Analysis of a novel low-cost solar concentrator using lunar flux mapping techniques and ray-tracing models

by

Casey Roosendaal

Submitted in partial fulfilment of the requirements for the degree:
Master of Engineering (Mechanical Engineering)

in the

Department of Mechanical and Aeronautical Engineering
Faculty of Engineering, Built Environment and Information Technology

UNIVERSITY OF PRETORIA

SOUTH AFRICA

2020

Executive summary

Title:	Analysis of a novel low-cost solar concentrator using lunar flux mapping techniques and ray-tracing models
Supervisor:	Dr WG le Roux
Co-supervisor:	Prof JP Meyer
Department:	Mechanical and Aeronautical Engineering
University:	University of Pretoria
Degree:	MEng (Mechanical Engineering)

Concentrated solar power is a growing but expensive alternative energy resource. One of the most common issues faced when it comes to solar dish design is the complex trade-off between cost and optical quality. A novel solar dish reflector setup that makes use of low-cost, commercial television satellite dishes to support aluminised plastic membranes in a multifaceted vacuum-membrane concentrator was investigated in this work. The design aims to reduce costs while maintaining high optical accuracy with the added benefit of optical adjustability. The flux distribution of the novel solar dish reflector setup had to be determined to make recommendations on the feasibility of the design. This research presents a method to determine the expected solar flux distribution from lunar tests using a Canon EOS 700D camera. Experimental tests and different pollution treatment methods were conducted using lunar flux mapping techniques. A numerical model of the experimental setup, based on photogrammetry results of the membrane surface, was also developed in SolTrace to ascertain the sources of error and allow for further design improvements. Preliminary testing proved that JPEG image formats yielded insufficient accuracy in capturing the incident flux when compared to RAW images. Based on the flux ratio maps, the intercept factor for a large multifaceted dish setup was calculated as 88.6% for an aperture size of 0.25 m × 0.25 m, with a maximum solar flux of 1 395 kW/m^2 for a 1 000 W/m^2 test case.

The numerical model showed that the experimental setup had a total optical error of 17.5 mrad with a comparable intercept factor of 88.8%, which was mainly due to facet misalignment and not reflector surface inaccuracies. The results suggest that large performance improvements can be gained through a more accurate aiming strategy. It is recommended that more durable membrane material can be used, along with an automated vacuum control system that can account for membrane leaks and temperature swings during operation. Correlations between the optical behaviour and geometrical features of elliptically supported facets can be further investigated to develop a design tool to aid in the design and development of high-performance systems. Overall, the design proved to be a viable design alternative for point focus solar concentrators to reduce costs and maintain optical accuracy. The lunar flux mapping techniques proved effective and safe by using the incident light from the moon and standard camera equipment.

Acknowledgements

I would like to thank the following people who assisted me in my work throughout my postgraduate studies:

- Dr Willem le Roux for being a phenomenal supervisor and friend during my studies. Your guidance has been invaluable and deeply appreciated. I will look back fondly on the time spent working with you for many years to come.
- Mr Jonathan Swanepoel for being the pleasant, hardworking individual he is, as well as for his extensive contributions in the collaborative research that was performed.
- Mr Tshepo Phakisi and Mr Jehiel Jacob for assisting with the design work.
- Mr Vincent Good for his photography services during the moonlight testing.
- Dr Radhakrishnan for kindly assisting with the UV/VIS testing.
- Mr Chris Govinder and Donald Keetse for their assistance in the construction phase and for providing space in the Wind Tunnel Labs as the main facility for most of the construction.
- Mr Marcel Slootweg for assisting with getting the numerical model up and running.

Thank you to the vacation work students who assisted with the manufacture, assembly and testing of the final system. It was a pleasure to work with you all as this would not have been possible without you.

The financial assistance of the National Research Foundation (NRF) towards this research is hereby acknowledged. Opinions expressed and conclusions arrived at are those of the author and are not necessarily to be attributed to the NRF. The work presented is based on the research supported by the financial contributions of the Technology Innovation Agency (TIA), the University of Pretoria's Research and Development Plan (RDP) and the NRF (Grant Number 109311).

Finally, I would like to thank my friends and family for their support and guidance throughout my studies. Your motivation has driven me to try and excel academically and better myself as an academic and human being. Without your support and time, I would not be the person I am today and for that I am grateful. I will also be forever grateful for the assistance of my dear friend, Marcel Killian, during moonlight testing – I am sorry that he is no longer with us. You will be dearly missed.

Research outputs

The following research outputs were produced from this work:

1. **Journal article**: Roosendaal, C., Swanepoel, J. K. and Le Roux, W. G., 2020. Performance analysis of a novel solar concentrator using lunar flux mapping techniques. Solar Energy, Volume 206, pp. 200–215.

2. **Conference paper:** Swanepoel, J. K., Roosendaal, C. and Le Roux, W. G., 2020. Photogrammetry analysis of a vacuum-membrane solar dish using elliptical television antennas. Presented at the 26th Annual SolarPACES Conference (SolarPACES2020).

Table of contents

List of figures

List of tables

List of symbols

Nomenclature

A	Area, m^2
$\bar{A}$	Facet length, m
$\bar{A}*$	Projected facet radial length, m
$\bar{B}$	Facet width, m
$\bar{B}*$	Projected facet width, m
CR	Concentration ratio
D	Diameter, m
d	Depth, mm
E	Pixel value, V/m^2
Et	Effective mechanical stiffness, N/m
F	Scaling factor
f	Focal length, m
f_0	Ideal focal length, m
f-stop	Focal STOP, focal length to diameter of lens iris ratio
I	Irradiance, W/m^2
l	Length, m
Mil	Thousandth of an inch, $inch^{-3}$
N	Total number of pixels in target surface image
n	Total number of pixels in aperture zone area
px	Pixel

T_0	Geometric induced stiffness due to initial tension, N/m
W_0	Parabolic depth, m
x	Spatial x-coordinate, m
y	Spatial y-coordinate, m

Greek characters

γ	Intercept factor
ε	Strain
θ	Facet tilt angle, degrees
ρ	Reflectivity
ϕ	f/D ratio
ψ_{rim}	Rim angle, degrees

Subscripts

ap	Pertains to the aperture zone
dish	Pertains to solar dish
facet	Pertains to facet
G	Global
g	Geometric
i	Pixel number index
L	Local
major	Major axis (largest)
max	Maximum
minor	Minor axis (smallest)

peak	Peak
pix	Scaled per pixel
r	Solar radiation flux
refl	Reflective
tot	Total target board surface
virt	Virtual

Abbreviations and acronyms

APS	Active pixel sensor
BOPET	Biaxially oriented polyethylene terephthalate
CAD	Computer-aided design
CCD	Charge-coupled device
CFA	Colour filter array
CMOS	Complementary metal-oxide semiconductor
COBYLA	Constrained optimisation by linear approximations
CSP	Concentrated solar power
CSV	Comma separated value (Excel file format)
DCT	Discrete cosine transform
DHI	Diffuse horizontal irradiance, W/m^2
DNG	Delaware National Guard
DNI	Direct normal irradiance, W/m^2
DoE	Department of Energy
DSLR	Digital single-lens reflex

EFS	Electro-focus, small image circle
ETFE	Ethylene tetrafluoroethylene
GHI	Global horizontal irradiance, W/m^2
HTF	Heat transfer fluid
IR	Infrared
IS STM	Image stabilisation stepper motor
ISO	International Organization for Standardisation – regarding sensor sensitivity
JPEG	Joint Photographic Experts Group – image format
LEC	LaJet Energy Company
MD	Machine direction
MDF	Medium density fibre
NIR	Near-infrared
NREL	National Renewable Energy Laboratory
NRF	National Research Foundation
PHLUX	Photographic flux
PVD	Physical vapour deposition
RAW	Raw camera sensor data – image format
RDP	Research and Development Plan
RGB	Red, Green, Blue
RMSE	Root mean square error
SAIC	Science Applications International Corporation
SBP	Schlaich, Bergermann and Partner
SKI	Solar Kinetics, Inc.

TD	Transverse direction
TIA	Technology Innovation Agency
UV	Ultraviolet
VIS	Visible

1. Introduction

1.1 Background

The sun is an abundant resource of energy that is available around the world in varying quantities. Just outside the atmosphere, the sun provides a constant 1.367 kW/m^2, known as the solar constant (Stine & Geyer, 2001). This value is affected by the atmosphere and local meteorological factors, depending on location, as well as the spectral distribution of the radiation. According to Le Roux (2016), measured solar radiation can be classified as global horizontal irradiance (GHI), direct normal irradiance (DNI) and diffuse horizontal irradiance (DHI). Point focus solar concentrators only focus DNI from the sun as the geometrical nature of their design can only effectively concentrate parallel or collimated rays.

According to South Africa's Department of Energy (DoE) (2020), South Africa has one of the best solar resources in the world, with average solar radiation levels of 4.5–6.5 kWh/m^2 per day. The site of this study is the University of Pretoria in South Africa. According to SolarGIS (2019), data averaged from 1994 to 2015 shows that ±2 000 kWh/m^2 per year can be expected for the chosen project site (Figure 1-1). The DNI present at a particular site varies during the year due to the seasonal changes that occur, which are unique to each geographic location.

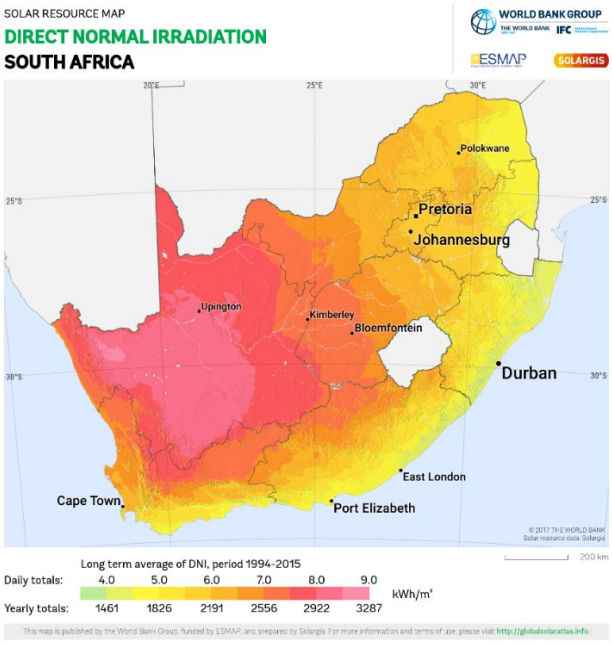

Figure 1-1: Annual sum of DNI irradiation (SolarGIS, 2019)

Concentrated solar power is a growing but expensive alternative energy resource technology. Its high cost is mainly due to the high-precision solar concentrators that are required to obtain acceptable operating thermal efficiencies. Opting for a low-cost solution for the solar dish often leads to poor accuracy with little to no ability to adjust the optical image once constructed. Coventry and Andraka (2017) elaborate on the interconnectivity between high optical performance and the increasing costs due to materials, surface inaccuracies and construction. One of the older proposed solutions is the stretched membrane concentrator. Starodubtsev et al. (1965) first described a vacuum-focused solar concentrator using a polymer mirror, according to Alpert et al. (1991). More recently, Schmitz et al. (2017) demonstrated an elliptical vacuum-membrane multifaceted reflector, as was proposed by Zanganeh et al. (2012), using silvered aluminium sheeting.

In the current study, a new design aims to reduce costs, while maintaining high optical accuracy with the added benefit of optical adjustability. This was accomplished by manufacturing individual facets out of commercially available television satellite dishes with aluminised plastic film to form a multifaceted vacuum-membrane concentrator. The lightweight facets were affixed to a modular support structure in a hexagonal honeycomb arrangement and in the profile of a paraboloid, where each facet could be adjusted individually.

1.2 Problem statement

One of the most common issues faced when it comes to solar dish design is the complex trade-off between cost and optical quality. In 2019, a novel solar dish reflector setup that makes use of low-cost, commercial television satellite dishes as a support for aluminised plastic membranes in a multifaceted vacuum-membrane concentrator was constructed at the University of Pretoria. Methods to determine the optical accuracy of the setup by aiming it at the sun can be expensive and destructive. Cost-effective and non-destructive methods had to be developed to determine the flux distribution of the novel solar dish reflector setup so as to determine its optical accuracy.

1.3 Reason for research

As energy needs continue to impact on the environment, more effort has been invested in developing sustainable, renewable energy in the hope of fighting global warming. Solar energy is a large contributor to alternative energy as it is an abundant resource worldwide. However, current methods of solar energy capture often involve low energy conversion efficiencies such as

photovoltaic systems or enormous start-up capital like that of central tower receiver and linear parabolic trough solar power plants.

The air-standard Brayton cycle is the ideal cycle for a simple gas turbine using a single-phase, gaseous working fluid (Borgnakke & Sonntag, 2012). The solar-dish Brayton cycle follows the same system principles with the addition of a recuperator (Dellar et al., 2020) and solar collector (Craig et al., 2020) for heat input to form an open and direct solar thermal Brayton cycle, shown in Figure 1-2 (Le Roux & Meyer, 2016). The system is being developed on the roof of the Engineering 2 Building at the University of Pretoria. The system has the potential for low cost (Mills, 2004), high reliability (Pietsch & Brandes, 1989) and cogeneration and hybridisation (Le Roux, 2018).

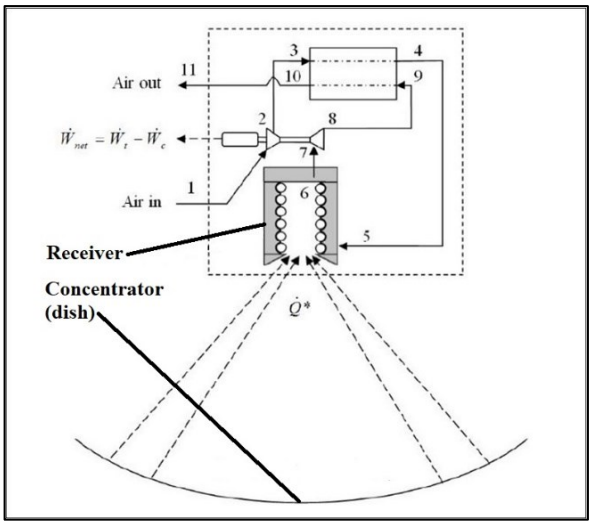

Figure 1-2: Open and direct solar thermal Brayton cycle (Le Roux & Meyer, 2016)

The optical performance of any solar dish is of importance as it directly affects the net power output of a concentrated solar energy system. The efficiency of the parabolic dish and receiver system is determined by the intercept factor (γ). The intercept factor is defined as the fraction of the rays reflected from the mirror that reaches the receiver (Goswami, 2014). According to Stynes and Ihas (2012), the intercept factor is a combination of several sources of error, some of which are dynamic and difficult to measure. However, the main contributors can be quantified. These are concentrator surface slope error (concentrator shape), concentrator specularity error, concentrator alignment error, system tracking error and receiver alignment error. The optical properties of the parabolic dish related to the intercept factor can be improved to increase system efficiency.

1.4 Objective

The objective of this research was to test and investigate a large, low-cost, multifaceted stretched membrane solar dish made from off-the-shelf television satellite dishes and a single layer of Mylar film to act as a membrane and as the reflective surface. In order to make recommendations on the feasibility of the design, the optical performance of the system had to be measured using lunar flux mapping techniques with investigations into image file formats and light pollution treatments. A numerical model also had to be developed by characterising an experimentally measured membrane surface shape (using photogrammetry) with known mathematically expressed surfaces. Using the numerical model, the sources of optical error had to be identified and measured using a discretised optical surface representative of the multifaceted dish array in ray-tracing software. Initial investigations into the optical behaviour of the facets, based on their geometric properties, had to be conducted to establish correlations that could be used to aid future designs in achieving high optical efficiencies with greater ease. The results produced from this research could be used to design and implement stretched membrane dish technology in various concentrated solar power (CSP) applications.

1.5 Overview

A literature review that details the work done by previous researchers was conducted and is reported in Chapter 2 to understand the current advantages and disadvantages of stretched membrane dish technology, as well as the methods developed to measure the performance of solar concentrators. The lessons learnt from previous research were used as a foundation. In Chapter 3, the setup of a large multifaceted dish, comprising 33 facets using low-cost, off-the-shelf satellite dishes that each supports an aluminised plastic membrane, is discussed. The experimental methods used to measure optical performance are also explained with various light pollution treatment strategies. Furthermore, the development of a numerical ray-tracing model to ascertain the sources of optical error in the lunar test results is presented. In Chapter 4, the results of the experimental and numerical tests and their significance are discussed, along with suggestions for improvements to yield higher performance using the same low-cost facet design approach. Future work regarding the development of a design aid for small-scale multifaceted systems using the numerical model is proposed. A summary with conclusions and recommendations is presented in Chapter 5.

2. Literature study

2.1 Introduction

A review of the current literature pertaining to concentrated solar energy optics, used in a variety of applications, is presented below. It focuses on the fundamental principles of stretched membrane concentrators and discusses the characteristics of existing stretched membrane systems. The technology and methods used to measure the performance of solar dish systems are also reviewed.

When considering any form of high concentration solar energy system, the optical performance of the solar dish is of importance as it directly affects the net power output of the solar energy system. The most common issue faced when it comes to a solar dish design is the complex trade-off between cost and optical quality. Early developments of "low-cost" dishes by JPL, conducted with General Electric and Ford, had three design objectives (Coventry & Andraka, 2017):

- Develop a dish optimised for solar energy applications and do not modify existing telecommunication dishes by adding a reflective surface directly to the antenna surface profile
- Maximise the performance-to-cost ratio
- Base the design on commercially available manufacturing techniques

These trade-offs influence optical qualities such as slope error, reflectivity and aiming errors (Truscello, 1979), which encompass all the factors that affect the size and location of the focused image. Truscello (1979) goes on to mention that, to achieve high power conversion efficiencies, higher temperatures are required and therefore better-quality optics.

A further discussion of solar energy, previous research and the mechanisms that drive the optical performance of stretched-membrane concentrators is presented below.

2.2 The sun as a power source

The spectral distribution of solar radiation is important when considering the material used to effectively reflect solar radiation. According to Majka and Majka (2012), the sun's rays are seen from earth with a spectral distribution described by Figure 2-1 (Goswami, 2014). The majority of the solar intensity lies in the visible spectrum (390–700 nm). A graph of the spectral reflectivity versus wavelength for various metals at normal incidence is given in Figure 2-2 (McNulty, 2016).

Figure 2-2 shows that aluminised Mylar film (red) is a good reflector material choice as it is more reflective across a broader spectrum compared to some commercial reflective materials.

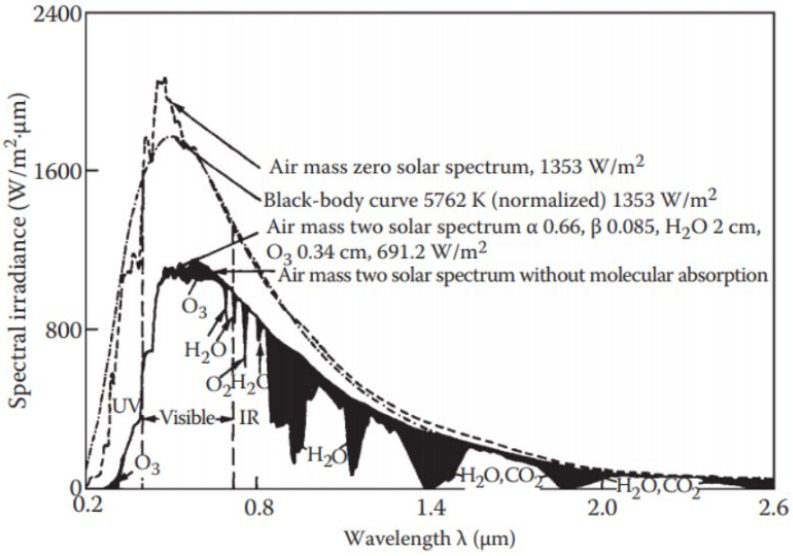

Figure 2-1: Extra-terrestrial solar radiation spectral distribution. Also shown are equivalent black-body and atmosphere-attenuated spectra (Goswami, 2014).

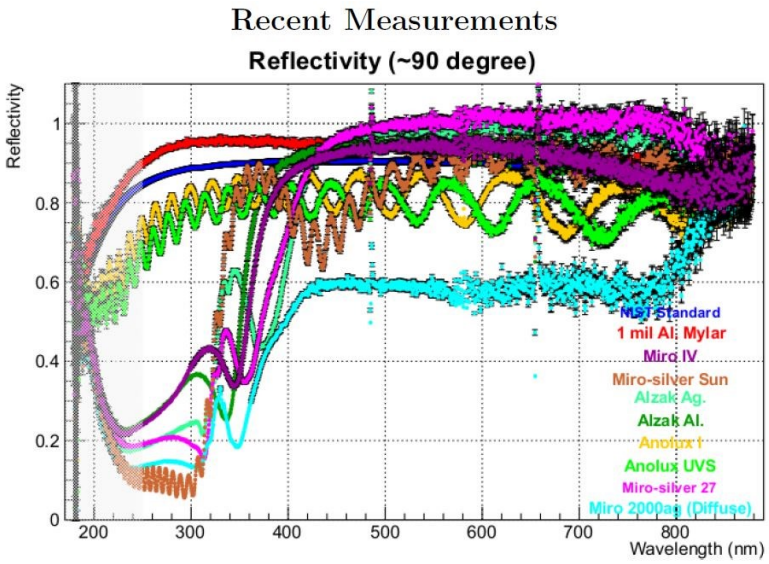

Figure 2-2: Reflectivity of some common metals versus wavelength at normal incidence (McNulty, 2016)

For most practical purposes, the sun's rays are assumed to be parallel. However, this is not the case with solar concentrators. The sun is approximately 1 390 473 km in diameter and its distance from

the earth is 150 000 000 km (NASA, 2017). This results in an angular diameter of 0.53˚ (Goswami, 2014). The sun's energy resource throughout the day is also not constant. Using data from a radiometric monitoring station located on the roof of the Engineering 1 Building at the University of Pretoria, a plot of the DNI, GHI and DHI of a typical sunny day in South Africa from 06:00 to 18:00 (13 September 2017, Spring) was created, shown in Figure 2-3 (SAURAN, 2018; Brooks et al., 2015).

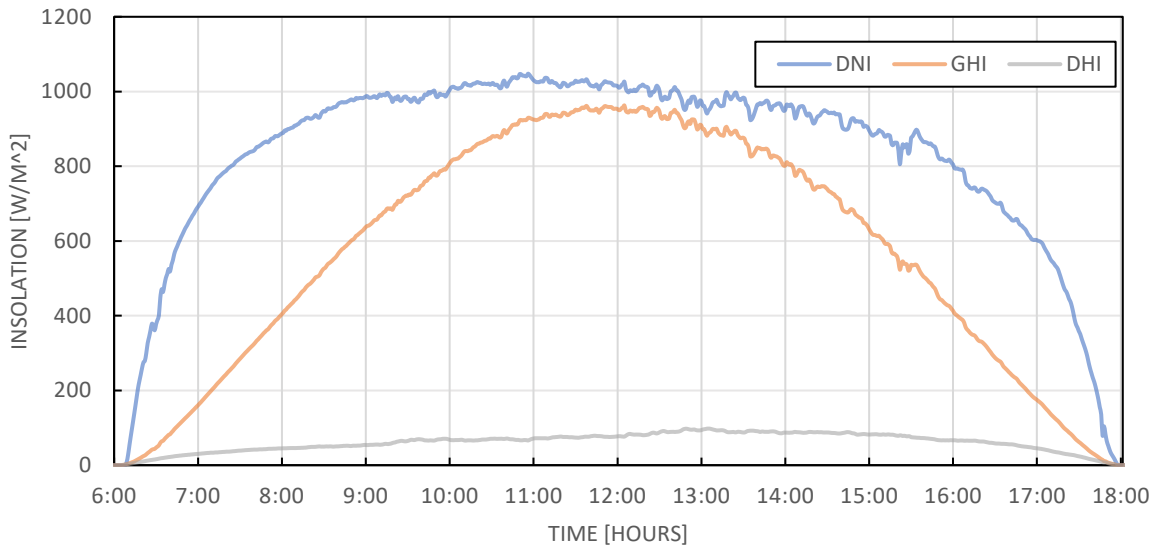

Figure 2-3: Insolation plot of DNI, GHI and DHI in Pretoria (13 September 2017) (SAURAN, 2018; Brooks et al., 2015).

With DNI being of specific interest to this research, a gradual increase and decrease at the start and end of the day are noted in Figure 2-3. This is due to the distance a ray needs to travel through the earth's atmosphere, which is greatest at sunrise and sunset. The DNI peaks above 1 000 W/m^2 at around 10:00 and tapers off again after 12:30. The significance of this with regard to concentrated solar energy is that, in order to produce any amount of usable thermal energy, optical performance needs to be high to capitalise on the small window of available high-intensity DNI. Low-level DNI can often decrease system efficiency and result in a net loss of thermal energy as the input capacity is not large enough to sustain any heat losses in the heat transfer fluid (HTF) transport system, while still maintaining sufficient heat for the systems to benefit from the solar energy input. Systems that implement thermal storage, however, can make use of the low-level

DNI to charge up to operating temperature in the early hours of the day and then slow down the discharge in the late hours, effectively increasing their operation duration.

A concentrated solar system design needs to account for the fluctuating availability of solar DNI. It must also account for changes in the sun's path throughout the year. The sun's path across the sky is dependent on the season, and the strategic placement of a solar system is required for optimal performance. Figure 2-4 illustrates the trajectories that the sun follows during the winter and summer solstices.

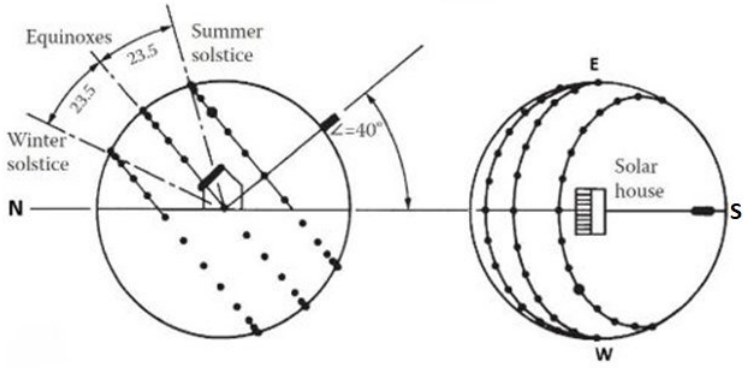

Figure 2-4: Sun paths for the summer solstice (21 June), the equinoxes (21 March and 21 September) and the winter solstice (21 December), adjusted for the southern hemisphere (Goswami, 2014)

2.3 History of stretched membrane dish technology

Vacuum membrane dish technology has been subject to extensive research over the years. According to Coventry and Andraka (2017), Bomin Solar pioneered the concept of using large foil membranes in the early 1970s, achieving high concentration ratios of over 1 000. Many variations were built, such as the DISTAL I dish series by the German company SBP since the early 1980s and a 7-m diameter stretched membrane dish by Solar Kinetics Inc (SKI) installed at Sandia, Albuquerque, in 1991. The DISTAL I dish implemented vacuum dish technology by slightly deforming a stainless steel membrane beyond its elastic limit using water to pre-curve the membrane. This allowed the required vacuum needed to reach the correct shape to be lowered during operation. The reflective surface was fabricated using 0.7 mm glass mirror sections adhered to the membrane surface (Coventry & Andraka, 2017). The 7-m SKI system had a similar approach to the DISTAL I system by deforming a 304 stainless steel membrane plastically to the desired shape. However, a secondary

polymer-based film was sucked onto the surface of the preformed stainless steel membrane and allowed for fast membrane replacement in the field (Coventry & Andraka, 2017). In 1988, a Sandia-contracted project saw the development of vacuum membrane-based heliostats that had a 0.076 mm-thick stainless steel membrane with 3M silvered-acrylic film adhered to the surface by the Science Applications International Corporation (SAIC) (Figure 2-5a) and a 0.25 mm aluminium version by SKI (Figure 2-5b). The SAIC version made use of a linear actuator on a rear membrane to control the reflective membrane shape, while SKI made use of a central fan on the front of the heliostat to generate the required negative pressure for membrane deformation (Alpert et al., 1991).

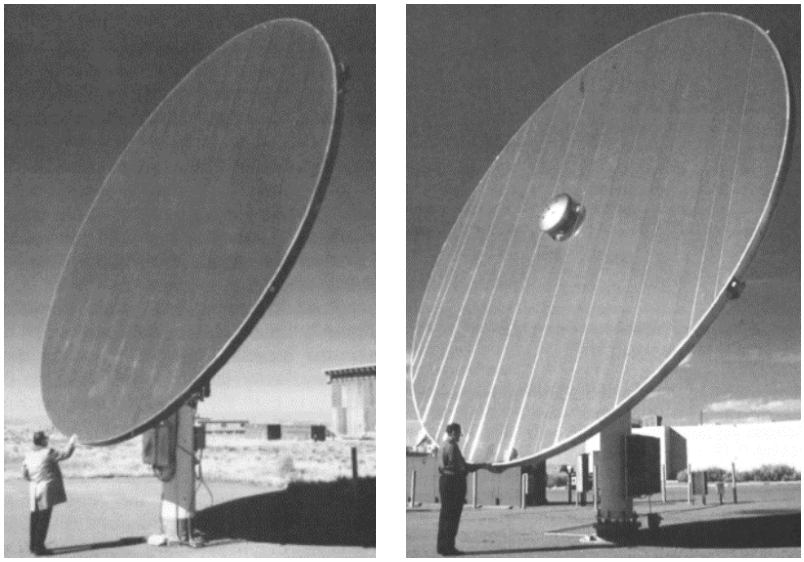

(a) (b)

Figure 2-5: Early stretched membrane modules: (a) SAIC; and (b) SKI (Alpert et al., 1991)

Furthermore, numerous other multifaceted stretched membrane reflectors have been developed, such as the LEC-460 Mylar stretched membrane dish by LaJet Energy Company (LEC) in 1984, and SAIC's stainless steel stretched membrane dishes since 1995 (Mancini et al., 2003; Coventry & Andraka, 2017). More recently, Schmitz et al. (2017) demonstrated an elliptical vacuum-membrane multifaceted reflector, as was proposed by Zanganeh et al. (2012), using a silvered aluminium sheet (Figure 2-6). Schmitz et al. (2017) tested two membrane thicknesses at 0.3 mm and 0.2 mm, which achieved average concentrations of 7 620 W/m^2 (68.2% intercept factor) and 8 970 W/m^2 (78.3% intercept factor), respectively. The thinner aluminium membrane demonstrated improvements in concentration and intercept factor. The increase in performance can be attributed to the difference in

thickness, changing the elastoplastic deformation behaviour based on findings from Dähler et al. (2016), according to Schmitz et al. (2017).

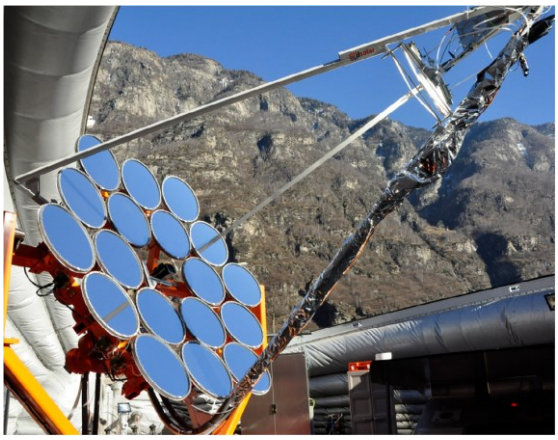

Figure 2-6: Vacuum facet prototype installed in Biasca (Switzerland) during testing (Schmitz et al., 2017)

The following section discusses the driving principles behind stretched membrane concentrators used to develop the various systems that were discussed and will aid in the optimal design of a new concentrator.

2.4 Principles of stretched membrane collectors

Stretched membrane collectors consist of a thin membrane supported by a rigid structural rim with an airtight seal. The membrane can be constructed from various flexible substrates, ranging from metals to polymers with a highly reflective surface on the side that faces outwards. The substrate used must allow a flat membrane surface to be deformed into a curved concentrating surface through elastic or plastic deformation. This is achieved by creating a vacuum within the plenum formed between the membrane and the support structure. The vacuum allows the atmosphere to apply a uniformly distributed pressure load on the unsupported membrane region, forming a continuous surface. This then allows rays of sunlight that approach the surface of the collector to be redirected to a focal point in a way that is comparable to a parabolic concentrator.

The ideal surface shape for concentrating solar energy is the paraboloid. Stretched membrane collectors approximate a parabolic surface under uniform pressure loading. According to Murphy and Tuan (1987), a homogenous and axisymmetric membrane will, in general, assume a limiting shape that is spherical. Flugge (1966) and Frei (1982) have shown that, for a uniformly pressure loaded

membrane with constant thickness and uniform tension (both spatially and in direction), supported by a circular frame, the resulting surface will be spherical, based on equilibrium conditions alone.

The material response and properties of the membrane are critical in achieving the desired surface. Murphy (1987) found that, for membranes that exhibit elastic material responses, uniform tension states are only achieved if either the ratio of the nominal focal length to dish diameter, f/D, is large, or if the dimensionless quantity, Et/T_0, is sufficiently small. Et represents the effective mechanical stiffness of the membrane, while T_0 is a measure of the geometrically induced stiffness due to the initial tension of the membrane in the flat state. This highlights the properties of interest for suitable membrane substrate materials. Murphy and Tuan (1987) further discuss that, with Et being small, small increases or variations in the stress field are seen when the membrane assumes the required surface. Similarly, if T_0 is quite large, the small deformation required to assume the required surface will be small compared to the average stress state when the membrane is flat, provided that the deformation due to the vacuum does not cross the yield point (Murphy & Tuan, 1987). These parameters emphasise how critical a uniformly distributed stress state is in order to approach a spherical surface. If the manufacturing process involves plastically deforming the membrane through large finite deformations to yield a permanent surface, a material with a very low plastic modulus is suggested by Gehlisch and Klaus (1982a, 1982b) and Khoshalm (1983). This allows for uniform stress distributions in the yielded areas of the membrane, which will again approach a more accurate parabolic contoured surface.

When considering the optical behaviour of a parabolic surface, any light that approaches the reflective surface parallel to the axis of the collector will be redirected to a focal point defined by the collector surface profile (Murphy & Tuan, 1987). This point can be mathematically calculated using Equation (2.1) where D is the collector aperture diameter, f is the focal length and Ψ_{rim} is the rim angle. According to Stine and Geyer (2001), the rim angle is defined as the angle between the normal position through the focal point to the centre of the collector and the line intersecting the edge of the collector and the focal point (see Figure 2-7a). Similarly, Murphy and Tuan (1987) describe the focal point using Equation (2.2) based on Figure 2-7a, where w_0 is the parabolic depth and r is the aperture radius. This results in a singular focal point, shown in Figure 2-7b.

$$f = \frac{D}{4\tan(0.5\Psi_{rim})} \tag{2.1}$$

$$w_0 = \frac{a^2}{4f} = \frac{r}{8\left(f/D\right)} \tag{2.2}$$

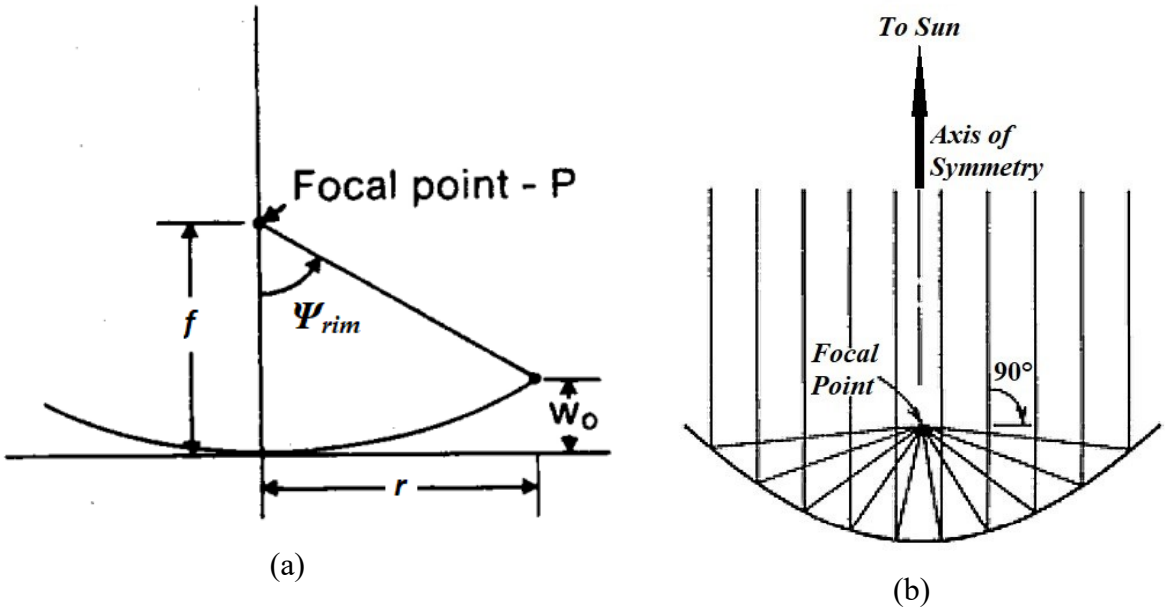

(a) (b)

Figure 2-7: (a) Parabolic collector geometry (Murphy & Tuan, 1987); and (b) ray diagram (Stine & Geyer, 2001)

The focal point of a spherical concentrator is more difficult to define based on the fact that it is not a single point, but a line along which reflected rays of light converge with a non-uniform distribution. Murphy and Tuan (1987) have mathematically described the optical geometry of spherical concentrators for membranes supported by a circular rim, based on Figure 2-8a, with equations (2.3) and (2.4). Two focal points are represented, where f_0 is based on the sphere centre and f_e is based on the concentrator edge. The two focal points represent the start and end of the focal line for a spherical concentrator. The smaller the difference between f_0 and f_e, the more accurate the parabolic approximation.

$$w_0 = 2f_0\left[1 - \sqrt{1 - \left(\frac{D}{4f_0}\right)^2}\right] \tag{2.3}$$

$$f_{e(a)} = 2f_0\left[1 - \frac{1}{2\sqrt{1 - \left(\frac{D}{4f_0}\right)^2}}\right] \tag{2.4}$$

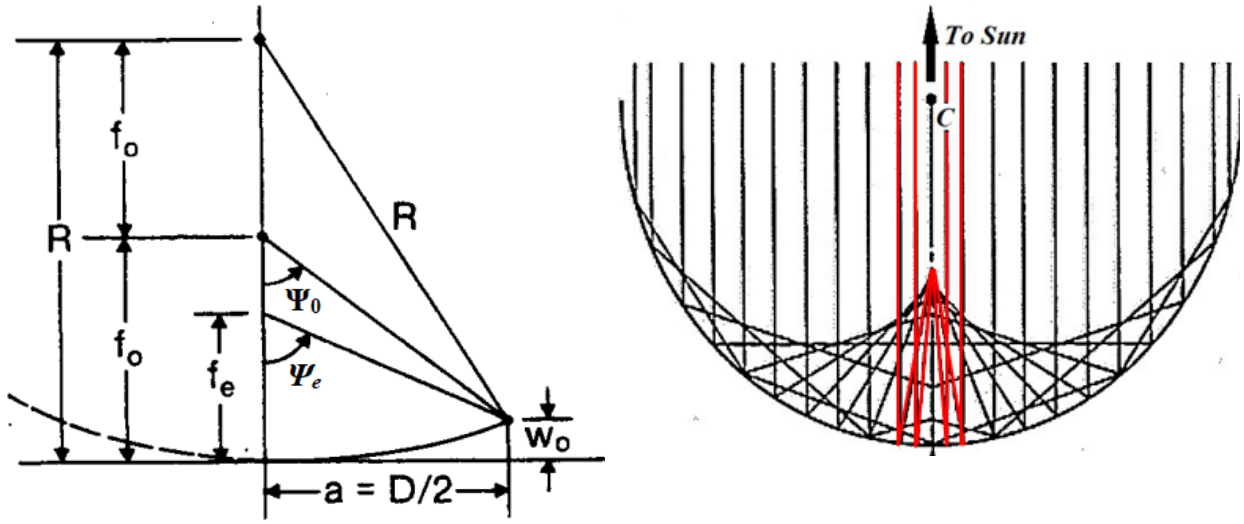

(a) (b)

Figure 2-8: (a) Spherical collector geometry (Murphy & Tuan, 1987); and (b) ray diagram (Stine & Geyer, 2001)

Schmitz et al. (2017) state that a spherical concentrator's ability to approximate a parabolic shape is limited when large rim angles and a compact design are required. Murphy and Tuan (1987) go on to explain that this is due to the optical effect inherent in spherical concentrators known as the spherical aberration effect. The focal point of a spherical concentrator, therefore, falls along the rotational axis of the spherical surface (Stine & Geyer, 2001). The aberration effect is shown in Figure 2-8b.

The spherical aberration effect becomes more apparent with smaller *f/D* values. As shown in Figure 2-8, the actual focal point lies within the rim of the spherical surface. This is an example of a small *f/D* value that leads to prominent aberration effects. By limiting the surface to reflect

only the rays highlighted in red, while maintaining the profile radius and, in turn, the focal length, the aberration effect is reduced, and the *f*/*D* ratio is increased. This also results in a shortened focal line, which converges towards a point, producing a more concentrated image.

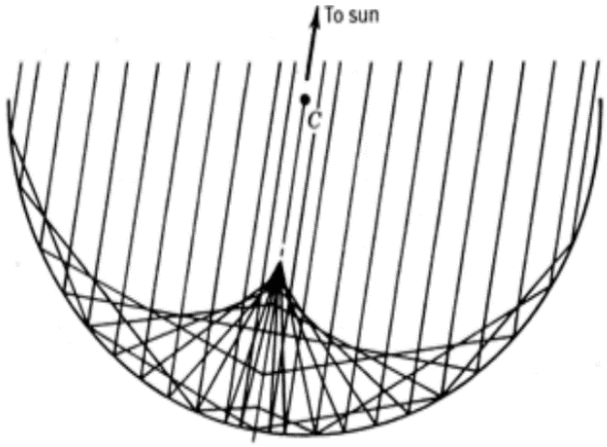

Figure 2-9: Misaligned spherical concentrator (Stine & Geyer, 2001)

Another key characteristic of spherical concentrator optics is that they are not as sensitive as parabolic concentrators to tracking misalignment with minimal image growth when large alignment errors are present. This is because the surface geometry is symmetrical about the surface centre. For this reason, faceted dish systems capitalise on the ability to focus light while being misaligned, according to Stine and Geyer (2001) (see Figure 2-9). This characteristic also allows a large optical surface to be approximated by an array of smaller facets at any scale. Not only does it provide more control of the location of the contributing facet images at the focal point, but it allows for smaller diameter facets to operate with large focal lengths. This increases the *f/D* value of the individual facets, while maintaining the global geometrical properties of the full array and, in turn, increases the optical precision. An additional knock-on effect is that, by implementing a faceted array, the production of the optical surfaces becomes less complicated. The tooling and manufacturing processes involved in producing a large membrane from industry-standard material sizes (usually supplied in sizes smaller than the final membrane unless specially ordered) are no longer necessary, reducing production costs.

Murphy and Tuan (1987) suggest that close parabolic approximation can be obtained for totally elastic membrane systems where *f/D* is greater than 2, as shown in Figure 2-10. Typical rim angles for a single stretched membrane are around 20° according to Schmitz et al. (2017), with Stine and

Geyer (2001) stating that, for practical applications, rim angles of spherical mirrors should range between 20° and 30°. However, single-facet solar dish designs typically operate with a dish focal length-to-diameter ratio of less than 1 ($\phi_G = f_{dish}\ /D_{dish} < 1$), which results in rim angles far higher than 20° (Zanganeh et al., 2012). By applying a faceted approach, one gets individual facets operating with a focal length-to-diameter ratio of around 6 ($\phi_L = f_{facet}\ /D_{facet} \cong 6$), keeping the facets closer to their optimal operating rim angles of around 20° (Zanganeh et al., 2012). This mitigates the material limitations and deviation from the parabolic approximation that occurs when larger rim angles are attempted (Schmitz et al., 2017).

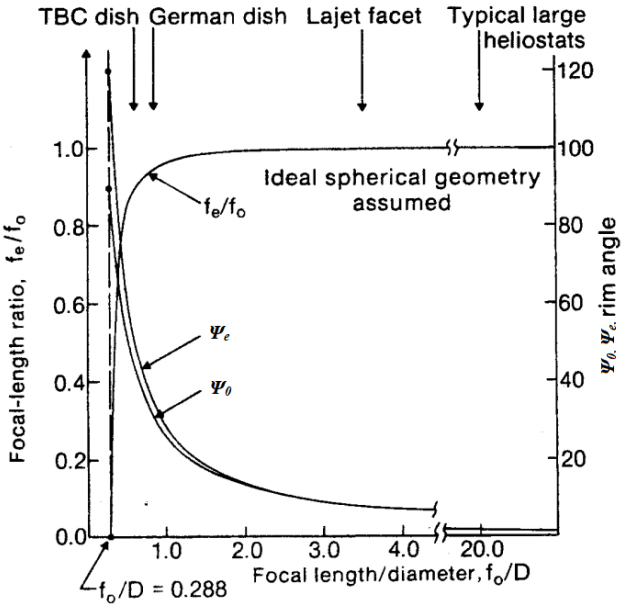

Figure 2-10: Ratio (f_e/f_0) of a spherical concentrator as a function of f_0/D and rim angles, Ψ_0 and Ψ_e, as a function of f_0/D (Murphy & Tuan, 1987)

2.5 Reflective membrane materials

Various reflective membrane products are available for use in vacuum-membrane technology. Most consist of a substrate material with a reflective coating adhered to the surface, commonly achieved with physical vapour deposition (PVD). This allows a thin uniform coating of either high-grade aluminium or silver to be deposited on the substrate surface. A few product examples are discussed below.

2.5.1 3M solar mirror film 1100

The 3M solar mirror film 1100 (3M Renewable Energy Division, 2012) is a silver metallised, weatherable film made from an acrylic substrate specifically designed for concentrated solar energy applications. It has a total hemispherical reflectance of 94% and an adhesive backing to allow for application to various smooth surfaces. This type of film is typically used on preformed concentrator surfaces. It has been applied to a stainless steel-based membrane system as shown in Figure 2-5a. The author found complications when initially trying to replicate the SAIC design in Figure 2-5a with strips of reflective material adhered to a membrane during a prototyping phase. As the membrane was extensively deformed, gaps between different sections of reflective film expanded, reducing the overall reflective area of the heliostat. Durability testing performed by Ho et al. (2011) concluded that the film's performance could be compared to that of traditional silvered glass mirrors. The results showed that the film only had slight decreases in specularity over long exposure times and with about 8 to 13% less total projected power when compared to an equivalent glass mirror.

2.5.2 ReflecTech Mirror Film

ReflecTech (DiGrazia & Jorgensen, 2010) is a polymer-based reflective film similar to 3M's solar mirror film 1100. It is a multi-layer construction with a silver reflective layer embedded under several layers of transparent polymer for protection. This helps to prevent oxidation and slows down ultraviolet (UV) degradation. It has a total specular reflectance of 94%. Performances in parabolic trough applications were reported with a solar-weighted hemispherical reflectance of 94% and a specular reflectance of 94% at a 25 mrad full acceptance angle at 660 nm (DiGrazia & Jorgensen, 2010). The product was able to sustain a high reflectivity during an accelerated seven-year test in desert conditions conducted by the National Renewable Energy Laboratory (NREL). Like 3M, it also has an adhesive back layer to adhere to various concentrator surfaces and therefore has similar applications and issues. However, both polymer-based films can still be used as the membrane and reflective material in small-scale applications where no joining is required to fabricate a single airtight membrane. When using the ReflecTech material as both the membrane and reflective surface, lower dish weights can be achieved as it contains less material compared to double-membrane systems that use a primary membrane with reflective material adhered to the surface.

2.5.3 MIRO-SUN

MIRO-SUN is a multilayer product designed specifically for outdoor use by Alanod Solar (2020). The sheet consists of a dual-sided anodised aluminium substrate with an air-to-air PVD coating of its trademarked MIRO^{TM} reflective coating. This coating is protected by nano-composite for weatherability and has an epoxy back layer. This product has a total solar reflectance of 90%. In the same manner as ReflecTech, MIRO-SUN can serve as both the membrane and the reflective surface.

2.5.4 Vega Energy

The Almeco Group (Almeca GmbH, 2015) produces a product similar to MIRO-SUN, using an aluminium substrate called Vega WR193. It has a 99.99% pure aluminium PVD coating with multiple optical index reflectance-enhancing layers, which are protected by a final weather-resistant coating referred to as a reflection stack. WR193 has a total solar reflectance of 89% with an 88.3% specularity. Almeco guarantees that the performance will remain within 3% of the original value over ten years.

2.5.5 Commercial Mylar

Mylar is a commercially available polymer typically used in food packaging. The addition of a PVD aluminium layer in a food-grade biaxially oriented polyethylene terephthalate (BOPET) reduces the permeability of the film to various gases (Mapes et al., 1993). Commercially available Mylar film was chosen due to its availability for this study to serve as a proof of concept. The 50 μm Mylar film sourced had no clear origin due to the multiple instances of rebranding through wholesalers and did not possess any form of UV protection or weather-resistant coating. Its reflectivity was measured using the ultraviolet visible (UV/VIS) spectroscopy in work done by Swanepoel (2019), yielding a 96.82% reflectivity for the visible spectrum. However, DuPont Teijin Films (2003), the company that holds the trademarked name Mylar^{TM}, states that its Mylar film has a machine direction (MD) modulus of 4.8 GPa and transverse direction (TD) modulus of 5 GPa with a 116% MD elongation and 91% TD elongation (DuPont Teijin Films, 2003). The material properties reported by DuPont Teijin Films (2003) shows that what is commercially known as Mylar is a highly elastic polymer that only yields at 0.196 GPa (MD) and 0.235 GPa (TD). It must be noted that, because of the different material properties (MD and TD), a non-uniform stress state will be present, albeit slight.

The various materials discussed are all good candidates for a small-scale multifaceted solar system. The nature of their design, being either polymer or metallic, will yield different results when considering the elastic behaviour and how well they can reach an ideal surface shape. Nonetheless, costing and durability need to be considered before further investigation.

2.6 Flux mapping techniques

To measure the incident flux produced by a solar concentrator and its performance when coupled with a receiver, an accurate means of measuring the flux intensity and its distribution is required. Numerous methods of measuring and evaluating the performance of a solar dish have been developed, along with dish technologies, the most common being systems based on energy balances using a calorimeter in conjunction with images recorded from a camera sensor. Schmitz et al. (2017) state that obtaining a relative scaled distribution is straightforward. However, the issue lies in obtaining the scaling factor (F) between the pixel intensity $E_{pix}(x, y)$ and the irradiance on the target surface $I(x, y)$ such that the relationship in Equation (2.5) is achieved.

$$I(x, y) = F \times E_{pix}(x, y) \qquad (2.5)$$

Many early methods have been investigated to determine the solar flux distribution on a target surface positioned at the focal point of a CSP plant, such as those presented by Blackmon (1985), Mavis (1988), Strachan and Houser (1993) and Ulmer et al. (2002). Most of these methods involve the direct measurement of the concentrated solar thermal radiation, which requires expensive and complex equipment to withstand the high-intensity radiation heat transfer. Another method mentioned is the Gardon gauge with small active regions placed inside a Lambertian target surface. Schmitz et al. (2017) presented their method of combining the Lambertian target surface with a calorimeter to create a flat plate calorimeter. This allows for the simultaneous measurement of the distribution and incident flux. Ho and Khalsa (2012) detail a more indirect approach, the Photographic Flux ("PHLUX") method, where images are taken of the sun, the incident flux on a Lambertian target surface, as well as the ambient pollution when the incident flux is not present. This method required various neutral density filters to prevent pixel saturation. However, Ho and Khalsa (2012) were able to calculate the flux incident on a Lambertian surface with a relative error of 2%. The methods outlined by Ho and Khalsa (2012) and Burgess et al. (2012) were later also modified for lunar testing by Siangsukone et al. (2004), Pye et al. (2017) and Wolff et al. (2018) for

solar dishes with non-faceted parabolic concentrator designs. Cioca and Wang (2013) show how closely the lunar spectrum matches that of the standard solar spectrum and why it is a suitable substitute for the sun (see Figure 2-11).

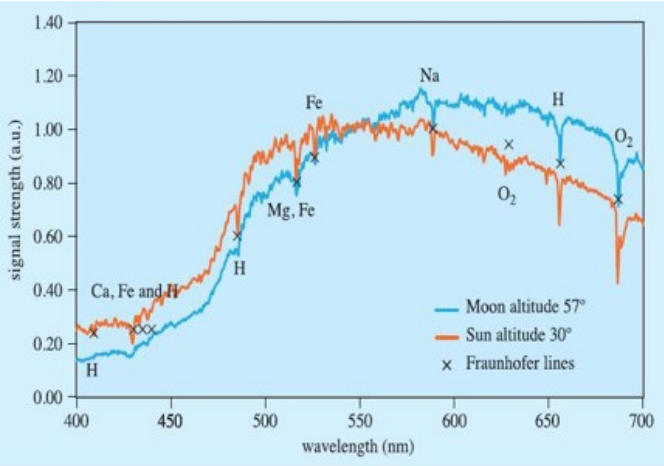

Figure 2-11: Sunlight and moonlight spectra normalised at 550 nm (Cioca & Wang, 2013)

Focusing on the photographic approaches of Ho and Khalsa (2012) and Wolff et al. (2018), it is worth understanding the camera technology used for the analysis. The dominant digital camera sensors that exist in the market today are the charge-coupled device (CCD) and complementary metal-oxide semiconductor (CMOS) sensors, which are linear photoconductive devices, with the major differences being the photon to charge readout methods (Lebourgeois et al., 2008). CMOS sensor advances have made them superior to CCD sensors by using the same pinned photodiode image sensor used in CCD sensors, along with local charge amplification integrated into the sensor, as well as the addition of an active pixel sensor (APS) (Gouveia & Choubey, 2016). This has greatly reduced the readout noise used in what is known as digital single-lens reflex (DSLR) cameras (Van Bakel, 2018).

Most of the cameras that use CMOS sensors make use of a colour filter array (CFA). This restricts certain pixels to only measure red, green or blue (RGB) light, also known as a Bayer array. To get the RGB values for each pixel, demosaicing or CFA interpolation is performed. Due to this filter, the CMOS sensor is only able to pick up certain wavelengths of light. Lebourgeois et al. (2008) provided a spectral analysis of the CMOS sensor in a Canon EOS 400D for the standard case with the near-infrared (NIR) filter and without the NIR filter for the red, green and blue channels in the sensor.

The CMOS sensor can capture light with wavelengths ranging from roughly 375 nm to just above 950 nm without an NIR filter, which encompasses the boundaries of the visible spectrum. This accounts for roughly 69% of the solar spectrum as is evident in Figure 2-12, where the red, green and blue plots represent the red, green and blue colour channels. With the filter, the range is limited to 375 nm to 750 nm and therefore accounts for 50% of the solar spectrum. However, most of the solar intensity falls within the visible spectrum and can therefore be captured by the camera sensor. The same applies to the lunar flux as the lunar spectrum closely resembles the solar spectrum with regard to intensity as shown in Figure 2-11. Therefore, professional digital cameras with a CMOS sensor are suitable enough for flux capturing without incurring the high cost of specialised camera equipment. This is since the most intense radiation – solar and lunar – falls within the visible spectrum (Lebourgeois et al., 2008).

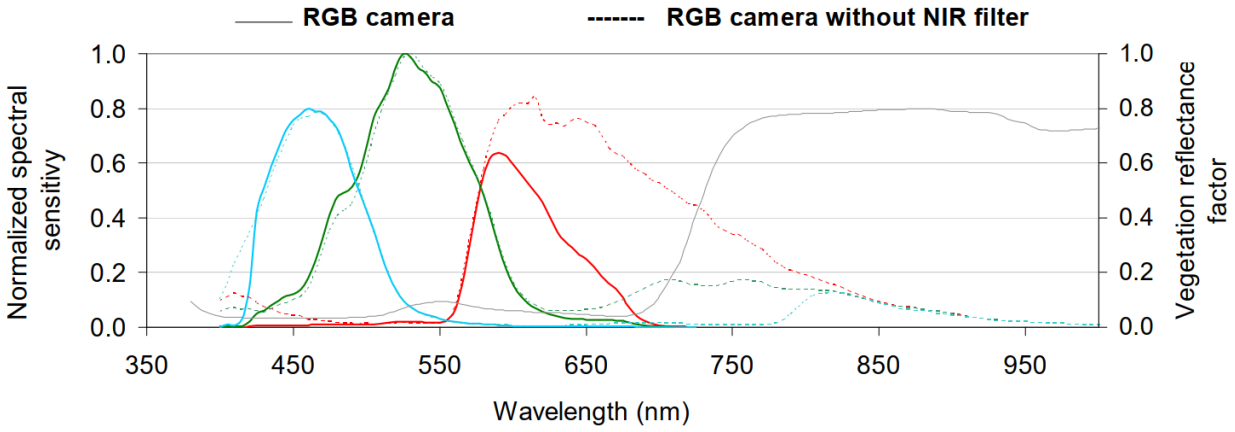

Figure 2-12: Normalised spectral sensitivity of Canon EOS 400D for the three colour channels (red, green and blue) with NIR filter (solid lines) and without NIR filter (dashed lines) (Lebourgeois et al., 2008)

An advantage of lunar flux mapping is that the analysis may be performed during full moon at night instead of in the midday sun since the moon is considered to produce a flux distribution that is comparable to that of the sun due to their similar angular diameters (Siangsukone et al., 2004). Goswami (2014) reported the sun's average angular diameter as 0.53˚, while Faulkner (1998) reported the moon's average angular diameter as 0.518˚. This allows the optical behaviour during lunar tests to closely resemble tests performed with the sun. With these low-intensity light conditions, no additional camera attenuation filters are required, and a less complex material can

be considered for the target surface. Simple camera settings such as ISO, f-stop and shutter speed are used to keep images from saturating. The absence of high-intensity flux makes calibration safer, as adjustments can take place during operation without the risk of injury to personnel and damages to other system components not designed for high-intensity flux.

2.7 Conclusion

The research presented in this chapter highlighted the benefits of stretched membrane dishes with regard to the reduction of construction costs, while preserving optical performance, as well as providing a means of measuring high-intensity flux indirectly. Flugge (1966) and Frei (1982) state that a stretched membrane dish assumes a surface that is spherical on equilibrium considerations alone, with optimal parabolic approximations occurring after *f/D* ratios of 2 according to Murphy and Tuan (1987). By selecting a polymer-based membrane, such as Mylar film by DuPont Teijin Films (2003), desirable results can be achieved due to its small modulus and high elasticity, based on work done by Murphy and Tuan (1987). To achieve the large *f/D* ratios required for optimal performance as stated by Zanganeh et al. (2012), a multifaceted approach is adopted for the design of the dish array. This approach is different to previous designs where a metal membrane was used with reflective films or glass mirrors adhered to the membrane surface, as described by Coventry and Andraka (2017).

To experimentally determine the optical performance of the multifaceted array and to measure the flux, one can substitute the sun with lunar irradiance during a full moon. Wolff et al. (2018) and Siangsukone et al. (2004) outlined the benefits of using a full moon to measure high flux intensity concentrators using an indirect photographic approach detailed by Ho and Khalsa (2012) called the PHLUX method. The process of determining the flux distribution takes advantage of the low-intensity light of a full moon, resulting in a low-risk testing procedure. The applications are mainly aimed at point focus dish systems that are able to photograph the incident flux with the camera sensor in a normal position in relation to the target surface.

The appeal of a multifaceted stretched membrane collector is that the design yields a lightweight, low-cost alternative with optical performance that can be compared to conventional rigid glass, metal or composite collectors. These qualities provide a possible solution to the prominent issue where high optical accuracy in rigid glass-styled collectors resulted in high production costs.

The next chapter applies the fundamental work that was reviewed in Chapter 2. It describes the experimental and analytical methodologies that were followed to obtain the results presented in this work. The experimental method details the setup of the multifaceted dish system, along with preliminary pollution treatment investigations that were applied in the lunar flux mapping techniques that were used. The fundamentals of the code used to process the results are also discussed. Furthermore, the analytical model that was developed is discussed and serves to investigate the unique surface shape and ascertain what errors contributed to the performance results that were found.

3. Methodology

3.1 Introduction

This chapter details the numerical and experimental procedures used to investigate and further develop a low-cost solar concentrating solution for use on an open-air solar Brayton cycle setup being developed on the roof of the Engineering 2 Building at the University of Pretoria. A numerical model to determine the sources of optical error for further improvements is also presented.

An experimental setup was tested using lunar flux mapping techniques during a full moon. Lunar flux mapping techniques were accessible using professional camera equipment and post-processing scripts written in Python and MATLAB. The lunar flux mapping method produced flux ratio maps and intercept factor plots to evaluate the optical performance and allows for comparison with other experimental setups. Methods for treating light pollution are also discussed.

A numerical model, based on the experimental setup, was developed that discretises the optical surface of the facet surface. Various Python scripts are used to set up the model along with SolidWorks for the computer-aided design (CAD) and SolTrace as the ray-tracing platform. Optical behaviour concerning the facet geometrical properties was investigated parametrically before setting up the final model, which was parameterised concerning optical error to determine the source of the errors present in the experimental results by comparing flux maps and intercept factor plots.

3.2 Experimental setup

A large multifaceted solar dish was constructed at the University of Pretoria using the lightweight faceted vacuum-membrane approach. The dish array comprised 33 elliptical facets fitted to commercially available Ellies satellite dishes (see Appendix A). The goal was to achieve a solar dish with good optical performance, but to include a large degree of optical adjustability at a lower cost. The incident flux could be adjusted in size and intensity by adjusting individual facets' aim or adjusting the membrane shape itself. This section details the design of the elliptical facets, as well as the support structure. It also discusses the experimental methods and testing procedures that were followed.

3.2.1 Facets

Satellite television dishes are generally considered to be low-cost items because of mass manufacturing. As shown in figures 3-1 and 3-2, the individual facets were constructed from

820 mm × 757.5 mm (measured outer dimensions of 860 mm × 790 mm) elliptical television satellite dishes with low-cost 50 µm aluminised BOPET membranes, also known as Mylar membranes, adhered to the leading edge of the satellite dish with an adhesive sealant (SikaTack). According to Good et al. (2016), aluminised BOPET is a highly specular material. The angular scattering of aluminised BOPET is accurately described by a single Gaussian distribution according to Good et al. (2016) with standard deviations of less than 0.05 mrad at all measured wavelengths and incidence angles. The angular scattering can therefore be assumed to be negligible for the reflective membrane.

Electric, normally closed, solenoid valves were installed on the back of the facet alongside the two-axis adjustable bracket used for mounting the dish to a round steel supporting arm in a honeycomb arrangement. By basing the facet construction on off-the-shelf television satellite dishes, manufacturing costs and weight are reduced extensively. The satellite dishes used can be classified as thin sheet-metal profiles with enough concavity to support a membrane under vacuum and a uniform smooth edge for airtight membrane attachment. Mapes et al. (1993) showed that, for a 90 kPa pressure difference and a temperature of 22 °C, 50 µm aluminised BOPET film has a weighted average permeation of 4.3 ml/m^2 per minute. For the exceedingly small pressure differences expected on the vacuum membrane facet, the permeation rate would be almost negligible and the BOPET film would provide a sufficient air seal.

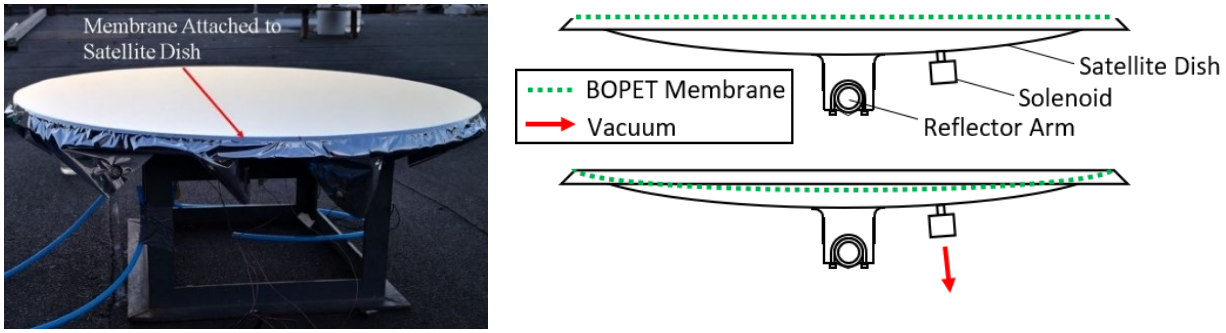

(a) (b)

Figure 3-1: (a) Completed facet being tested for leaks; (b) Illustration of a single-dish facet in a non-vacuum state (top) and a vacuum state (bottom) (Swanepoel, 2019)

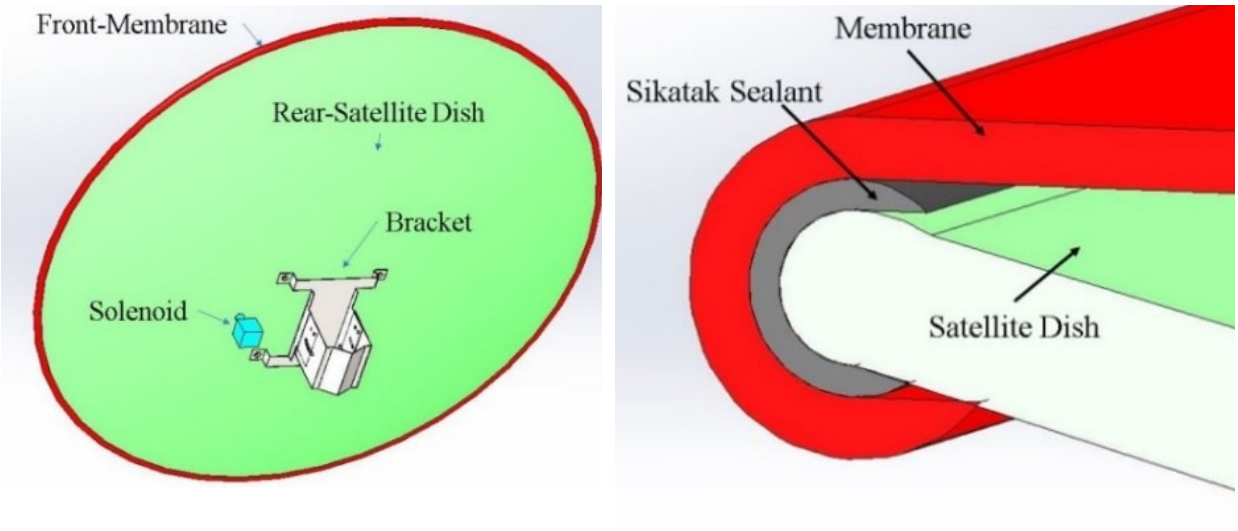

(a) (b)

Figure 3-2: (a) Rear-view of facet construction; (b) Membrane attachment method

3.2.2 Dish structure design

The design focused on optical accuracy and ease of operation to allow one-man operation when on-sun tests were performed. It integrated with a tracking system in a modular fashion to allow for the disassembly and storage of individual arms, with the facets attached, when not in use. The arms were attached to a central hub mounted on the tracking system using a tube-in-tube socket system. The individual dish arm tubes were notched to ensure correct alignment in the hub and were then clamped down using industrial stage-light clamps with a load capacity of 500 kg fitted to a rectangular aluminium support frame. This secured the arms in place and ensured that they were installed in the same location and orientation every time so as not to nullify the calibration that had to be done on the facets. The array consisted of three different dish arms: a straight arm, a T-arm and a special T-arm. See Appendix B for additional illustrations of the experimental setup and arrangement of the different arm types in the array.

A simple analogue control system was implemented to adjust the membrane shape. A control box with illuminating switches in the layout of the array was used to open any specific solenoid valve (6 W) attached to the back of a given facet by delivering 12 V provided by a QJE PS3020 lab power supply. Each dish arm had a polyurethane pneumatic line connecting the individual solenoids to a single line, which was then attached to a ring circuit at the base of the dish, as well as to the wiring that powered the solenoids. All pneumatic lines were connected using push-in

fittings while the wiring was fitted with an XT60 connector to allow for the quick disconnection of all the dish arms' pneumatic and electrical lines from the ring circuits.

To control the membrane shape, one had to control the pressure in the plenum of the facet. This was achieved using a 230 V, 186 W, 66 l/min single-stage vacuum pump and a 12 V, 168 W, 30 l/min automotive compressor connected to the pneumatic ring circuit. The pumps were controlled by two normally open push buttons with a spring return to allow for small adjustments of the plenum pressure. See Appendix B for images of the control system.

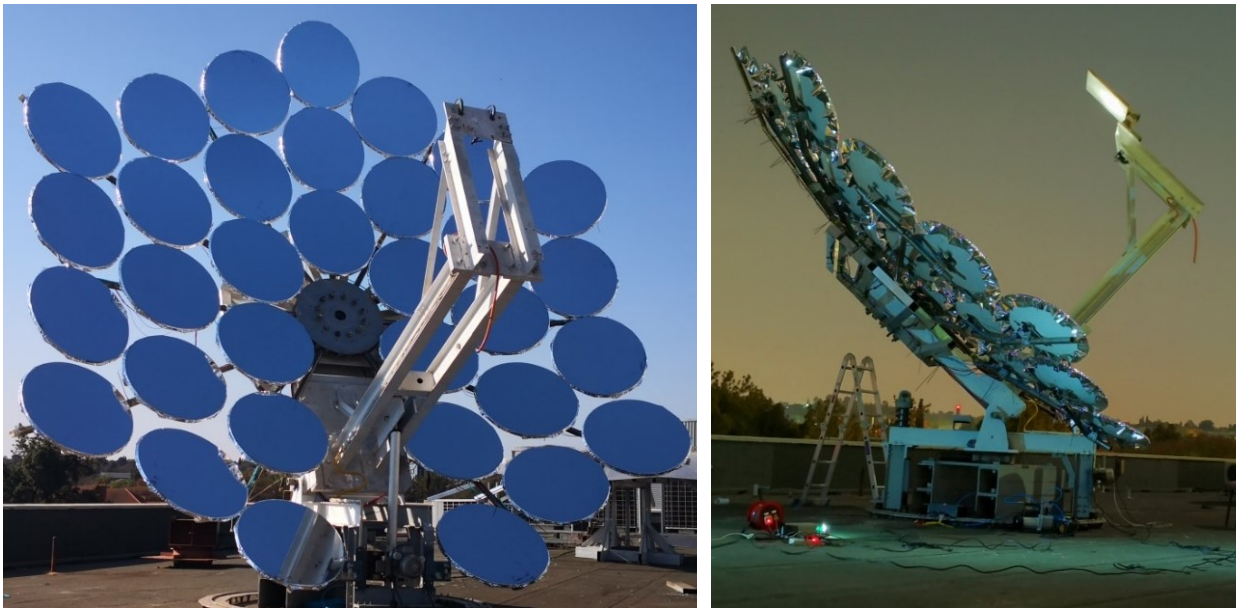

(a) (b)

Figure 3-3: (a) Completed large solar dish setup before aiming and lunar calibration; and (b) during lunar calibration

The multifaceted dish (see Figure 3-3) was mounted on a two-axis solar tracking system with azimuth and elevation control utilising an electric slew drive and actuator, which were not connected to an automated tracking control system, and was therefore separately and manually operated. The solar receiver could be mounted on a central arm that was fixed relative to the array and moved together, while the entire setup tracked the sun. For lunar testing, a target surface was manufactured to cast the same size shadow on the central hub when placed in the same plane and focal length as the focal point of a solar receiver. The target surface was made from medium density fibre (MDF) board (0.54 m × 0.54 m), sanded down to a smooth surface and painted with

a high matt white paint to serve as an approximate Lambertian surface. This ensured that any light hitting the surface did not appear brighter than it was due to unwanted specularity, which could skew results. The Lambertian target surface experienced no damage during testing due to low-intensity moonlight, and as a result, remained consistent.

3.2.3 Dimensioning

Table 3-1 shows the dimensions of the setup according to the layout shown in Figure 3-4. Note that two of the facets on the fourth ring (denoted as 4b in Table 3-1 and shown as purple in Figure 3-4) could not be mounted like the other facets (denoted as 4a in Table 3-1 and shown as pairs of dark green facets in Figure 3-4) in the ring due to tracking interferences with the tracking frame.

Table 3-1: Detailed geometric characteristics of the dish setup

Ring no	Radius from centre of the array (m)	Local focal length, f_L (m)	Projected local facet dimensions		Projected facet aspect ratio ($\bar{A}^*/\bar{B}^*$)	Projected facet area, A_L (m^2)	Local facet ratio (f_L/D_L)
			$\bar{A}^*$ (m)	$\bar{B}^*$ (m)			
1	0.82	2.72	0.82	0.76	1.08	0.49	3.45
2	1.46	2.90	0.80	0.76	1.06	0.48	3.72
3	1.69	3.02	0.81	0.76	1.06	0.48	3.85
4a	2.17	3.23	0.71	0.82	0.86	0.46	4.23
4b	2.27	3.25	0.81	0.76	1.07	0.48	4.15
5	2.56	3.41	0.76	0.76	1.00	0.45	4.50

The local facet focal length (f_L) was defined as the distance between the facet centroid and the focal point as illustrated in Figure 3-5a. By considering the incident area of each reflector facet, the associated local diameter (D_L) could be determined according to Equation (3.3), where $\bar{A}$ = 820 mm and $\bar{B}$ = 757.5 mm. It is important to note that the incident area (A_L) is calculated using the area of an ellipse. Note that the projected facet length in the radial direction is $\bar{A}^* = \bar{A}\cos\theta$ and therefore the incident area changes with the tilt angle (θ) of the associated facet, as illustrated in Figure 3-6. In the case of the T-arm facets, the projected facet length becomes $\bar{B}^* = \bar{B}\cos\theta$. Using the incident areas for the reflector facets, the total reflective area of the elliptical facets (A_{refl}) was then determined. The work of Zanganeh et al. (2012) suggested that an elliptical facet is beneficial since the tilting of the reflector facet to face the receiver aperture results

in a near-circular image projected onto the receiver aperture plane because of the angle between the incident solar rays and the tilted reflector facet. According to Zanganeh et al. (2012), elliptical facets can increase the intercept factor by 6.6% and the concentration ratio by 12%.

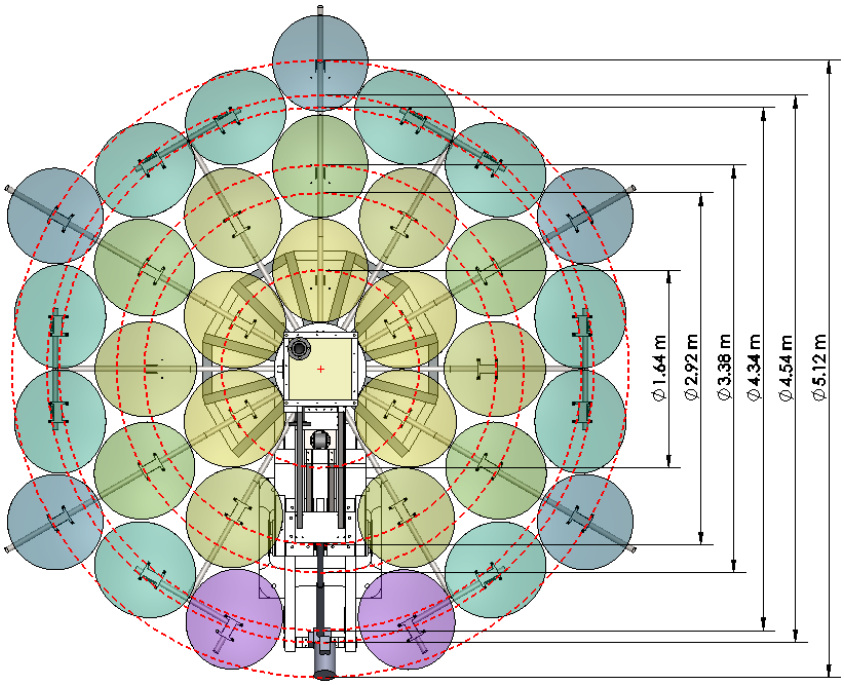

Figure 3-4: Layout of the dish setup using off-the-shelf satellite television antennas as facets

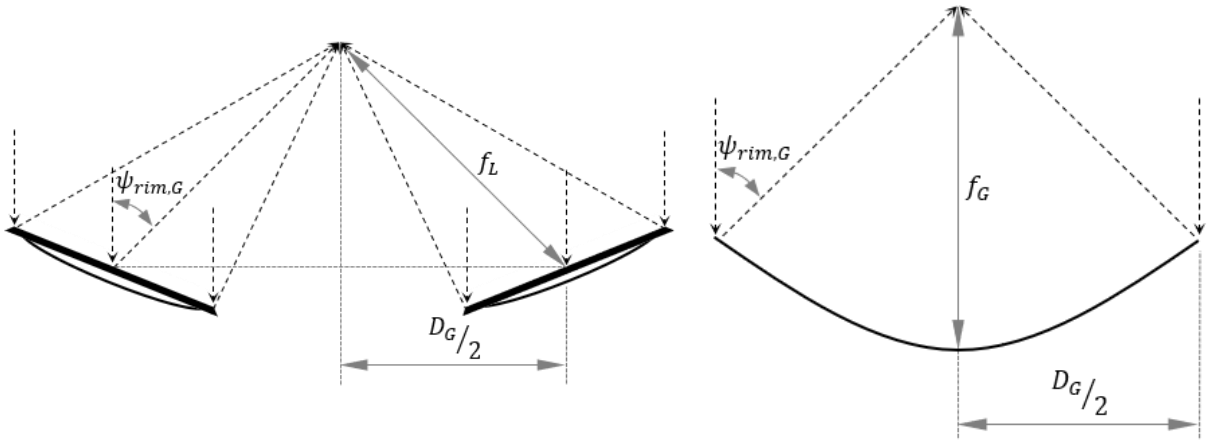

(a) (b)

Figure 3-5: (a) Dimensions of the faceted dish with two of the outermost, opposing facets represented (Swanepoel, 2019); and (b) dimensions of an equivalent parabolic dish reflector

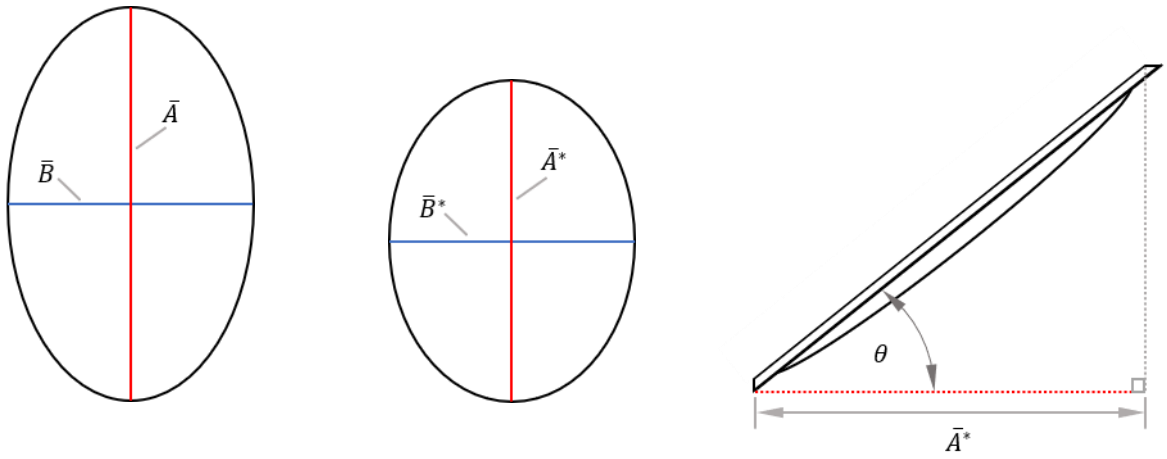

(a) (b) (c)

Figure 3-6: (a) The incident area of the elliptical facet oriented at a normal position to the point of reference (Swanepoel, 2019); (b) the incident area of the tilted elliptical facet (Swanepoel, 2019); and (c) a side view of the tilted facet (Swanepoel, 2019)

The global dimensions of the full array were defined according to an equivalent solid parabolic dish reflector that the faceted reflectors were approximating. As shown in Figure 3-5a, the global diameter (D_G) was defined as the diameter from the centroids of the outermost facets of the associated dish reflector. The outermost centroids were located at a diameter of 4.98 m around the central axis of the reflector. The global focal length (f_G) was calculated using Equation (3.1) (Stine & Geyer, 2001), where the area of the dish was taken as the virtual incident area (A_{virt}) based on the global diameter (see Equation (3.2)), as shown in Figure 3-5b.

$$A_{virt} = 4\pi f_G^2 \frac{sin^2\,\psi_{rim,G}}{\left(1 + cos\,\psi_{rim,G}\right)^2} \tag{3.1}$$

$$A_{virt} = \frac{\pi D_G^2}{4} \tag{3.2}$$

$$A_L = \frac{\pi(\bar{A}^*)(\bar{B}^*)}{4} = \frac{\pi D_L^2}{4} \tag{3.3}$$

The dimensions of the setup are presented in Table 3-2. Because the array had six facet location diameters (see Figure 3-4) and therefore six different focal lengths, the local focal lengths and local diameters of all 33 facets were averaged when determining the average local facet ratio, ϕ_L.

Table 3-2: Geometric characteristics of the dish setup

	Symbol	Units	Value
Number of facets	-	-	33
Global diameter	D_G	m	4.98
Global rim angle	$\psi_{rim,G}$	degrees	46
Virtual area	A_{virt}	m^2	19.48
Global focal length	f_G	m	2.93
Global reflector ratio, f_G/D_G	ϕ_G	-	0.59
Total reflective area	A_{refl}	m^2	15.57
Average local facet ratio, f_L/D_L	ϕ_L	-	3.97

3.2.4 Testing procedure

The dish setup was tested during a full moon using a stock Canon EOS 700D camera with a CMOS sensor without any expensive attachments. Camera settings were adjusted using the built-in histogram to ensure that the image was just below saturation. The camera settings are listed in Table 3-3. The photographer (Mr Vincent Good) chose these settings to mitigate any light saturation that could be present on the image. The camera was mounted as shown in Figure 3-7a.

The camera's location needed to be fixed during testing to ensure that the same image frame was captured with each shot. A tripod was used to mount the camera and was secured to the central hub of the dish. This was essential as two images were required for the artificial light pollution treatment method discussed later. One image with the concentrated lunar flux at the target surface and another where the dish was intentionally misaligned with the moon to move the lunar flux away from the target surface were required to capture the pollution present on the target surface. This allowed the camera to capture a pollution image of the target surface, while a controlled level of artificial pollution was added from a point source. This was later used for image correction during post-processing as a large degree of dynamic ambient light pollution was present on the target surface due to city lights.

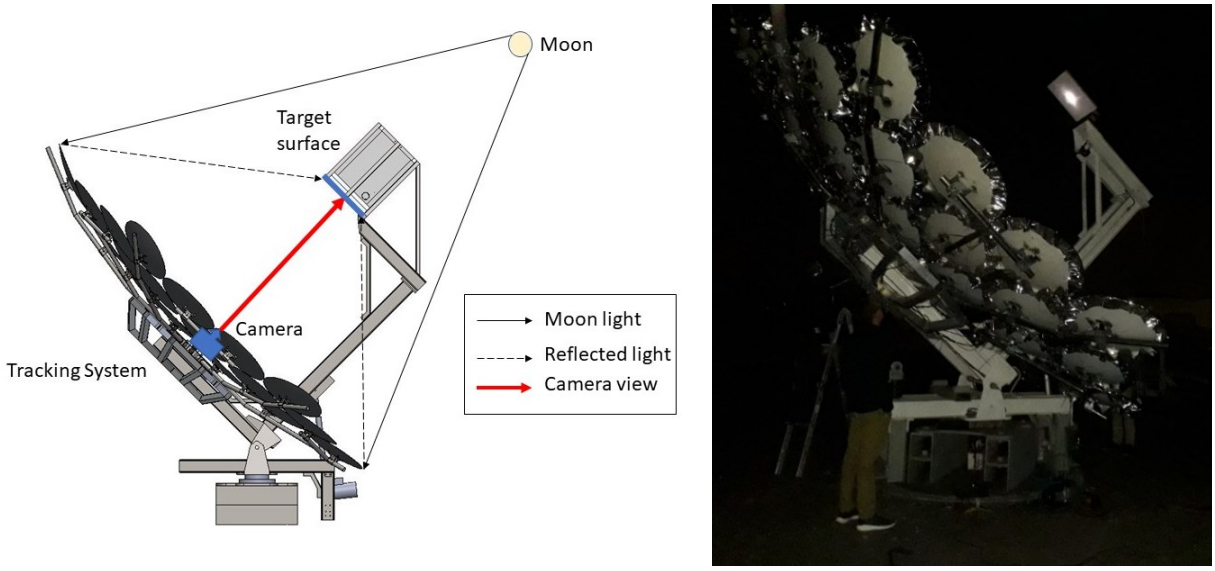

(a) (b)

Figure 3-7: (a) Experimental setup; and (b) experimental testing of the dish setup

Table 3-3: Camera properties during moonlight test

Property	**Value**
Aspect ratio	5 184 × 3 456
ISO speed	ISO-100
F-stop	f/4
Exposure time	0.4 second
Zoom lens	EFS 18–55 mm f/3.5–5.6 IS STM

Each facet had to be calibrated before the photographs were taken. The calibration consisted of manually assessing and adjusting the aim of the individual facets and then activating their respective solenoid valves using a control board. The vacuum pump and compressor were then used to achieve the smallest image possible, after which the solenoid was closed off to lock in the membrane shape. Different vacuum levels were achieved within each facet by opening the solenoid to the specific facet and closing all other solenoids. Adjustments to each membrane shape were made in about 20 seconds and most facets did not need to be readjusted again after an hour. Once the tightest concentrated flux was obtained (see Figure 3-7b) by manually calibrating each

facet's aim and membrane shape, RAW and JPEG images were taken of the flux distribution and the baseline artificial light pollution.

3.3 Data processing procedure

Based on the work of Ho and Khalsa (2012), an arbitrary voltage unit of V/px^2 was used to represent the camera sensor data of the image taken, where the voltage represents the average pixel value, and px^2 represents the respective area of the pixel. The aspect ratio of the image file, after cropping the image to the borders of the target surface, was then scaled to its respective dimensions by determining the associated area per pixel on the target surface, A_{pix}. This was done by dividing the total target surface area of 0.54 m × 0.54 m by the total number of pixels on the target surface. Based on the assumption that each pixel represents a square area on the target surface and that the area per pixel did not change, the side length of a square pixel was determined by calculating the square root of the pixel area. Results processing took place in MATLAB where both the JPEG and the raw Bayer data (RAW image) were accessed. The code used is explained in detail in Appendix C.1 and Appendix C.2. The raw Bayer data was processed to yield a 14-bit depth grayscale image of the flux distribution by averaging the RGB values for each pixel. Parts of the process used to achieve the demosaiced image before converting it to grayscale are detailed by Sumner (2014).

3.3.1 Light pollution

Two different methods for the treatment of city light pollution were investigated. The first method assumed that the dark edges of the photographed target surface represented the average baseline pixel value of the city's light pollution present. Therefore, calculating the average pixel value of the target board boundary yielded a value representing the baseline pollution pixel value. In the second method, artificial light pollution was imposed onto the target surface using a uniformly diffuse point source placed behind the facets and pointing directly towards the target surface, ensuring uniform illumination. The incident lunar flux was photographed with the city light pollution present, as well as the isolated imposed light pollution, which represents the baseline values. For both methods, the baseline values were subtracted from every pixel value of the lunar flux image, isolating the contributions from the dish facets that were present on the target surface.

3.3.2 Flux mapping

The pixel data of the treated image was first normalised based on the maximum pixel value in the image with the minimum pixel value expected to be found along the boundary of the target surface. The pixel values were thus normalised to produce a high-resolution flux ratio map with values scaled between 0 and 1, after which the flux map and intercept factor could be generated.

When considering the work of Ho and Khalsa (2012), the ratio between the intensity of pixel i with respect to the maximum pixel intensity is equivalent to the flux ratio as shown in Equation (3.4). Note that E_{max} refers to the maximum pixel intensity while I_{max} refers to the peak solar flux.

$$Flux\ Ratio_i = \frac{E_i}{E_{max}} = \frac{I_i}{I_{max}} \tag{3.4}$$

It is assumed that any solar flux distribution at the target surface normalised by its peak solar flux value would be equal to the normalised lunar flux distribution created from the digital image captured of the moonlight concentrated onto the target surface as shown in Equation (3.4). Furthermore, the total power incident on the target surface should equal the total power reflected by the dish reflector. Therefore, the summation of the discretised radiation pixel values relating to the irradiance from the sun can be expressed as shown in Equation (3.5), where A_{refl} is the incident area of the dish reflector and ρ_{dish} is the dish reflectivity. The solar flux distribution on the target surface (I_i) can be determined by multiplying the normalised flux distribution ($Flux\ Ratio_i$) by the peak solar flux (I_{max}), as shown in Equation (3.6).

$$\rho_{dish} A_{refl} DNI = \sum_{i}^{N} I_i\, A_{pix} \tag{3.5}$$

$$I_i = Flux\ Ratio_i \times\ I_{max} \tag{3.6}$$

$$\rho_{dish} A_{refl} DNI = \sum_{i}^{N} \{Flux\ Ratio_i \times I_{max} \times A_{pix}\} \tag{3.7}$$

Using Equation (3.7), a peak solar flux, I_{max}, can be determined, which would result in a solar flux distribution that would be equivalent to the solar power expected during the day, in such a way that the total incident power per pixel area would correlate to the given direct solar power.

The intercept factor (γ) defined by Equation (3.8) is calculated based on a square aperture zone, A_{ap}. Note that A_{tot} represents the total target board surface area (0.54 m × 0.54 m), while A_{ap} represents

the area of a virtual aperture zone on the target board (0.25 m × 0.25 m). The centroid of the aperture zone is defined at the weighted centroid of the lunar flux distribution.

$$\gamma = \frac{\sum_i^n E_i}{\sum_i^N E_i} = \frac{\int_0^{A_{ap}} E(x,y)dxdy}{\int_0^{A_{tot}} E(x,y)dxdy} \tag{3.8}$$

The intercept factor, as a function of the geometric concentration ratio, allows for comparison between different setups. The associated geometric concentration ratio, based on the total dish reflective area (A_{refl}), is defined by Equation (3.9). Note that A_{refl} is the sum of all the local facet areas (A_L) in Equation (3.3).

$$CR_g = \frac{A_{refl}}{A_{ap}} \tag{3.9}$$

3.4 Numerical model

The literature in section 2.4 outlined the behaviour of a stretched membrane when supported by a circular frame. Any deformation that occurs when a vacuum is drawn develops a uniform stress state in the membrane, provided that the initial tension and thickness is uniform, and the membrane is supported by a perfect circle. However, the implementation of elliptical satellite dishes will result in different behaviours. The elliptical support resulted in an unknown surface shape and therefore the optical relationships developed for spherical surfaces can no longer be applied. Therefore, the surface geometry of a membrane supported by an elliptical rim had to be investigated to identify the surface shape. Simulating the behaviour of the identified surface can then produce the results needed to develop new relationships.

The membrane surface was first experimentally determined using photogrammetry and then modelled in SolTrace to understand the optical behaviour and develop optical correlations to aid in modelling an array more accurately. The model would also allow sources of optical error to be identified. By modelling a perfect array, and later implementing optical errors using slope error and aiming error, the main source of error could be identified. This was achieved by adjusting the applied errors to match the flux map and intercept factor plots with those of a lunar test. With the results, targeted improvement of future designs or upgrades on the current system can be performed. The following sections detail the numerical modelling procedure that was followed in characterising the membrane surface and initial testing that led to its necessity.

3.4.1 Initial testing

Initial observations of a facet prototype provided some insight into understanding the behaviour of the membrane. Initial deductions concluded that a likely driving factor behind its divergence from a spherical surface is the difference in length between the major and minor axes that define the elliptical rim. This would result in unequal tension states. If the basic principles of material deformation are considered, the behaviour can be explained. If the membrane is to deform to a fixed depth, located at the centre of the ellipse, strain along the major axis of the membrane will be less than that of the minor axis. This is because the deformation required to reach the same depth occurs over a longer distance and the material experiences less elastic deformation and therefore less strain, according to Equation (3.10). The initial understanding was that the resulting surface could be described as a combination of the curvatures of two spherical surfaces with different surface radii and therefore different focal lengths, supported by two circular rings based on the major and minor diameters.

$$\left[\varepsilon_{minor} = \frac{\Delta l}{l_{minor}}\right] > \left[\frac{\Delta l}{l_{major}} = \varepsilon_{major}\right] \qquad (3.10)$$

Evidence of this surface description was present in the focal image of the elliptical facet when adjusting the focal length. The image was elliptical at its most concentrated size. Changing the focal length of the facet by changing the magnitude of the vacuum behind the membrane while the target and facet remained at fixed locations showed that the elliptical focal image went through an inversion at the focal point. Just before the focal point, one of the image axes would contract while the other would grow slightly. After passing the average focal point, the roles would reverse. Going further beyond or before the focal point, the focal image increased uniformly, but still maintained the inversion of the ellipse (see Figure D.7 in Appendix D). A preliminary explanation is that, as the membrane is drawn in, decreasing the focal length, the first focal point is reached.

Decreasing the focal length further deviates from the first focal point and approaches the second focal point. This increases the image axis attributed to the first focal point and decreases the axis attributed to the second focal point. This understanding formed the basis for the analysis approach discussed below.

3.4.2 Photogrammetry

After noticing the unique optical behaviour of the elliptical facet prototype, it was decided that the surface needed to be characterised. The membrane surface was captured by Swanepoel (2019), following the work of Dähler et al. (2016) using the GOM ARAMIS Adjustable 4M System. The facet was placed in a vertical orientation in front of the ARAMIS camera system. By placing high-contrast markers on the membrane surface, as well as a stationary reference point, membrane displacements under vacuum at the marker locations could be captured and calculated with reference to a control image taken with a flat membrane, as well as the stationary reference markers (Figure 3-8).

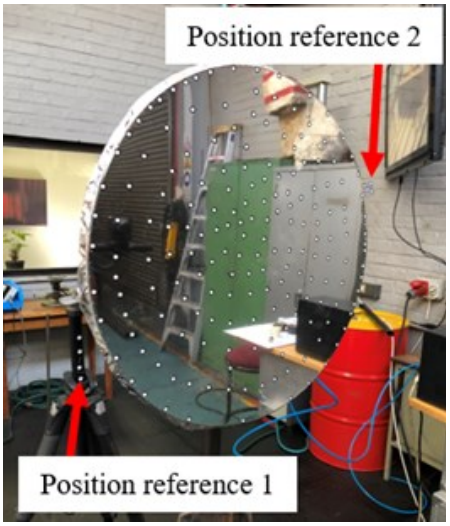

Figure 3-8: Photogrammetry test using the GOM ARAMIS 4M System (Swanepoel, 2019)

Using the results from the photogrammetry, Swanepoel (2019) fitted two mathematically defined 3D surfaces using the constrained optimisation by linear approximations (COBYLA) algorithm. These were an elliptic paraboloid, shown in Equation (3.11), and a hemi-ellipsoid, shown in Equation (3.12), where the *a*-coefficients define the shape of the surface and the *b*-coefficients define the location of the surface. Swanepoel (2019) found that the hemi-ellipsoid had the best fit with a minimised root mean square error (RMSE) of 24.07×10^{-2} mm for the given membrane depth used during testing. The RMSE was 27.34×10^{-2} mm for the elliptic paraboloid. Both surfaces proved to be good surface fits on the membrane shape that was created when a vacuum was drawn behind a thin Mylar membrane supported by an elliptical rim from a satellite dish. However, the elliptic paraboloid was chosen due to the ease with which it could be defined in a

SolidWorks model using the dimensions of the elliptical rim and membrane depth. The surface of the elliptical facet can therefore be represented using an elliptic paraboloid.

$$z(x,y) = \frac{(x+b_1)^2}{a_1^2} + \frac{(y+b_2)^2}{a_2^2} - b_3 \tag{3.11}$$

$$z(x,y) = a_3\sqrt{1 - \frac{(x+b_1)^2}{a_1^2} + \frac{(y+b_2)^2}{a_2^2}} - b_3 \tag{3.12}$$

3.4.3 Ray-tracing procedure

To create a geometric stage of triangular surface elements that represent an elliptic paraboloid, the following procedure was followed:

SolTrace (Wendelin et al., 2013) was used to simulate the behaviour of the elliptic paraboloid. However, SolTrace's native surface options could not capture an elliptic paraboloid. In addition to limited surface options, SolTrace did not have the functionality that allows imported custom geometries. Using the native irregular triangle aperture and flat surface options, the elliptic paraboloid could be discretised with triangular surfaces as a single geometric stage with the optical properties of aluminised Mylar applied to the surface elements.

By constraining the dimensions of the elliptical rim to those of the Ellies satellite dish (with measured inner dimensions of 757.5 mm × 820 mm) used in the photogrammetry and defining the membrane depth, a SolidWorks CAD model of the surface could be constructed based on the elliptic paraboloid (Figure 3-9a). The CAD model was then imported into ANSYS where the surface was meshed using triangles (Figure 3-9b). The mesh data was saved as a .msh file and served as the defining geometric source for the triangular surface elements. A Python script and .lk SolTrace script, developed by Craig et al. (2020), allowed for the custom meshed geometry to be imported into SolTrace and were implemented in the analysis process. The Python script converted the .msh file into a series of text files that contained the surface element location and orientation data, optical properties and simulation setup constraints. Using the .lk script, these files were then imported into a SolTrace project. To complete the setup process, virtual targets were placed at the estimated focal point to visualise the convergence of the reflected rays (Figure 3-9c). Two hundred parallel virtual stages were created using large circular flat surfaces and were spaced

1 mm apart to ensure that the focal point was captured with 1 mm accuracy. By looking at the virtual stages from the side, using SolTrace 2012.7.9, the location of the smallest image could be found. An example of the full simulation is shown in Figure 3-9d. Selecting the focal plane and displaying it as a flux map provided values for the centroid of the flux, which could be used to determine the translational distance and image size.

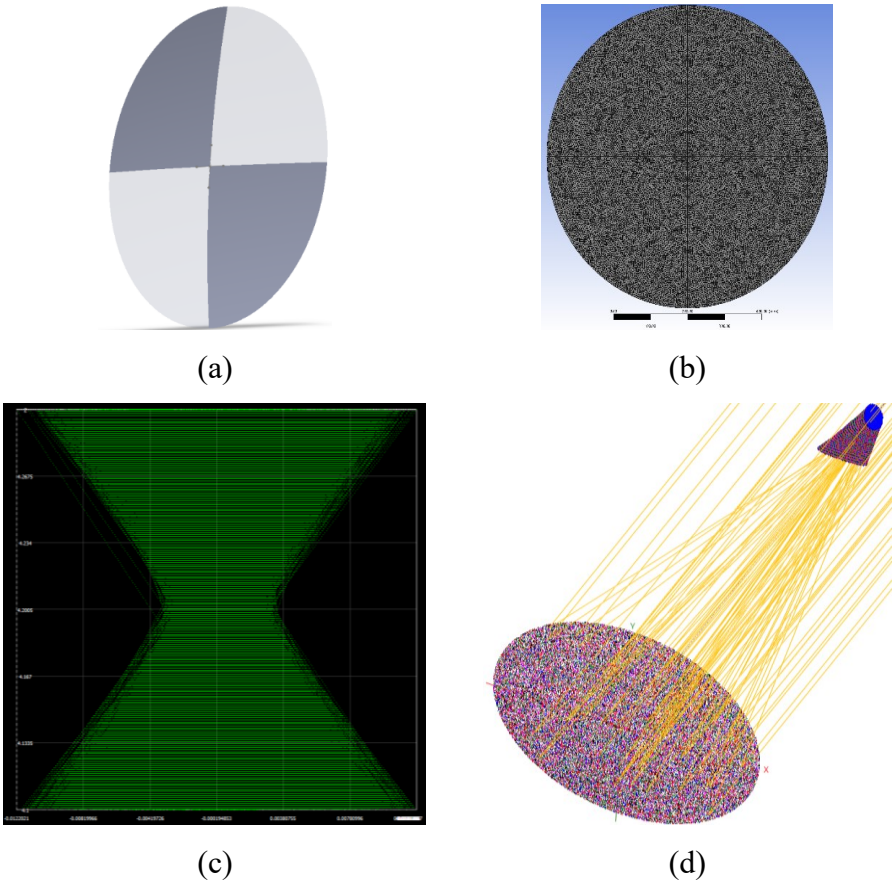

(a) (b)

(c) (d)

Figure 3-9: Analytical model setup process example (single facet): (a) SolidWorks CAD surface, which is meshed in ANSYS; and (b) imported into SolTrace 3.1; and then (c) viewed in SolTrace 2012.7.9 to locate (d) the focal point with the final simulation

Before the simulations took place, a mesh independence study was performed. This was critical as the model aimed to approximate a reflective surface with continuous curvature using flat surface elements. Having flat reflective surfaces that are too large would drastically impact on the optical performance of the facet due to the applied sun shape. Any non-parallel light that reflects off a flat surface will form an image that grows in size more drastically than a curved surface as the distance from the reflective surface to the target increases. With sufficiently small surfaces, this phenomenon

will have a negligible impact. By maintaining the membrane depth and location relative to a virtual target surface, five mesh densities were simulated, which ranged from 20 mm to 2.5 mm element sizes. Using a self-developed Python script that processes the comma-separated value (CSV) ray data on the target surface from SolTrace and generates intercept factor data and flux maps, the mesh independence could be performed. The code is explained in detail in Appendix C.3. The intercept factor curve profile is used to quantify mesh independence. Figure 3-10 shows that mesh densities with 5 mm and 2.5 mm elements produced very similar intercept factor curves. Therefore, mesh independence is reached from 5 mm elements onwards (especially in the geometric concentration ratio range of 100 –1 000, which was investigated) and will be used for all analytical studies discussed from here on. All characterisation simulations were simulated with 100 000 rays.

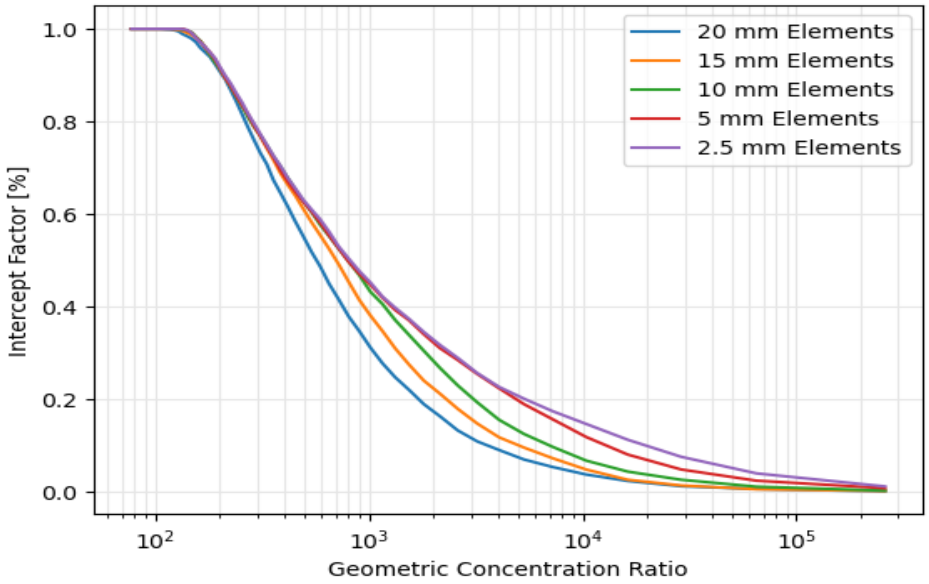

Figure 3-10: Mesh independence study using intercept factor versus geometric concentration ratio plots

3.4.4 Characterisation of elliptical surface

Once the numerical model setup process had been developed, and an acceptable mesh density had been identified, correlations of focal length versus membrane depth, as well as image translation versus facet tilt angle, needed to be investigated. This would allow for an accurate model of the full array to be created in SolidWorks. Additional behaviour was also investigated. This involved the validation of the assumption that the angle of incidence and angle of reflection are equal

relative to the facet's normal aperture and whether the focal length remains consistent as the tilt angle is increased. It is important to note that, given the dual focal length nature of the focal image, the first focal point was chosen in the formation of these correlations to achieve an accurate representation of the experimental model. The reason for this is that, in the lunar test, all the facets were aimed manually and by eye. When the first focal image was achieved, the membrane surface shape was fixed in place. The simulation also implemented the sun's angular diameter, reported as 0.53° by Goswami (2014), which is comparable to the moon's angular diameter of 0.518°, reported by Faulkner (1998). Furthermore, no optical errors were applied to the CAD surface. The sun's angle was applied because at no point would the facet be used with a perfectly parallel light source or collimated beam. The only controllable error would be the optical errors of the reflective surface applied in SolTrace.

Before the main optical error study, two secondary numerical tests aimed at generating a membrane depth versus focal length correlation and validation of a SolidWorks model took place in SolTrace. The first consisted of a series of elliptic paraboloid facets aimed directly at the sun with various membrane depths. The objective was to develop a correlation between the membrane depth and the focal length. The second objective was to investigate how far the image would translate laterally when the facet was tilted. In doing so, the focal length was checked to see if it remained constant at different tilt angles. The total ray deflection angle was also compared to an expected angle of twice the tilt angle to validate the assumption that the facet will behave similarly to a flat mirror where the angle of incidence is equal to the angle of reflection. All measurements of the results in SolTrace were accurate to the nearest millimetre by visually identifying which virtual target plane (spaced 1 mm apart) had the smallest image, as shown in Figure 3-9c.

Using the secondary test results from SolTrace, a parametrically driven SolidWorks model, developed by Swanepoel et al. (2020) in order to construct the full-array SolidWorks model for the main SolTrace study, was validated. The result of the definitive focal length versus membrane depth is presented in Chapter 4, while the provisional results for tilt angles versus focal image translation, as well as changes in focal length and resulting image angle due to facet tilt angle, are presented in Appendix D. The SolidWorks model, based on fundamental optical principles, consisted of the elliptic paraboloid surface with random points selected for incoming solar ray intersections. The ray had a 0.53° deviation applied to it to resemble the sun's angular diameter.

At the points of intersection on the surface, a normal vector was drawn. The ray reflection angle was then based on the angle the incoming ray made with the normal surface and was set to be equal. This was done for both extremes of the non-parallel ray. This resulted in an incoming and outgoing ray that was shaped like a cone, where the outgoing ray maintained a 0.53° angle that diverged towards the target surface. An example with two rays is shown in Figure 3-11.

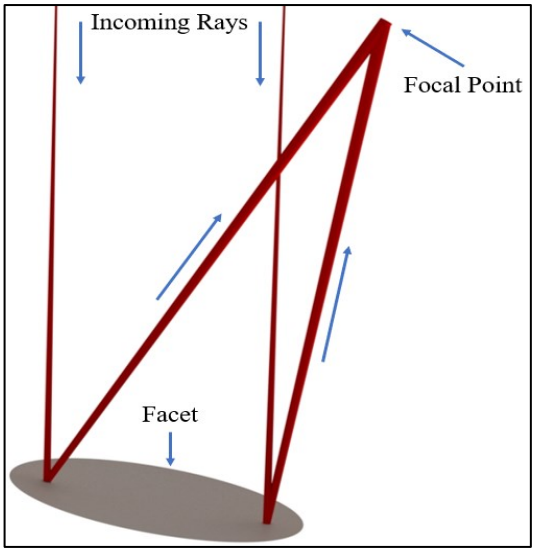

Figure 3-11: SolidWorks ray-tracing model at 10° tilt angle with a 25 mm membrane depth

3.4.5 Full-array optical error analysis

Using the SolidWorks ray-tracing model and the focal length versus membrane depth correlation that was found based on the Ellies satellite dish, the locations, membrane depths and tilt angles were calculated. Table 3-4 summarises the facet properties based on their respective locations within the array. The facet orientation is noted in Table 3-4 as some of the facets were mounted to tilt along their major axes instead of their minor axes due to design limitations as shown in Figure 3-4. They are denoted as "major" for tilt about the major axis and "minor" for tilt about the minor axis. The final-array CAD model consisting of elliptic paraboloid surfaces is shown in Figure 3-12.

For Ring 4b in Table 3-4, the different facet orientations require a different membrane depth for the same focal length. Figure 3-4 shows that the facets on the T-arm are rotated 90° in orientation compared to all other facets and are tilted along the major axis instead of the minor axis. This increases the projected aspect ratio (described in Figure 3-6), where tilting along the minor axis reduces the aspect ratio. This causes the dual focal lengths mentioned in section 3.4.1 to be further

apart from each other. This means that the first focal length is further away and will therefore have a smaller membrane depth. Because the experimental setup used the first focal length during the manual calibration process, this had to be done in the numerical model as well. The smallest focal image for the facet tilted about its major axis is, however, achieved with the stated membrane depth of 10 mm for a physical focal length of 3.31 m, although the apparent focal length is 4.19 m. If the facets in Ring 4b were orientated in the same way as all the facets, the membrane depth would have been 12.2 mm, like the facets in Ring 4a.

Table 3-4: Facet characteristics based on location in the array

Ring no	Facet orientation	Ring diameter [m]	Membrane depth [mm]	Focal length [m]		Facet tilt angle
				Facet focal length	Physical focal length	
1	Major	1.64	14.8	2.84	2.72	8.4°
2	Major	2.92	13.9	3.03	2.90	14.6°
3	Major	3.39	13.3	3.15	3.02	16.5°
4a	Major	4.43	12.2	3.31	3.23	21.0°
4b	Minor	4.43	10.0	4.19	3.25	21.0°
5	Major	5.12	11.2	3.75	3.41	23.7°

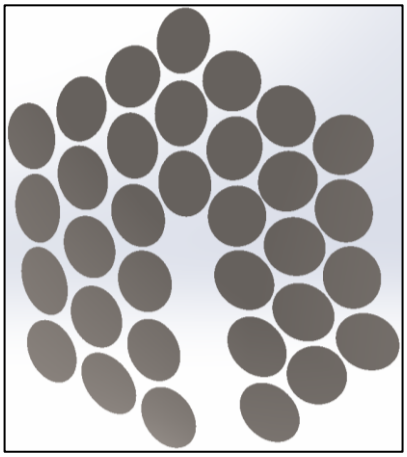

Figure 3-12: Elliptic paraboloid modelled in SolidWorks

With the full array modelled in SolidWorks fully defined, it was then meshed in ANSYS and imported into SolTrace. Simulations were set to run with 1 000 000 ray intersections on the target

surface, similar to work done by Craig et al. (2016) and Moghimi et al. (2015). This ensured that convergence was achieved with a uniform flux distribution on the virtual target surface. Another reason for the high ray count was to allow for the intersection data to be exported and converted into an image in a Python post-processor (see Appendix C.3). To get a respectably smooth contour map of the flux distribution with high resolution, small "pixel" sizes had to be used. In this instance, a pixel was defined as a square element with a user-defined height and width within the total image space. This could also be described as a mesh with square elements overlaying the image. If a ray fell within the pixel element boundaries, it was counted to form a pixel intensity value with the pixel centroid as the x and y coordinates for that pixel. With these image parameters, low ray intersections would result in zero-value pixels giving the flux map a speckled appearance. The 1 000 000 ray intersections still produced zero-value pixels among the high-intensity flux region, but these were greatly minimised and were therefore not noticeable at the selected resolution of 3 162 × 3 162 pixels, which produces a 10 megapixel image array. To perform the optical error study, the total optical error was modified in SolTrace as part of a parametric study. This concluded the final step of the analysis setup process. A summary of the analysis process (discussed in sections 3.4.2 to 3.4.5) is shown in figures 3-13 and 3-14.

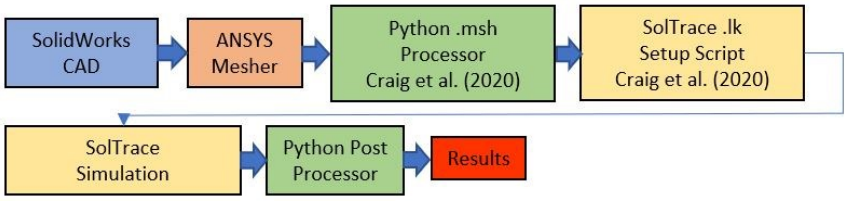

Figure 3-13: Core analysis flow diagram

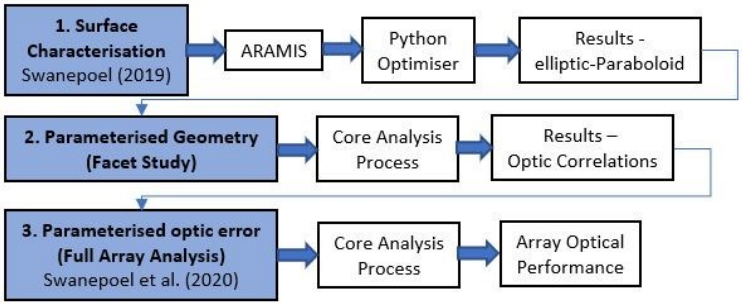

Figure 3-14: Analytical process summary

3.5 Conclusion

Analytical and experimental methods were presented to analyse the optical performance of a multifaceted solar dish built on the roof of the Engineering 2 Building at the University of Pretoria. The experimental procedure made use of a full moon as a substitute for the sun due to its similar angular diameter and used minimal testing equipment. This allowed for the safe testing of a solar concentrator that could prove dangerous if safety procedures were not followed. It also allowed for a more accurate Lambertian target surface to be used repetitively without being damaged by high-intensity flux.

The analytical model procedure detailed a method for importing custom surfaces into SolTrace. Using a parametrised approach, correlations could be developed between the facet characteristics (dimensions, orientation and location) and the optical behaviour, such as focal length and image location. These correlations were then used to accurately model the full dish array in SolidWorks. Performing another parametric optical error study could then quantify the optical error present in experimental results.

The following section presents the results obtained from the experimental and analytical methods and discusses their significance.

4. Results

4.1 Introduction

This chapter presents the results obtained following the experimental and analytical procedures discussed in Chapter 3. The results from the preliminary investigation of the accuracy of RAW and JPEG image formats are presented and discussed. The light pollution treatment results are also presented for two methods using dark edges as the pollution baseline and imposing a pollution baseline using artificial light pollution. The main results of the performance of the current work are then compared with two different setups in a discussion highlighting sources of error and areas for further study.

4.2 Experimental results

Using the lunar flux mapping technique presented in section 3.3, the resulting flux ratio distributions of the dish setup are presented below for tests performed on 14 September 2019. Preliminary investigations into the experimental methods were also done.

4.2.1 RAW image

Figure 4-1: Photographic image of the target board taken 2.93 m away

The RAW image captured during testing is shown in Figure 4-1. The image was captured after all 33 facets were manually focused and aimed at the target surface, while the tracking system was manually aimed at the moon. Figure 4-1 is the best result, as calibration was difficult due to manual tracking.

4.2.2 Preliminary testing

The following results form part of a preliminary investigation into the experimental methods used. Experimental means of city light pollution treatment, including a case where artificial light pollution is imposed, were investigated along with two types of image formats (RAW and JPEG).

4.2.2.1 RAW and JPEG comparison

The first investigation concerns the negative effect of using 8-bit JPEG images for flux mapping instead of RAW 14-bit images. Bit depths above 14-bit are available for more accurate flux representation with other camera models. A JPEG image is less memory intensive and is easier to process than its RAW counterpart. However, the image compression algorithm (lossy compression) that is used when an image file is saved in JPEG format prioritises visually impactful (intensity or brightness) information and discards information that is generally not noticeable to the human eye (Rabbani & Jones, 1991). With JPEG images, full intensity (luma) data is kept from the RAW file version and colour data is subsampled, also known as chroma subsampling. According to Hussain et al. (2018), cosine-based correlations are used to estimate the distribution of pixel information in a JPEG image. This leads to inaccuracies in the image detail (known as artefacts). An example of this effect in a JPEG compressed version is evident in the bullseye (sharp central dip) in Figure 4-2. This phenomenon is most noticeable at large compression ratios, especially if exceptionally fine detail is present in the image. Rabbani and Jones (1991) further report on the RMSE after JPEG compression using discrete cosine transform (DCT) ranging from 2.56 to 14.78, depending on the bit rate used for compression, which in the case of figures 4-2 and 4-3 is 1.5 to 0.25 bits per pixel. Larger bits per pixel yield better quality in JPEG compressed images. It is thus justifiable to investigate how well the intercept factors of the JPEG images compare to those of the RAW images.

Images are generally not compressed when they are saved in RAW format. However, current camera models possess the capability to do so. Compression of the RAW image file is a lossless process (reversible), which means that pixel information is not lost after compression. RAW (CR2)

image files are compressed through mathematical formulas that can be fully reversed when the file is decompressed during opening.

Both file type cases (RAW and JPEG) are presented for images that have not been corrected for light pollution. Transects presented in figures 4-2 and 4-3 show the normalised flux ratio, defined by Equation (3.4), along the transverse distance of the target surface in the *x* and *y* planes through the weighted centroid of the flux. Note that each of the normalised flux distributions does not reach its peak (1.0) along the centroidal planes that were used. This is due to the fact that the flux distribution does not follow an ideal normal shape and results in the peak flux occurring offset from the weighted centroid of the lunar flux distribution on the target surface.

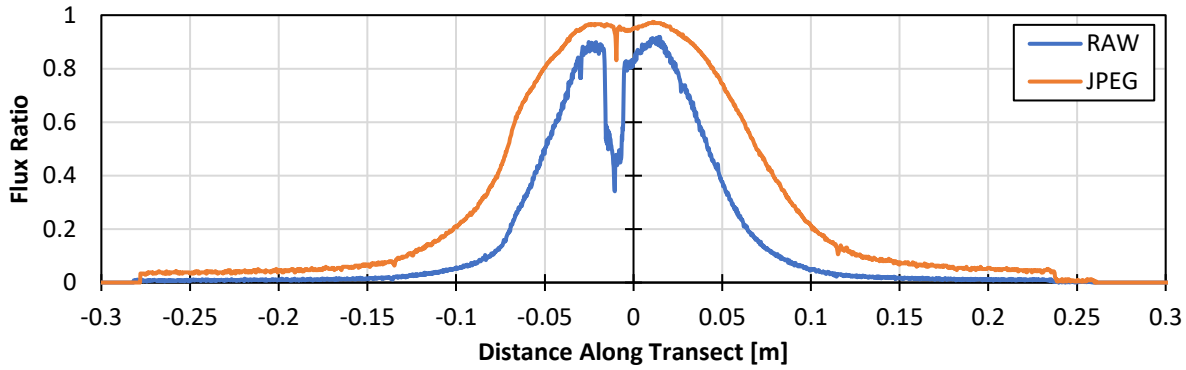

Figure 4-2: Comparison between RAW and JPEG images with transects through the *x*-plane of the flux image without light pollution correction

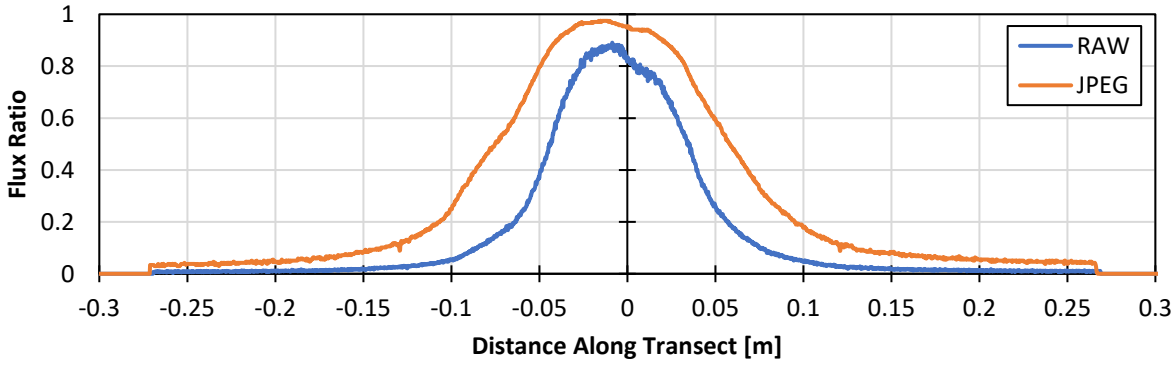

Figure 4-3: Comparison between RAW and JPEG images with transects through the *y*-plane of the flux image without light pollution correction

Figures 4-2 and 4-3 show a difference in the result of captured flux. The JPEG image, known as a lossy compressed image, overestimates the distributed flux as it is only capable of intensity values between 0 and 255. Steep pixel gradients, therefore, lead to transiency in the correlations, causing image distortion along contrasting edges in the image. This is known as ringing artefacts. Gradient information is lost in this process as adjacent pixels are approximated to have similar values in a step to compress the 16 384 shades of colour per RGB channel in a 14-bit RAW image file to 256 shades of colour per RGB channel in an 8-bit JPEG image. To counteract distortion or blurred edges and other inaccuracies after JPEG compression, the camera implements sharpening through post-processing by increasing pixel values in certain areas. Spatial aliasing takes place, causing the high-contrast regions to have an exaggerated jagged boundary, as well as increased pixel values through post-process sharpening in the JPEG image. This effect is shown by the sharp drop in Figure 4-2 due to a black cross drawn on the target surface.

4.2.2.2 Light pollution treatment comparison

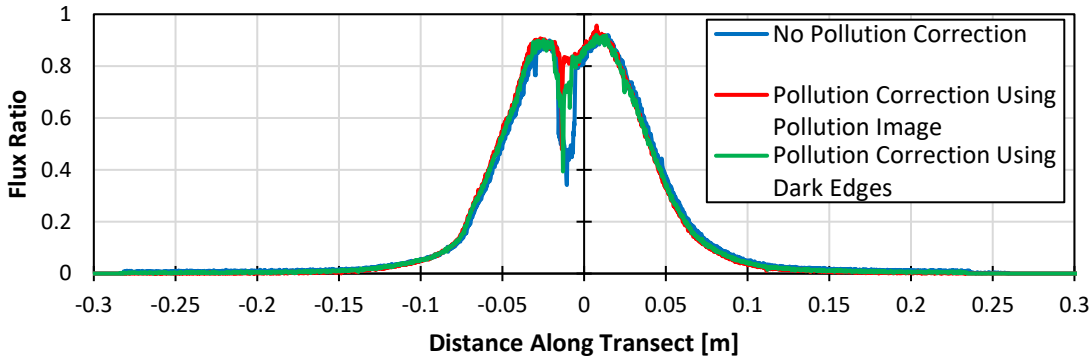

Figure 4-4: Light pollution treatment transects in the *x*-plane

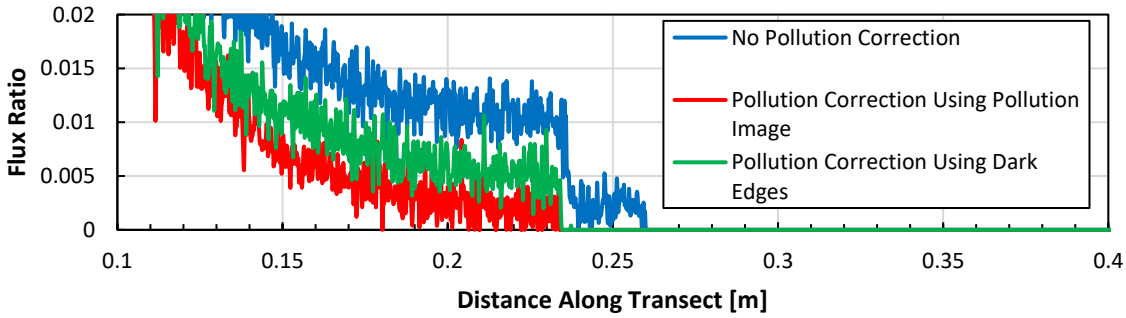

Figure 4-5: Light pollution treatment transects in the *x*-plane (detailed view of target edge)

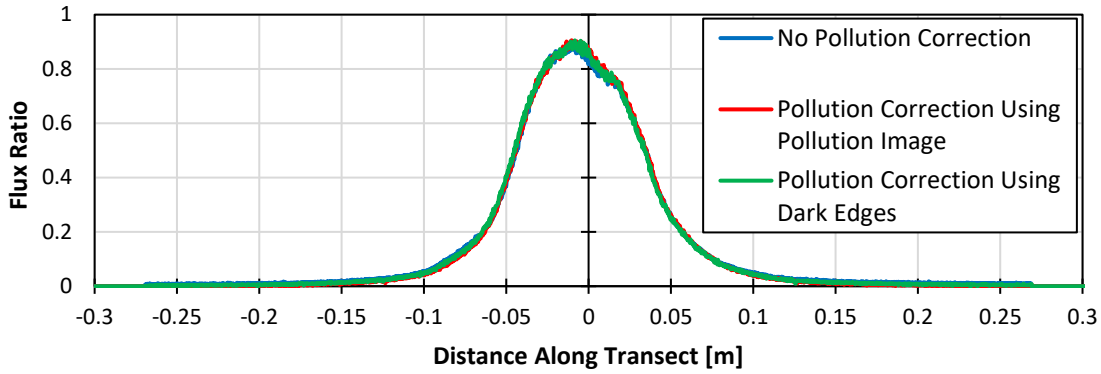

Figure 4-6: Light pollution treatment transects in the *y*-plane

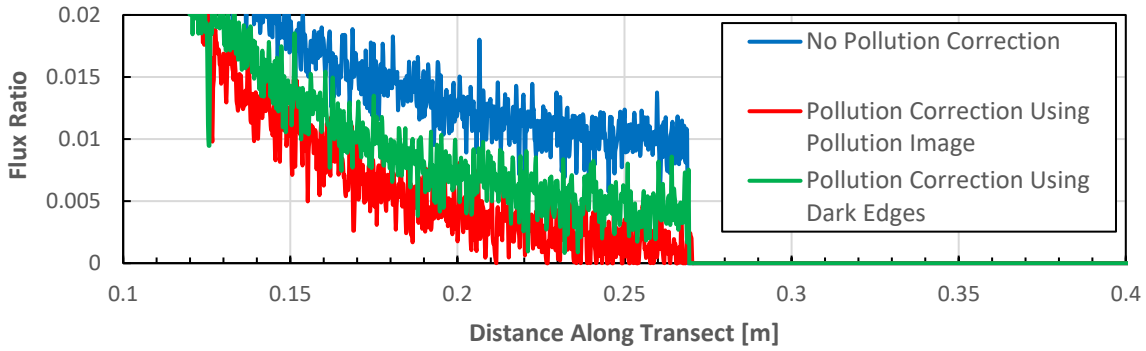

Figure 4-7: Light pollution treatment transects in the *y*-plane (detailed view of target edge)

The second comparison is done with regard to the light pollution treatment methods investigated. Transects of the same RAW image, corrected by the two aforementioned light pollution approaches (see section 3.3.1), are presented with the untreated images.

Figures 4-4 to 4-7 present the effects of light pollution treatment on the distribution. They provide visual examples of how light pollution treatment can affect the intercept factors obtained. The two treatment methods mainly affect the low-level pixel values in the flux distribution. Using artificial light pollution, the edges of the target surface were dropped down closer to zero compared to the other treatments. Note that the sharp dip in Figure 4-4 is a result of having a black cross drawn on the target surface to indicate the target centre during the calibration process.

4.2.2.3 Initial intercept factor comparison

Figure 4-8 presents the intercept factors of the same image with different light pollution treatments for both RAW and JPEG formats. As an example, the resulting intercept factors for an aperture zone with dimensions of 0.25 m × 0.25 m ($CR_{g,ap}$ = 249) are summarised in Table 4-1.

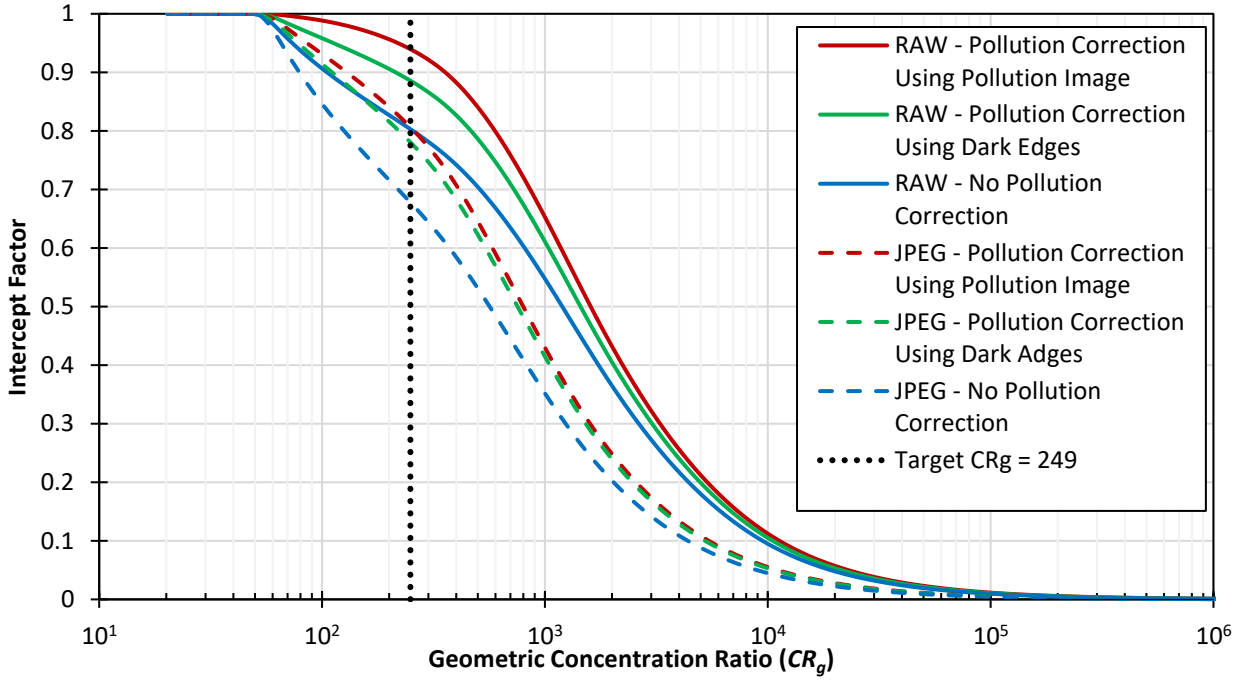

Figure 4-8: Intercept factor as a function of geometric concentration ratio

Table 4-1: Multifaceted dish intercept factors for $CR_{g,ap}$ = 249 using various pollution treatments

	No pollution correction (%)	Pollution correction using pollution image (%)	Pollution correction using dark edges (%)
RAW	80.3	94	88.6
JPEG	67.8	80.6	78.1

Here, the exaggerated distribution of the flux caused by JPEG images is demonstrated again. The intercept factor curves for JPEG-based calculations all perform 12% to 16% below their RAW counterparts. The effect of light pollution treatment methods is also evident. The conservative method, where averaged target border values are considered for the baseline pixel intensity, predicts

intercept factors between the two extremes: no light pollution correction and light pollution correction using the average pixel intensity of the artificial light pollution image as the baseline.

The preliminary investigations demonstrated the negative effect that JPEG images introduce to the analysis process. The artificial light pollution treatment process helped in reducing the non-uniform, dynamic city light pollution experienced during testing, but still requires additional development. Further results are therefore presented for RAW format images treated for city light pollution using the average from the target surface edges as the baseline pollution value (the more conservative method).

4.2.3 Flux ratio maps and transects

In this section, normalised flux maps are presented with city light pollution treatment using the target edges as the baseline pollution value for RAW format images. Transects through the *x* and *y* planes at the weighted centroid of the flux (not the peak flux value) are presented.

The resulting transects are presented in Figure 4-9 with the boundaries of an aperture zone with dimensions of 0.25 m × 0.25 m also shown. Note that the sharp dip in the *x*-plane is a result of a black cross drawn on the target surface to indicate the target centre. A 3D surface plot and contour plot of the distribution are shown in Figure 4-10.

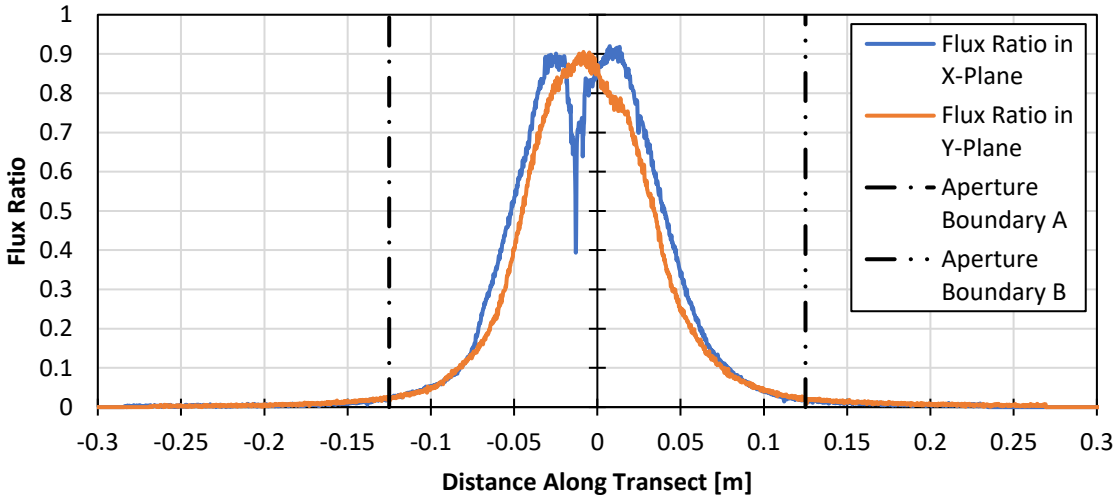

Figure 4-9: Transects in *x*-plane and *y*-plane

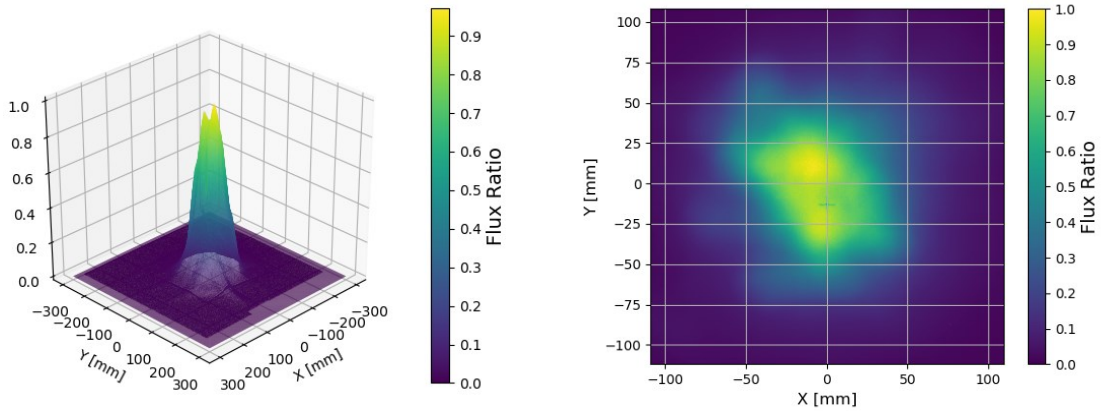

(a) (b)

Figure 4-10: (a) 3D surface plot of the flux ratio; and (b) contour plot of the flux ratio

4.2.4 Intercept factors

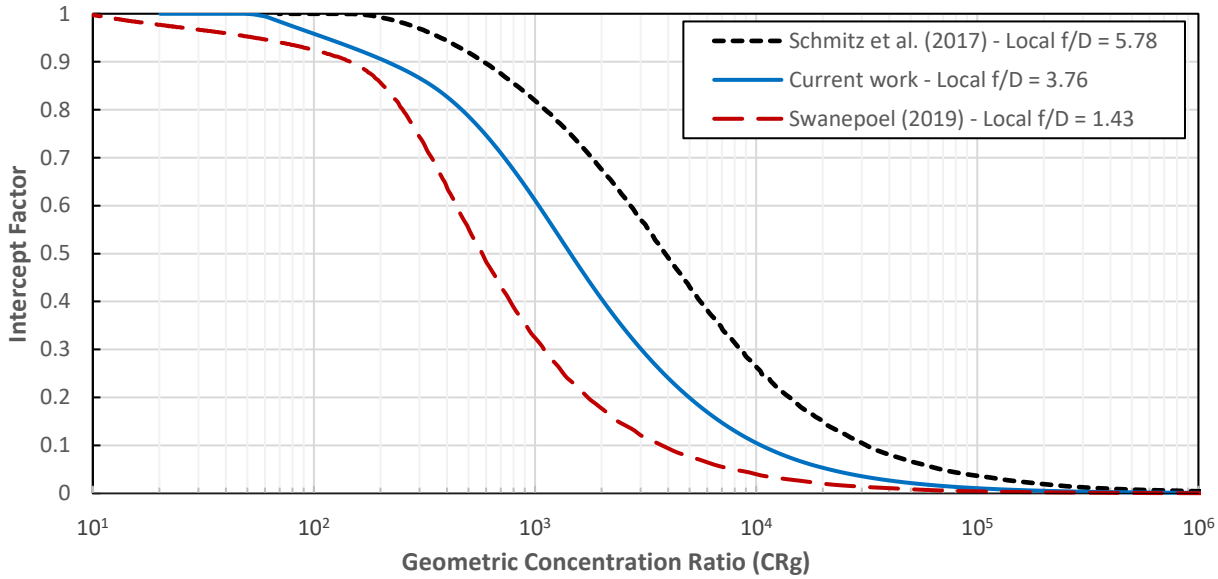

Figure 4-11: Optical performance comparison with the dish setups of Schmitz et al. (2017) and Swanepoel (2019)

Based on the flux ratio maps, the intercept factor for the current dish setup was calculated as 88.6% for an aperture size of 0.25 m × 0.25 m. A smaller six-facet dish was also constructed (Swanepoel, 2019) in unison with the larger dish setup investigated in this work. The performance between the two systems could be compared as they used the exact same facet construction and only differed in total array size (see Table 4-2). The presented intercept factor graph in Figure 4-11 follows the

same trend as Swanepoel (2019) and Schmitz et al. (2017). The results and the comparison of the results are further discussed in section 4.2.5.

Table 4-2: Comparison of intercept factors shown in Figure 4-11

	Swanepoel (2019)	**Current work**		**Schmitz et al. (2017)**
Number of facets	6	33		18
Global rim angle, $\psi_{rim,G}$	45	46		28
Average local *f/D* ratio, ϕ_L	1.49	3.97		5.59*
Dish global diameter, D_G (m)	1.6	4.98		2.4*
Global focal length, f_G (m)	0.97	2.93		3
Global *f/D* ratio, ϕ_G	0.6	0.59		1.25*
Virtual dish area, A_{virt} (m^2)	2.01	19.5		4.52*
Total reflective area, A_{refl} (m^2)	2.70	15.57		4.28
Receiver target area, A_{ap} (m^2)	$(0.135)^2$	$(0.25)^2$	$(0.1217)^2$	$(0.06)^2$
Geometric concentration ratio, CR_g	148.4	249	1 189	1 189
Intercept factor (%)	89.9	88.6	55.9	78.3

* Represents estimated values

4.2.5 Discussion

Schmitz et al. (2017) managed to obtain an intercept factor of 78.3% for their 60 mm × 60 mm receiver, using 18 facets with 0.2 mm silvered aluminium sheeting as the reflector material. The performance of the dish setup investigated in the current work is compared at the same geometric concentration ratio as that of Schmitz et al. (2017) at 1 189 in Table 4-2. This results in an equivalent target surface size of 121.7 mm × 121.7 mm for the current dish setup with an intercept factor of 55.9%. Table 4-2 shows that, at the same geometric concentration ratio of 1 189, the current dish setup underperforms that of Schmitz et al. (2017). The average local *f/D* ratio of the facets used in the setup of Schmitz et al. (2017) was ϕ_L = 5.59, while for the current dish setup, the average local *f/D* ratio was ϕ_L = 3.97. However, it should be noted that the current dish setup had three facets missing because of its receiver arm design (see Figure 3-4). Furthermore, the projected area of each facet in Schmitz et al. (2017) had an aspect ratio of 1, which was not the case for the current dish setup (see Table 3-1). According to Zanganeh et al. (2012), a higher intercept factor can be expected for projected facet aspect ratios of 1. However, the advantage of the current work is that the facets

were constructed using easily available and affordable off-the-shelf products such as satellite television dishes and aluminised BOPET membranes. The performance of the current dish setup could be further improved by mounting the facets on the fourth ring (Ring 4a in Table 3-1) in such a way that they are orientated in a manner similar to the other facets in the setup (see Figure 3-4). The performance can be further improved by having a better aiming strategy for facets – facets can be calibrated and aimed individually (while the other facets are not aimed) using an accurate and automatic lunar tracking system instead of manual tracking and aiming.

Figure 4-11 also shows that the performance of the smaller dish setup by Swanepoel (2019) is lower than that of the current dish setup for a fixed geometric concentration ratio. Note that the two setups have a similar global *f/D* ratio of $\phi_G \approx 0.6$ according to Table 4-2. The comparison in Figure 4-11 and Table 4-2 suggests that increased performance is to be gained when the dish is designed with larger local *f/D* ratios, with the dish setup of Swanepoel (2019) having an average local *f/D* ratio of $\phi_L = 1.49$, and the current dish setup having an average local *f/D* ratio of $\phi_L = 3.97$. According to Murphy and Tuan (1987), spherical aberration effects become more apparent with smaller *f/D* values, and close parabolic approximation can be obtained for totally elastic membrane systems where ϕ_L is greater than 2. The performance of the dish setup of Swanepoel (2019) can therefore be increased by increasing the distance of the target board from the facets or decreasing the size of the facets, both of which would increase the local *f/D* ratio. However, it should also be noted that the dish setup of Swanepoel (2019) only had six facets, compared to 33 on the current dish setup, and that a reduced performance from one of the facets in the smaller setup would have a more significant effect on the intercept factor. Furthermore, after the testing period, creep was evident in the smaller dish setup, where a more drastic vacuum was drawn to achieve the concentrated image due to the smaller local *f/D* ratio. The magnitude of the creep experienced on the dish setup of Swanepoel (2019) was evident as it showed wrinkling when the membrane was not under vacuum. This was due to the fact that the tension induced was closer to the yielding point of the material. Evidence of creep on the current dish setup's facets was not present. The current 33-facet dish setup only required the membrane centres to depress on average by approximately 12 mm. The introduction of creep in the membrane would cause the initial tension (albeit slight) to diminish over time. Additional deformation will therefore be needed to achieve the required surface, but will result in an image that is focused on a plane away from the receiver

aperture, closer to the dish array. This will create a larger focused image at the receiver and reduce the intercept factor and performance of the concentrator.

4.3 Concentration ratios

In this section, a test case is considered where the dish setup investigated in this work would experience a DNI of 1 000 W/m^2. The reflectivity of the BOPET membrane used in the dish facets was determined to be 96.88% through UV-VIS spectroscopy, courtesy of the Physics Department at the University of Pretoria.

A Bio-100 spectrometer was used to determine the spectral absorptivity and spectral transmissivity of a BOPET membrane sample. The sample was analysed for a spectral waveband between 330 nm and 850 nm, which accounted for 89% of the total spectrum captured by the CMOS camera sensors.

Using the flux ratio maps generated in section 4.2.3, the peak solar flux intensity value (I_{max}) could be estimated. The peak solar flux was determined using a Python code, presented by Swanepoel (2019), which minimised the RMSE between the approximated solar radiation at the aperture and the calculated value using the test case DNI (see section 3.3.2). Swanepoel (2019) used the Nelder-Mead optimisation algorithm as the solver for the objective function (Nelder & Mead, 1965). For a test case with a solar DNI of 1 000 W/m^2 and a facet reflectivity of 0.97, the optimiser determined the maximum solar flux to be 1 395 kW/m^2 and 523 kW/m^2 for the 33-facet dish setup (current work) and the six-facet dish setup of Swanepoel (2019), respectively. The resulting solar flux maps are presented in Figure 4-12. For both setups, the total incident radiation on the target surface was approximated by the optimiser to within 10^{-3} W when compared to the target surface radiation calculated using the DNI. The peak solar concentration ratio was also determined using Equation (4.1), which describes the degree to which the reflected solar radiation gets concentrated at the target surface. The resulting peak solar concentration ratios for the 33-facet and the six-facet dish setups were 1 438 and 539, respectively.

$$CR_{r,peak} = \frac{I_{max}}{\rho_{dish} DNI} \qquad (4.1)$$

It should be noted that errors due to the difference in the moon and solar spectrum, the camera sensor and a non-perfect Lambertian surface were assumed to be negligible in this work. Errors due to the curvature of the camera lens, the target surface not being orientated perfectly perpendicular to the

camera and human error in determining the vertices of the target surface in the image were also assumed to be negligibly small. Furthermore, the possibility of moonlight reflecting from a small portion of a facet's curved rim area onto the target board was not investigated and the potential effects of this phenomenon on the results were assumed to be negligible.

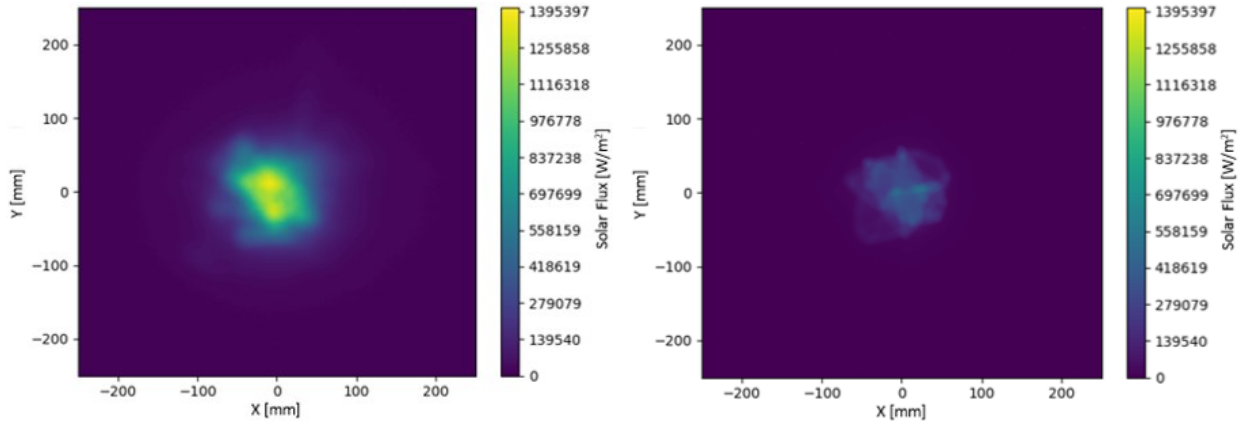

(a) (b)

Figure 4-12: Estimated solar flux map with a DNI of 1 000 W/m^2 for: (a) the 33-facet dish setup (current work) with a peak flux of 1 395 kW/m^2; and (b) the six-facet dish setup of Swanepoel (2019) with a peak flux of 523 kW/m^2

4.4 Analytical results

As described in section 3.4.4, facet characterisation needed to take place to be able to accurately model the full array in SolidWorks. Additional optical behaviour was also investigated. This included determining whether the focal length remained constant at different facet tilt angles, as well as validating a preliminary assumption that the incident and reflected angle of a ray of light would be equal to that of a flat mirror due to its dual focal length nature. The results of these additional investigations can be found in Appendix D as they did not result in fully defined correlations due to their multivariable interdependencies. However, the preliminary investigation showed that the focal length decreases from the focal length defined by the membrane depth as the tilt angle of the facet increases. Validation of the assumption that rays are reflected with a total angle equal to twice the tilt's angle was also successful (see Appendix D). The results of the focal length versus membrane depth study, as well as the optical error analysis, are presented below for a facet supported by a 757.5 mm × 820 mm elliptical satellite dish.

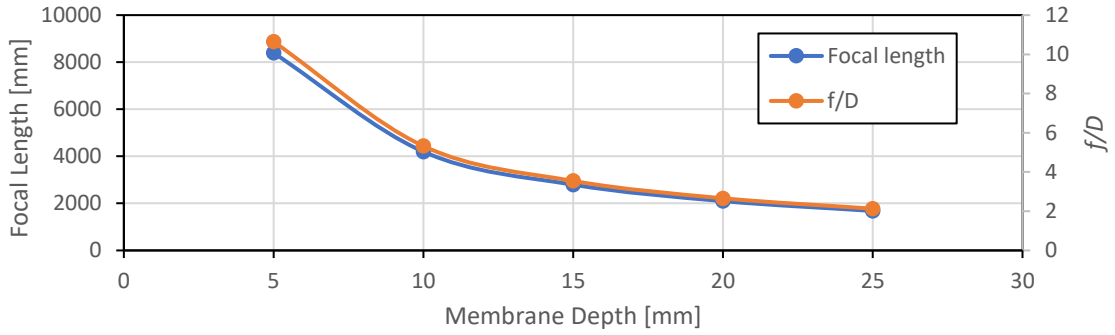

Figure 4-13: Focal length versus membrane depth

$$f = 41978d^{-1} \qquad (4.2)$$

The focal length versus membrane depth study, unlike the other additional studies in Appendix D, is independent of all other variables that describe the facet location, orientation or membrane material. Figure 4-13 shows a plot of the membrane depth (defined as the depth at the membrane centre) versus focal length. Equation (4.2) expresses the facet focal length, f (in mm) as a function of the membrane depth, d (in mm). As expected, smaller membrane depths yield larger focal lengths with a hyperbolic nature (also known as a reciprocal function). Considering that the gradient of the function decreases very slowly as the focal length increases, suggests that the application of this specific size facet will be difficult to achieve for systems with very large focal lengths of above 10 m. This is because, at large focal lengths, a very small change in membrane depth will result in a large change in focal length. Achieving the accuracy required for the membrane depth will therefore require more sophisticated manufacturing processes to allow for accurate vacuum control. To achieve optimal performance, a minimum *f/D* of 2 is required, as stated by Murphy and Tuan (1987). Designing an array with elliptical facets (757.5 mm × 820 mm) with focal lengths of above 2 m and below 7 m will be more achievable and still yield high performance. Using the result from Equation (4.2) and the validation results in Appendix D, a full array simulation was run in SolTrace to yield Figure 4-14.

Figure 4-14: Completed SolTrace simulation of the 33-facet array

The full array model was simulated using 1 000 000 intersecting rays, while applying a sun shape of 0.53° using the pillbox function in SolTrace. A parametric optical error analysis was done with optical errors ranging from 10 mrad to 20 mrad according to Equation (4.3) (Wendelin et al., 2013). The resulting flux data at the target was then processed with a Python script (see Appendix C.3) to yield intercept factor plots integrated from the weighted centroid, as was done in section 4.2.3, as well as contour plots of the flux distribution. An intercept factor plot is presented in Figure 4-15, which shows the performance of the array with different optical errors, along with the results of the lunar test and that of Schmitz et al. (2017).

$$\sigma_{optical} = \sqrt{4\sigma_{slope}^2 + \sigma_{specularity}^2} \qquad (4.3)$$

Figure 4-15 shows that, with an increase in optical error, the focal image grows and therefore the curve moves towards the left along the *x*-axis. The location of the curve along the *x*-axis and the shape of the curve provide information about the concentrated image. The lunar test results showed an intercept factor of 88.6% for a geometric concentration ratio of 249. Figure 4-15 shows that a 17.5 mrad optical error produced comparable results to that of the moonlight test by achieving an 88.8% intercept factor at the same geometric concentration ratio. However, the curve only matches

the location along the *x*-axis, but not the profile of the moonlight results. Therefore, another source of error needs to be quantified: facet alignment error, where the goal of the experimental setup was to achieve a single point of focus. This error describes the distribution of high-intensity flux zones on the target surface.

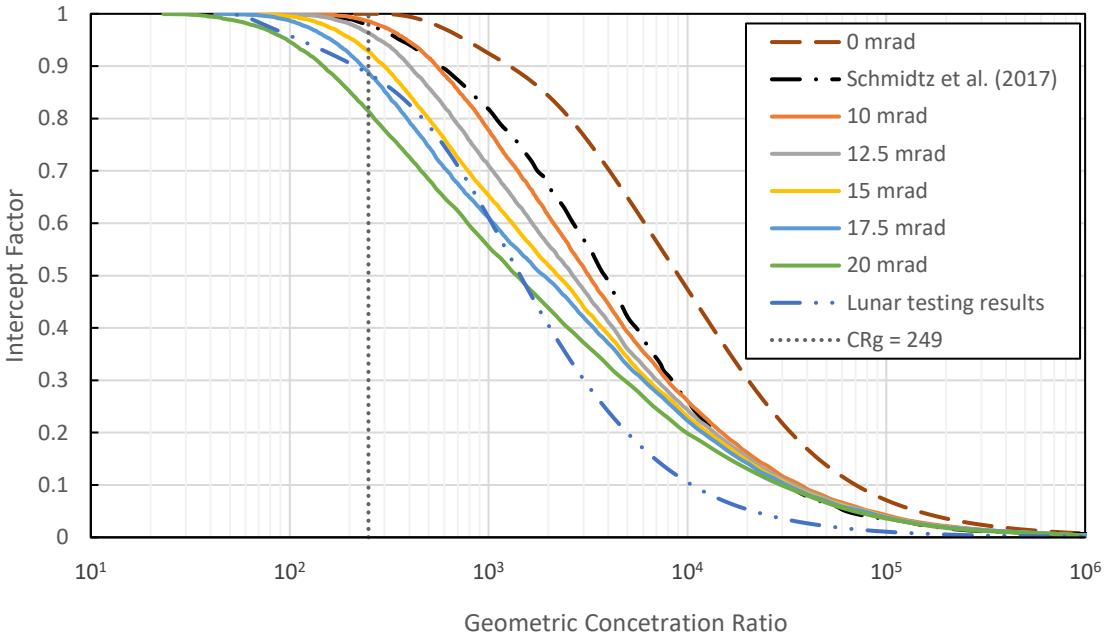

Figure 4-15: The intercept factor versus the geometric concentration ratio of the multi-faceted reflector as a function of optical error. SolTrace flux mapping results are compared with an experimental result from Schmitz et al. (2017).

Considering the shape discrepancy between the intercept factor plots of the numerical model and that of the moonlight test in Figure 4-15, it is evident that the experimental facets possess a lower optical error and a prominent alignment error. This error is to be expected according to findings of Good et al. (2016) that state that Mylar film is a highly specular material and therefore does not make a large contribution to the total optical error. Figure 4-15 also shows that, if the total error can be reduced to 10 mrad, the setup will have a similar performance to Schmitz et al. (2017).

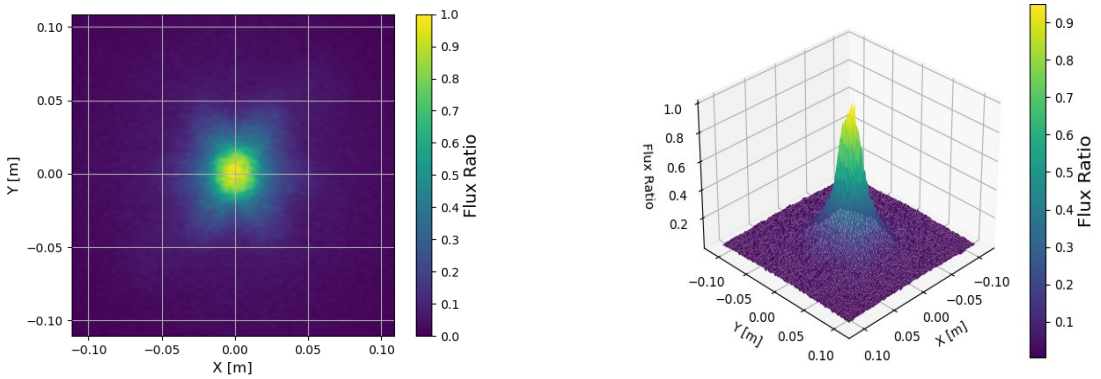

(a) (b)

Figure 4-16: (a) Contour plot; and (b) 3D surface plot for 17.5 mrad optical error from SolTrace simulation

To quantify the aiming and slope errors, further investigation is required where random alignment errors are applied to individual facets in the CAD model to determine the extent of all the contributing factors. The analytical model presents a focal image where all facets were aimed at the same point, creating an axisymmetric image around the bullseye in Figure 4-16. Figure 4-10 shows how the light was distributed on the target surface for the moonlight test. Note that the origin of the *x*-axis and *y*-axis is located at the weighted centroid of the flux in Figure 4-10b and Figure 4-16a. The centroid in Figure 4-10b diverges from the bull's-eye of the target surface on the *y*-axis, which is where the facets were supposed to be focused. Compared to Figure 4-16a, the moonlight flux ratio map in Figure 4-10b has its most intense flux around the centroid (instead of on the centroid). This distribution explains the shape of the curves in Figure 4-15. Low-level flux at the centroid with the peak flux situated around the weighted centroid will result in an intercept factor plot with an initially small gradient and then a sudden increase until the extremities of the flux are reached. In comparison, the intercept factor plots from the analytical results have a mostly constant gradient. It is clear that, for the moonlight test, all the facets were not successfully aimed at the same location on the target surface. Note that the flower-like petals in Figure 4-16 are due to the incorrectly oriented T-arm facets in the fourth ring. While the first focal point was adequately focused on the target surface, the second focal point was out of focus, causing spillage away from the high-flux centre.

4.5 Conclusion

Vacuum-membrane dish technology has been investigated to reduce the cost of building high-performance optical systems. A solar dish reflector setup that makes use of low-cost, commercial television satellite dishes as a support for aluminised BOPET membranes in a multifaceted approach was investigated. The facets were positioned in a hexagonal honeycomb arrangement, in the profile of a paraboloid, where each facet could be adjusted individually. The research presented a method to determine the expected solar flux distribution from lunar tests using a Canon EOS 700D camera with a CMOS sensor. Preliminary testing proved that JPEG image formats yielded insufficient accuracy in capturing the incident flux when compared to the RAW images. City light pollution treatment, using the dark target edges as the baseline, proved to be the most conservative method. An artificial light pollution treatment method was also considered, which yielded higher intercept factors. The performance of the low-cost dish setup, in terms of the intercept factor as a function of the geometric concentration ratio, was compared with results from setups by Schmitz et al. (2017) and Swanepoel (2019). For the dish setup of Swanepoel (2019), the comparisons showed that increased performance is to be gained when the dish is designed with larger local *f/D* ratios, as stated in the literature. Recommendations have been made for further improvements to the current dish setup because the results showed that it did not perform as well as the setup of Schmitz et al. (2017). However, the advantage of the current work is that the facets were constructed using easily available and affordable off-the-shelf products. Durability and feasibility studies are recommended for further industry-motivated research. Estimated solar flux maps for the 33-facet dish setup (current work) and the six-facet dish setup of Swanepoel (2019) were computed and compared using the flux ratio maps, DNI and facet reflectivity. The peak solar concentration ratios of the 33-facet and the six-facet dish setups were estimated at 1 438 and 539, respectively, for a test case considering a DNI of 1 000 W/m^2 and a dish reflectivity of 97%. The lunar flux mapping techniques proved to be effective and safe by using the incident light from the moon and standard camera equipment.

The numerical model showed that a total optical error of 17.5 mrad yielded comparable results to the moonlight test for the investigated dish setup. It also supported the findings of Good et al. (2016) that Mylar film is highly specular, as the discrepancy in the intercept factor plots indicated that the main source of optical error can be attributed to facet misalignment. The results, therefore, suggest that large performance improvements are to be achieved with a more accurate aiming strategy for the investigated dish setup.

5. Summary, conclusion and recommendations

5.1 Summary

A common issue faced when it comes to solar dish design is the complex trade-off between cost and optical quality. The optical performance of any solar dish is important as it directly affects the net power output of the solar energy system, such as the solar Brayton cycle system being developed on the roof of the Engineering 2 Building at the University of Pretoria. Vacuum-membrane dish technology has therefore been investigated to reduce the costs of building high-performance optical systems. A novel solar dish reflector setup that makes use of low-cost, commercial television satellite dishes as a support for aluminised BOPET membranes in a multifaceted approach was investigated. Experimental tests were conducted using lunar flux mapping techniques and different pollution treatment methods. A numerical model, based on the photogrammetry results of the membrane surface, was also developed in SolTrace to ascertain the sources of error and allow for further design improvements.

5.2 Conclusion

The design consisted of facets positioned in a hexagonal honeycomb arrangement in the profile of a paraboloid, where each facet could be adjusted individually. The research presented a method to determine the expected solar flux distribution from lunar tests using a Canon EOS 700D camera with a CMOS sensor. Preliminary testing proved that JPEG image formats yielded insufficient accuracy in capturing the incident flux when compared to the RAW images. City light pollution treatment using the dark target edges as the baseline proved to be the most conservative method. An artificial light pollution treatment method was also considered, which yielded higher intercept factors. The performance of the low-cost dish setup, in terms of the intercept factor as a function of the geometric concentration ratio, was compared with results from setups by Schmitz et al. (2017) and Swanepoel (2019). For the smaller dish setup of Swanepoel (2019), the comparisons showed that increased performance is to be gained when the dish is designed with larger local *f/D* ratios, as stated in the literature. Recommendations have been made for further improvements on the current dish setup because the results showed that it did not perform as well as the setup of Schmitz et al. (2017). However, the current work makes use of facets based on easily available and affordable off-the-shelf products. Estimated solar flux maps for the 33-facet dish setup (current work) and the six-facet dish setup of Swanepoel (2019) were computed and compared

using flux ratio maps, a test case DNI of 1 000 W/m^2 and a facet reflectivity of 97%. The peak solar concentration ratios of the 33-facet and the six-facet dish setups were estimated at 1 438 and 539, respectively. The lunar flux mapping techniques proved to be effective and safe by using the incident light from the moon and standard camera equipment.

The numerical model, which discretised the reflective surface of the facets, proved to be effective in identifying the sources of optical error. The surface on the membrane, supported by an elliptical rim, was identified as an elliptic paraboloid through photogrammetry by Swanepoel (2019). Using this model, an accurate focal length versus membrane depth correlation was determined and used in a validated SolidWorks ray-tracing model to accurately aim the facets to yield the smallest image possible. A total optical error of 17.5 mrad with an intercept factor of 88.8% closely resembled the results from the moonlight test at 88.6%. Considering the shape discrepancy between the intercept factor plots of the numerical model and that of the moonlight test, it is evident that the experimental facets possess a lower optical error and a prominent alignment error. This error is to be expected according to findings of Good et al. (2016) that state that Mylar film is a highly specular material with small specularity error and highlights prominent improvements that can easily be implemented to increase performance, such as an improved aiming procedure to reduce aiming error during the calibration phase.

5.3 Recommendations

Potential areas for future work are discussed in this section. Important factors to consider are membrane durability, creep and vacuum regulation. It was found that the 50 μm aluminised BOPET film was quite vulnerable to punctures from sharp objects, as well as chemical and abrasion degradation of the deposited aluminium when exposed to dust, wind and rain. Furthermore, the membranes had to be cleaned in a somewhat delicate manner. Micro-fibre cloths and a hose with residential pressure (4 bar) and a nozzle on a medium setting did not appear to damage the membrane. However, multiple studies have been performed to test the durability of reflector materials and show that reflectivity decreases with exposure time (García-Segura et al., 2016; Kennedy & Terwilliger, 2005). According to Good et al. (2016), aluminised BOPET is not recommended for outdoor use without a resistant top layer for protection from weather and abrasion. Zanganeh et al. (2012) suggested an inflated air bubble made from transparent ethylene tetrafluoroethylene (ETFE) material to protect thin mirror membranes from dust, rain and wind.

On the other hand, weatherproofing layers result in a transmission loss, as well as additional losses due to scattering (Good et al., 2016). Furthermore, durability is dependent on exposure conditions, maintenance (cleaning), substrate material (base layer for mechanical support) and adhesion between the layers. Solar reflective films that are optimised for these conditions include ReflecTech (DiGrazia et al., 2010, the 3M Solar Mirror (Ho et al., 2011), MIRO-SUN, SAIC film (Kennedy & Terwilliger, 2005) and others mentioned by Good et al. (2016). Using reflective membranes that are optimised for these conditions will increase the optical efficiency, but also increase the cost. Durability and feasibility studies are recommended for further industry-motivated research. It is therefore recommended that a techno-economic analysis, as well as an environmental impact analysis, be performed in future work. Furthermore, the thickness of the aluminised BOPET membrane and its effect on durability can be further investigated.

The purpose of the current study was to develop a novel faceted reflector design and analyse its performance in a controlled environment. The primary mechanism of creep for the current stretched membrane design is expected to be the plastic deformation of the sheet over time. This would occur if a constant vacuum pressure were kept within the plenum of the facet and the aluminised BOPET membrane degraded with exposure to the environment. With a reduction in the strength of the sheet, the concavity would slowly deform beyond its ideal shape and thus result in a growth of optical error. Further testing is required to investigate the reduction in performance to gauge the magnitude of the creep experienced by an aluminised BOPET membrane. Future studies should also analyse the effects of temperature swings and thermal ratcheting. A control system can be used to adjust the membrane's shape at frequent intervals, similar to Butler and Beninga (1991), with the addition of ambient temperature monitoring to include an adjustment factor to the calibrated membrane distance. Because of the very low-pressure difference across the membrane, pinholes might result in manageable leaks that can be resolved with intermittent adjustment through a control system. Overall, it was found that some of the facets were able to hold a vacuum for almost a year.

The numerical model proved useful in developing correlations that aid in designing a multifaceted dish array for facets supported by an elliptical rim. Further research must be performed to determine the impact of elliptical rims with different aspect ratios. This will allow facets with a specific focal length and tilt angle due to their location in the array to be designed with a specific aspect ratio so

that the projected aspect ratio is always 1. A multivariable database consisting of all the empirical results from multiple parameterised studies can be developed as a design tool that will be fast and accurate for use in the design of multifaceted systems using elliptical facets. Simple user input values such as receiver location relative to the location of the facet and minor axis size of the facet can serve as inputs, and the required design dimensions and membrane depths will be returned to the user. To reduce the non-uniform nature of elliptical supports using Mylar film and obtain aspect ratios of 1, one can ensure that the machine direction of the Mylar film is oriented along the major axis of an elliptical support ring and the transverse direction along the minor axis. Doing so will allow the stress states that form along the major and minor axes to be closer to each other due to the different material properties present in the machine direction and transverse direction in the Mylar film. This will allow non-circular supports to achieve a more uniform surface.

Multi-faceted stretched membrane technology using commercial satellite television dishes possesses potential for future renewable solar projects. With new developments in materials and technology, its full potential can be recognised with further research and development.

References

3M Renewable Energy Division, 2012. 3M™ solar mirror film 1100, Minneapolis: 3M.

Alanod Solar, 2020. Products. [Online] Available at: https://alanod-westlake.com/products [Accessed 12 10 2020].

Almeco GmbH, 2015. Reflective surfaces for solar applications. [Online] Available at: https://www.almecogroup.com/uploads/generic_file/almeco_vegaenergy_eng_s302_01_2015-mail.pdf [Accessed 12 10 2020].

Alpert, D. J., Mancini, T. R., Houser, R. M., Grossman, J. W., Schissel, P., Carasso, M. Jorgensen, G., Scheve, M., 1991. Solar concentrator development in the United States. Solar Energy Materials, Volume 24, pp. 307−319.

Blackmon, J. B., 1985. Development and performance of a digital image radiometer for heliostat evaluation at Solar One. Journal of Solar Energy Engineering, Volume 107(4), pp. 315−321.

Borgnakke, C. and Sonntag, R. E., 2012. Fundamentals of thermodynamics, 8th edition. Singapore, SG: Wiley.

Brooks, M. J., Du Clou, S., Van Niekerk, J. L., Gauche, P., Leonard, C., Mouzouris, M. J., Meyer, A. J., Van der Westhuizen, N., Van Dyk, E.E. and Vorster, F., 2015. SAURAN: A new resource for solar radiometric data in Southern Africa. Journal of Energy in Southern Africa, 26, 2−10.

Burgess, G., Zapata, J., Chauvin, R., Shortis, M. R., Pye, J. D. and Preston, J., 2012. Three-dimensional flux prediction for a dish concentrator cavity receiver. In: Proceedings of SolarPACES 2012, Marrakech, Morocco.

Butler, B. L. and Beninga, K. J., 1991. Focus control system for stretched-membrane mirrors. United States Patent No. 5,016,998.

Cioca, M. and Wang, J., 2013. By the light of the silvery moon: Fact and fiction. Physics Education, Volume 48, pp. 360−367.

Coventry, J. and Andraka, C., 2017. Dish systems for CSP. Solar Energy, Volume 152, pp. 140−170.

Craig, K. J., Marsberg, J. and Meyer, J. P., 2016. Combining ray tracing and CFD in the thermal analysis of a parabolic dish tubular cavity receiver. Cape Town, South Africa, In: Proceedings of the 21st SolarPACES International Conference (SolarPACES 2015).

Craig, K. J., Slootweg, M., Le Roux, W. G., Wolff, T. M. and Meyer, J. P., 2020. Using CFD and ray tracing to estimate the heat losses of a tubular cavity dish receiver for different inclination angles, Solar Energy, Volume 211, pp. 1137−1158.

Dähler, F., Ambrosetti, G., Montoya-Zegarra, J. A., Schindler, K. and Steinfeld, A., 2016. High-concentration solar dishes based on pneumatic reflecting membranes. Solar Energy, Volume 124, pp. 89−100.

Dellar, K. E, Le Roux, W. G. and Meyer, J. P., 2020. Plate-style recuperator for a solar Brayton cycle using high-temperature sealant. Applied Thermal Engineering, Volume 177, 115439.

DiGrazia, M. and Jorgensen, G., 2010. Design flexibility and durability in reflecting solar applications. In: Proceedings of the 39th ASES National Solar Conference (SOLAR 2010), Phoenix, AZ, USA.

Department of Energy (DoE), 2020. Renewable energy: Solar power. [Online] Available at: http://www.energy.gov.za/files/renewables_frame.html [Accessed 27 10 2020].

DuPont Teijin Films, 2003. Technical information. [Online] Available at: https://usa.dupontteijinfilms.com/wp-content/uploads/2017/01/Mylar_Physical_Properties.pdf [Accessed 18 10 2020].

Faulkner, D. R., 1998. The angular size of the moon and other planetary satellites: An argument for design. [Online] Available at: https://creationresearch.org/angular-size-moon-planetary-satellites-argument-design/ [Accessed 31 10 2019].

Flugge, W., 1966. Stresses in shells. New York, NY: Springer.

Frei, O., 1982. Tensile structures. Cambridge, MA: MIT Press.

García-Segura, A., Fernández-García, A., Ariza, M. J., Sutter, F. and Valenzuela, L., 2016. Durability studies of solar reflectors: a review. Renewable and Sustainable Energy Reviews, Volume 62, pp. 453−467.

Gehlisch and Klaus, 1982a. Small solar power plants with large parabolic dish collector. Berlin, West Germany. In: Proceedings of the 4th International Solar Forum of the German Solar Energy Society.

Gehlisch and Klaus, 1982b. Large parabolic dish collectors with small gas-turbine, stirling engine or photovoltaic power conversion systems. In: Proceedings of the 17th Intersociety Energy Conversion Engineering Conference, Los Angeles, CA, USA.

Good, P., Cooper, T., Querci, M., Wiik, N., Ambrosetti, G. and Steinfeld, A., 2016. Spectral reflectance, transmittance, and angular scattering of materials for solar concentrators. Solar Energy Materials and Solar Cells, Volume 144, pp. 506−522.

Goswami, D. Y., 2014. Principles of solar engineering, 3rd edition. Boca Raton, FL: Taylor and Francis.

Gouveia, L. C. P. and Choubey, B., 2016. Advances in CMOS image sensors. Sensor Review, Volume 36(3), pp. 231−239.

Ho, C. K., Ghanbari, C. M., O'Neill, M. B. and Yuan, J. K., 2011. On-sun testing of a heliostat using facets with metallized polymer films. Albuquerque, NM: Sandia National Laboratories.

Ho, C. K. and Khalsa, S. S., 2012. A photographic method for concentrating solar collectors and receivers. Journal of Solar Energy Engineering, Volume 134 (041004-1), pp. 041004/1-041004/8.

Hussain, A. J., Al-Fayadh, A. and Radi, N., 2018. Image compression techniques: A survey in lossless and lossy algorithms. Neurocomputing, Volume 300, pp. 44−69.

Kennedy, C. E. and Terwilliger, K., 2005. Optical durability of candidate solar reflectors. Journal fo Solar Energy Engineering, Volume 127(2), pp. 262−269.

Khoshalm, B. H., 1983. 50-kW solar membrane concentrator. In: Proceedings of the 4th SOLERAS Workshop, Kansas City, MO, USA

Le Roux, W. G., 2016. Optimum tilt and azimuth angles for fixed solar collectors in South Africa using measured data. Renewable Energy, Volume 96, pp. 603−612.

Le Roux, W. G. and Meyer, J. P., 2016. Modelling the small-scale dish-mounted solar thermal Brayton cycle. In: Proceedings of SolarPACES 2015, Cape Town, South Africa, pp. 060002-1–060002-8. doi:10.1063/1.4949144.

Le Roux, W. G., 2018. Feasibility study of a hybrid small-scale dish-mounted solar thermal Brayton cycle with cogeneration. In: Proceedings of the 16th International Heat Transfer Conference (IHTC 2018), Beijing, China, pp. 7929−7936.

Lebourgeois, V., Bégué, A., Labbé, S. and Mallavan, B., 2008. Can commercial digital cameras be used as multispectral sensors? A crop monitoring test. Sensors, Volume 8, pp. 7300−7322.

Majka, M. and Majka, T. M., 2012. Healthy light source. World Susatainability Forum, Malopolska.

Mancini, T., Heller, P., Butler, B. and Osborn, B., 2003. Dish-stirling systems: An overview of development and status. Solar Energy Engineering, Volume 125(2), pp. 135−151.

Mapes, M., Hseuh, H. C. and Jiang, W. S., 1993. Permeation of argon, carbon dioxide, helium, nitrogen and oxygen through mylar windows. In: Proceedings of the 40th National AVS Symposium and Topical Conference, Orlando, FL, USA.

Mavis, C. L., 1988. 10 MWe solar thermal central receiver pilot plant heliostat and beam characterisation system evaluation. Albuquerque, NM: Sandia National Laboratories.

McNulty, D., 2016. Reflectivity measurements. Pocatello, ID: Idaho State University.

Mills, D., 2004. Advances in solar thermal electricity technology. Solar Energy, Volume 76(1−3), pp. 9−31.

Moghimi, M. A., Craig, K. J. and Meyer, J. P., 2015. A novel computational approach to combine the optical and thermal modelling of linear Fresnel collectors using the finite volume method. Solar Energy, Volume 116, pp. 407−427.

Murphy, L. M., 1987. Moderate axisymmetric deformations of optical membrane surfaces. Journal of Solar Energy Engineering, Volume 109(2), p. 111.

Murphy, L. M. and Tuan, C., 1987. The formation of optical membrane reflector surfaces using uniform pressure loading, Golden, CO: Solar Energy Research Institute.

National Aeronautics and Space Administration (NASA), 2017. Solar system exploration − our sun. [Online] Available at: https://solarsystem.nasa.gov/solar-system/sun/in-depth/ [Accessed 10 09 2018].

Nelder, J. A. and Mead, R., 1965. A simplex method for function minimization. The Computer Journal, Volume 7(4), pp. 308−313.

Pye, J., Coventry, J., Venn, F., Zapata, J., Abbasi, E., Asselineau, C.A., Burgess, G., Hughes, G., and Logie, W., 2017. Experimental testing of a high-flux cavity receiver. In: Proceedings of SolarPACES 2016, Abu Dhabi, UAE.

Rabbani, M. and Jones, P. W., 1991. Digital image compression techniques, 7th edition. Bellingham, WA: Optical Engineering Press.

SAURAN, 2018. SAURAN. [Online] Available at: http://www.sauran.net/ShowStation.aspx?station=5 [Accessed 12 10 2020].

Schmitz, M., Ambrosetti, G., Steinfeld, A. and Cooper, T., 2017. On-sun optical characterisation of a solar dish concentrator based on elliptical vacuum membrane facets. Solar Energy, Volume 153, pp. 732−743.

Siangsukone, P., Burgess, G. and Lovegrove, K., 2004. Full moon flux mapping the 400m^2 "Big Dish" at the Australian National University. In: Proceedings of the 42nd Annual Conference of the Australian and New Zealand Solar Energy Society (ANZSES 2004), Perth, Australia.

Slootweg, M., Craig, K. J. and Meyer, J. P., 2019. A computational approach to simulate the optical and thermal performance of a novel complex geometry solar tower molten salt cavity receiver. Solar Energy, Volume 187, pp. 13−29.

SolarGIS, 2019, Solar resource maps and GIS data for 200+ countries. [Online] Available at: https://solargis.com/maps-and-gis-data/overview [Acessed 12 10 2020].

Starodubtsev, S. V., Umarov, G. Y. and Kordub, N. V., 1965. A 2.7-meter diameter vacuum film solar concentrator. Geliotekhinka, Volume 1(16).

Stine, W. B. and Geyer, M., 2001. Power from the sun, 2nd edition. Hoboken, NJ: Wiley.

Strachan, J. W. and Houser, R. M., 1993. Testing and evaluation of large-area heliostats for solar thermal applications. Albuquerque, NM: Sandia National Laboratories.

Stynes, J. K. and Ihas, B., 2012. Slope error measurement tool for solar parabolic trough collectors: Preprint. Golden, CO: National Renewable Energy Laboratory.

Sumner, R., 2014. Processing RAW images in MATLAB. Santa Cruz, CA: Department of Electrical Engineering, UC Santa Cruz.

Swanepoel, J. K., 2019. Helically coiled cavity receiver for a micro-scale direct generation steam Rankine cycle using novel solar dish design. Thesis: University of Pretoria, Pretoria, South Africa.

Swanepoel, J. K., Roosendaal, C. and Le Roux, W. G., 2020. Photogrammetry analysis of a vacuum-membrane solar dish using elliptical television antennas. Presented at the 26th Annual SolarPACES Conference (SolarPACES2020).

Truscello, V. C., 1979. The parabolic concentrator. Pasadena, CA: Jet Propulsion Laboratory.

Ulmer, S., Reinalter, W., Heller, P., Lupfert, E. and Martínez, D., 2002. Beam characterization and improvement with a flux mapping system for dish concentrators. Journal of Solar Energy Engineering, Volume 124(2), pp. 182−188.

Van Bakel, B. L., 2018. Development of a high concentration solar flux mapping system. Thesis: University of KwaZulu-Natal, Durban, South Africa.

Wendelin, T., Dobos, A. and Lewandowski, A., 2013. SolTrace: A ray-tracing code for complex solar optical systems. Golden, CO: National Renewable Energy Lab.

Wolff, T. M., Le Roux, W. G. and Meyer, J. P., 2018. Analysis of parabolic dish solar collector via lunar flux mapping. In: Proceedings of the 5th Southern African Solar Energy Conference (SASEC 2018), Durban, South Africa.

Zanganeh, G., Bader, R., Pedretti, A., Pedretti, M. and Steinfeld, A., 2012. A solar dish concentrator based on ellipsoidal polyester membrane facets. Solar Energy, Volume 86, pp. 40–47.

Appendices

Appendix A – Ellies 75 cm satellite dish

Appendix B – Additional images of experimental setup

Appendix C – Python and MATLAB Code

- C.1: RAW image processor for moonlight test images – MATLAB
- C.2: RAW graphics and intercept factor post-processor – Python
- C.3: SolTrace CSV post-processor – Python

Appendix D – Additional numerical results

Appendix A Ellies satellite dish specifications sheet

75cm Satellite Dish

Product Code: DE75

- 1 year warranty
- Easy to assemble

75cm satellite dish

Ideal for high definition satellite reception.
Outdoor installation

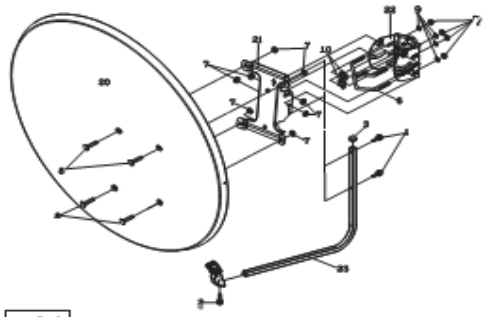

NO.	ITEM	DESCRIPTION	Q'TY
25		40mm LNB CLAMP	1
24		40mm LNB CLAMP HOLDER	1
23		LNB Arm	1
22		F/Mast Bracket	1
21		Reflector Bracket	1
20		Reflector	1
10		M6*15 round-head screw	4
9		M6 Washer	4
8		M6*15 Round Flat Head Square Screw	4
7		M6 flange nut	12
6		M6*W53 U Square bolt	2
5		M4 hex nut	1
4		M4*20 Round-head cross screw	1
3		cover	1
2		M6*12 hex-head cap screw w/sw/w	1
1		M6*30 hex-head cap screw w/w	2

TECHNICAL INFORMATION

Specifications:	
Item & Spec.	**DE80**
Offset Angle	22.75
Effective Physical Size (cm)	W75xH81
Focus Length (mm)	492
S-band Gain @ 2.5GHZ	25.7dB
C-band Gain @ 4.0GHZ	-
Ku-band Gain @ 12.5GHZ	38.63dB
Elevation	15°~75°/10°~80°/0°~90°
Azimuth	0°~360°
Aperture Efficiency	75% (min)
F/D Ratio	0.65
Weight	4.5kg
Material	Mild Steel
Finishing	Polyester Powder
Color	Gray/Cool Gray
Standard Mount	G/P/W
Pole diameter Acceptable (mm)	38~50
Ambient Temperature	-40°~+60°C
Relative Humidity	0~100%

THE PACKAGE CONTAINS

1 x (75cm x 81cm) Satellite Dish

PACKAGE DIMENSIONS

Height (mm)	Depth (mm)	Width (mm)	Weight (kg)
870	84	935	8.5

www.ellies.co.za

ELSAT

Reference: Ellies Electronics, 2020. Elsat 75Cm Dish – Ellies Electronics. [Online] Available at: https://www.ellies.co.za/product/elsat-75cm-offset-dish/ [Accessed 8 11 2020].

Appendix B Additional images of the experimental setup

Additional images of the experimental setup are shown below, including the tracking system, facet design and control system.

Figure B.1: Pneumatic line with solenoid and wiring used to control individual facet vacuum pressures. Pneumatic and electrical ring-line visible on the support frame.

Figure B.2: Moonlight test with the target board in view

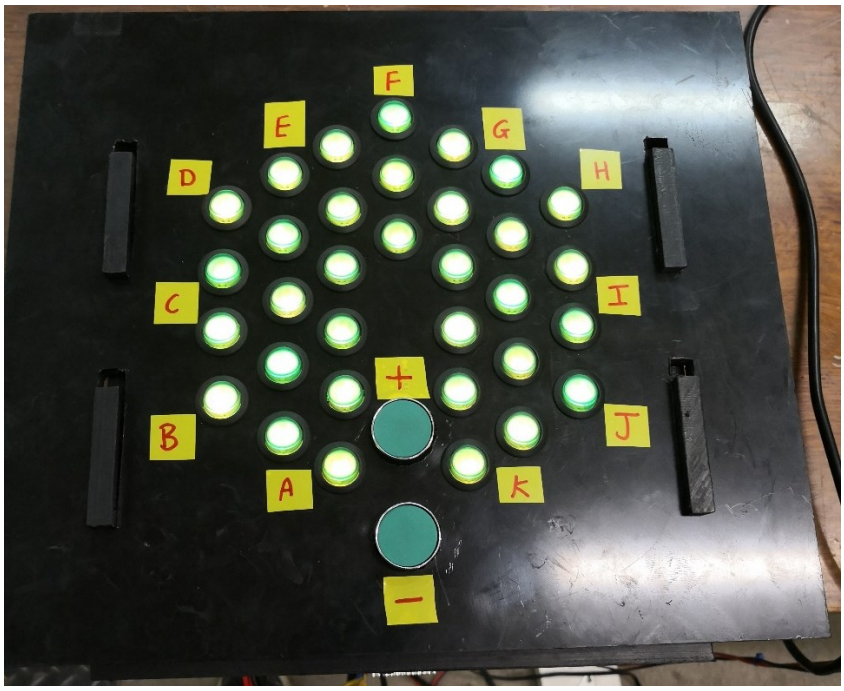

Figure B.3: Analogue control board with solenoid, vacuum pump and compressor controls

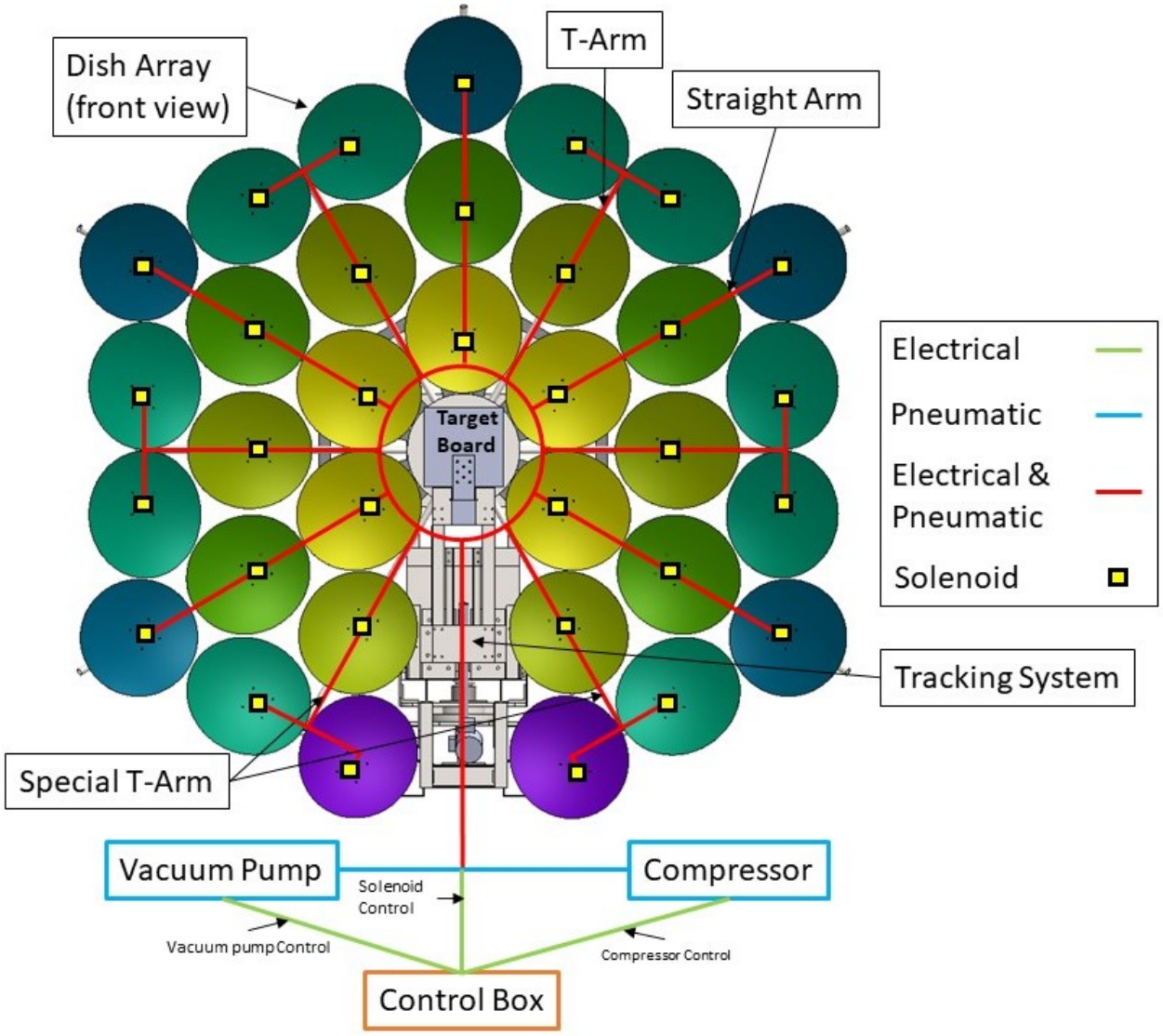

Figure B.4: Pneumatic and electric layout diagram for the control system

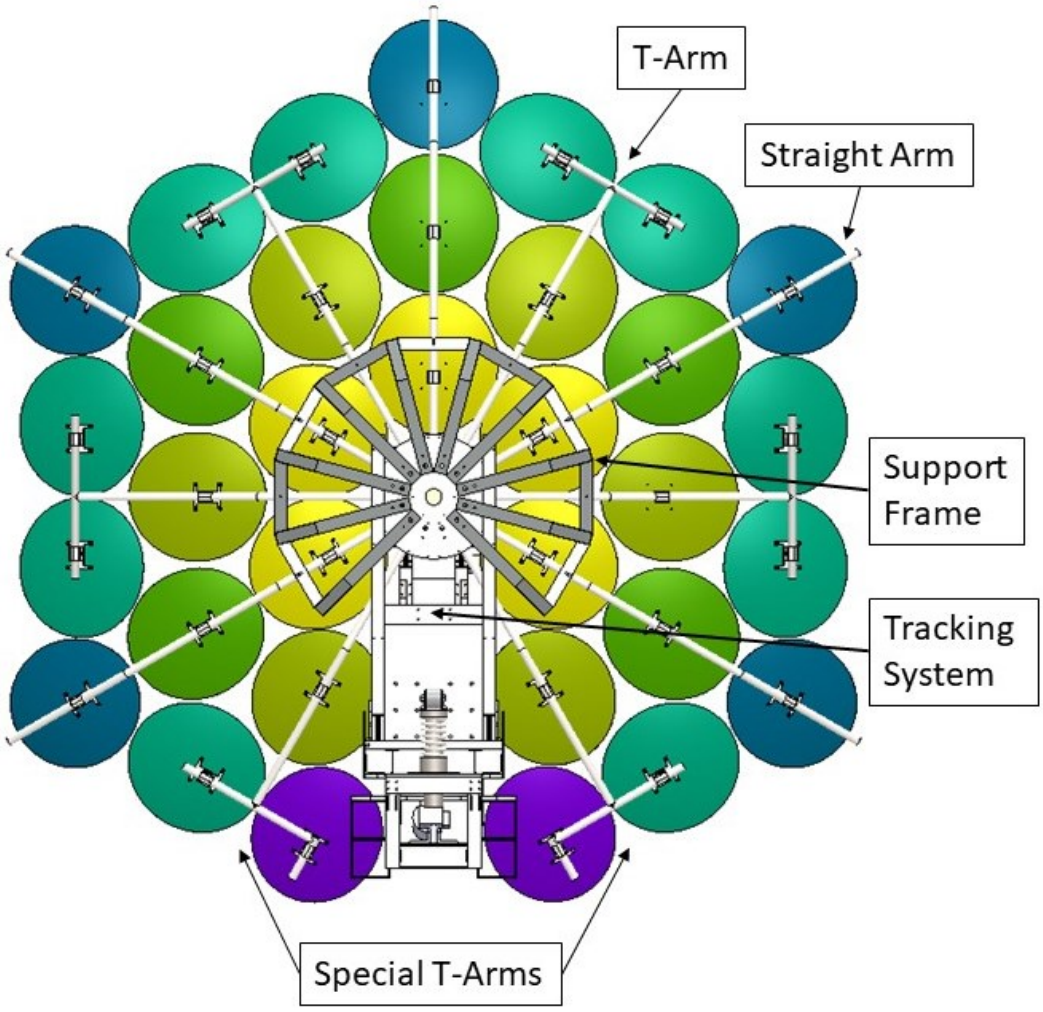

Figure B.5: Rear view of the array showing dish arm layout and support frame

Appendix C Python and MATLAB Code

Appendix C.1 RAW Image Processor for Moonlight Test Images – MATLAB

C.1.1 Introduction

The code presented below processes the image file from the moonlight test. This specific version deals with the Delaware National Guard (DNG) image formats based on methods described by Sumner (2014). Another version of this code was used for processing JPEG images that required a simple image-loading process native to MATLAB and is therefore not presented. The MATLAB code was used to process various pollution approaches as well. The code presented in section C.1.7 deals with artificial light pollution treatment. Sections of the code also deal with the other pollution treatment methods. To select which treatment was used, certain functions within the code were deactivated. However, all the functions will be discussed below.

C.1.2 Image extraction

The initial section deals with the extraction of the RAW image data from the DNG file as it consists of three images: a RAW image, a JPEG and a thumbnail. After accessing the image, it was cropped to the active sensor region that was stored in the Exif metadata (referred to as metadata from here on), when the image was taken based on the camera aspect ratio settings. The image was then de-linearised as some camera models compress the raw image using non-linear transformation stored with the mapping values found in a linearisation table in the metadata. White balance correction was also applied to the image by scaling each colour channel in the colour filter array. This was done using white balancing coefficients in a dot-multiplication mask (multiplication matrix) found in the metadata, with the green channel typically set to 1 and the red and blue values based on ratios relative to the green channel. The image was then demosaiced using a built-in MATLAB function to generate a 2D image matrix with elements representing pixels. Each pixel entry then contained a list of the RGB intensity values. The image was then turned into a grayscale image with single intensities for each pixel by averaging the RGB intensities. This concluded the image loading process used in the code. For artificial pollution treatment, images with the flux and added artificial pollution were loaded. For the case where the averaged boundary pollution treatment was used, images that only contain the concentrated flux were loaded.

C.1.3 Manual corrections

Once the image had been fully processed, manual corrections were applied. The first correction was to rotate the image based on the coordinates of the top vertices of the square target board. This was done manually by plotting the original image using a surface plot and the built-in functionality of the MATLAB plotting GUI to select the vertices in question returning the pixel index. The index values were used to calculate the rotation that was present relative to the horizontal plane, and the image was then rotated back to achieve the correct orientation.

The second correction was to crop the image to the target board boundary as the night sky was also part of the original image. This allowed the flux on the target board to be isolated. This was done in a similar manner to the rotation correction by selecting the bottom left and top right corners and using their index values to crop the image.

C.1.4 Pollution treatment

The first treatment case involved importing a raw image of the target surface, which only contained artificial light pollution from a uniform point source. The same manual rotation and cropping correction as mentioned above was applied. After processing the base pollution image, an average pixel value was calculated and subtracted from every pixel in the flux image to yield an image that only had the concentrated incident flux intensities from the solar collector based on artificial pollution correction.

The second pollution treatment method assumed that the intensities of the pixels on the edges of the target board were only due to ambient pollution and therefore had dark edges if ambient pollution was not present. For this treatment, a moonlight image with no added pollution had to be imported. The borders of the target surface were averaged to yield the baseline pollution intensity value, which was then subtracted from every pixel from a flux image that did not contain pollution. This produced a flux image where the pixel intensities only resulted from the solar collector, based on the dark edge assumption.

C.1.5 Normalisation

The images in both treatment cases were then normalised. The maximum pixel value was determined after correction and divided throughout the whole image matrix. After normalisation, the images were added to a padded array of zeros and the weighted centroids were calculated. The weighted centroid served as the axis origin for the images, as well as the starting point for the calculation of the intercept factor.

C.1.6 Intercept factor calculation

The intercept factor was calculated by integration, starting at the centroid pixel, and can be referred to as a zone. The zone was then grown in each successive loop by a single pixel around the centroid pixel as shown in Figure C.1.

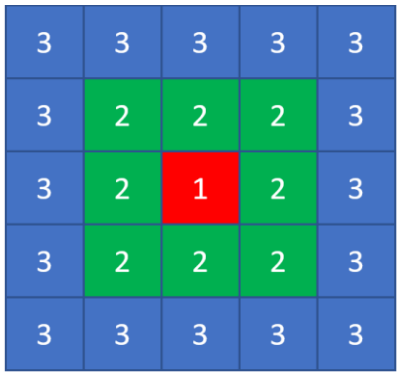

Figure C.1: Intercept factor integration pattern

The sum of the intensities in each zone was calculated and divided by the sum of the intensities on the whole target surface, producing an intercept factor value. The area of the zone was also calculated and the target surface area was known. Dividing the total target surface area by the number of pixels on the target surface yielded an area per pixel value. The square root of this value was also the length of a square pixel. After calculating the intercept factor, the geometric concentration ratio was calculated by dividing the total projected reflective surface area of the solar concentrator by the zone area. As mentioned before, the image was added to a padded array of zeroes. This allowed the integration to go beyond the boundaries of the target surface and ensured that every non-zero pixel was captured. The intercept factor and geometric concentration ratios were then appended to lists.

The final steps included saving the normalised flux image matrix, the image coordinate matrices, the intercept factor and the geometric concentration ratio list in .mat files for further processing in the code presented in Appendix C.2.

C.1.7 MATLAB code

```
clc
clear all
%% Load Flux Image and Process Raw Bayer Data
%READING RAW BAYER DATA AND CROPPING TO ACTIVE REGION (Sumner, 2014)
filename = 'E:\Honours\MSS732 Research Study\Deathray 2\CR2\DNG\FLUX_ART_POLL.DNG'; % Put file name here
warning off MATLAB:tifflib:TIFFReadDirectory:libraryWarning
t = Tiff(filename,'r');
offsets = getTag(t,'SubIFD');
setSubDirectory(t,offsets(1));
raw = read(t); % Create variable 'raw', the Bayer CFA data
close(t);
meta_info = imfinfo(filename);
% Crop to only valid pixels
x_origin = meta_info.SubIFDs{1}.ActiveArea(2)+1; % +1 due to MATLAB indexing
width = meta_info.SubIFDs{1}.DefaultCropSize(1);
y_origin = meta_info.SubIFDs{1}.ActiveArea(1)+1;
height = meta_info.SubIFDs{1}.DefaultCropSize(2);
raw = double(raw(y_origin:y_origin+height-1,x_origin:x_origin+width-1));

%LINEARISING, BLACK/WHITE CORRECTION AND FIXING BAD PIXELS (Sumner, 2014)
if isfield(meta_info.SubIFDs{1},'LinearizationTable')
   ltab=meta_info.SubIFDs{1}.LinearizationTable;
   raw = ltab(raw+1);
end
black = meta_info.SubIFDs{1}.BlackLevel(1);
saturation = meta_info.SubIFDs{1}.WhiteLevel;
lin_bayer = (raw-black)/(saturation-black);
lin_bayer = max(0,min(lin_bayer,1));

%WHITE BALANCING (Sumner, 2014)
wb_multipliers = (meta_info.AsShotNeutral).^-1;
wb_multipliers = wb_multipliers/wb_multipliers(2);
mask = wbmask(size(lin_bayer,1),size(lin_bayer,2),wb_multipliers,'rggb');
balanced_bayer = lin_bayer .* mask;
temp=uint16(balanced_bayer/max(balanced_bayer(:))*2^16);
lin_rgb=double(demosaic(temp,'rggb'))/2^16;

%Normalising Image
[X,Y,Z]=size(lin_rgb);
```

```
flux=zeros(X,Y);
for i=1:X
   for j=1:Y
      pix=lin_rgb(i,j,:);
      flux(i,j)=(pix(1)+pix(2)+pix(3))/Z;
   end
end
fluxV2=uint16(flux*(2^16-1));

%% Figure(1) - Original Flux Image
figure(1)
surf(fluxV2,'FaceColor','interp','Edgecolor','interp')
axis equal
colormap jet(1000)
title('Original Flux Image')
view(0,90)

%% Calculate Flux Image Angle of Rotation
%CALCULATE ANGLE OF ROTATION
%coordinates for corners of top edge
x1=1525;
y1=271;
x2=3989;
y2=194;
width=x2-x1;
height=y1-y2;
theta=atand(height/width);
fluxV3=imrotate(fluxV2,-theta);

%% Figure(2) - Rotated Flux Image
%rotated image
% figure(2)
% surf(fluxV3,'FaceColor','interp','Edgecolor','interp')
% axis equal
% colormap jet(1000)
% title('Rotated Flux Image')
% view(0,90)

%% Crop Flux Image to Full target Size

%CROP IMAGE TO FULL TARGET SIZE
%botoom left corner
xbl=1623;
ybl=320;
%top right corner
xtr=4075;
```

```
ytr=2787;
xdif=xtr-xbl;
ydif=ytr-ybl;
fluxV4=fluxV3(ybl:ybl+ydif-1,xbl:xbl+xdif-1);

%% Figure(3) Cropped Flux Image
figure(3)
surf(fluxV4,'FaceColor','interp','Edgecolor','interp')
axis equal
colormap jet(1000)
title('Cropped Flux Image')
view(0,90)

%%
% ########################################################################
% ------------------- Pollution ------------------
% ########################################################################

%% Load Pollution Image and Process Raw bayer Data
%READING RAW BAYER DATA AND CROPPING TO ACTIVE REGION (Sumner, 2014)
filename = 'E:\Honours\MSS732 Research Study\Deathray 2\CR2\DNG\ART_POLL.DNG'; % Put file name here
warning off MATLAB:tifflib:TIFFReadDirectory:libraryWarning
t = Tiff(filename,'r');
offsets = getTag(t,'SubIFD');
setSubDirectory(t,offsets(1));
raw = read(t); % Create variable 'raw', the Bayer CFA data
close(t);
meta_info = imfinfo(filename);
% Crop to only valid pixels
x_origin = meta_info.SubIFDs{1}.ActiveArea(2)+1; % +1 due to MATLAB indexing
width = meta_info.SubIFDs{1}.DefaultCropSize(1);
y_origin = meta_info.SubIFDs{1}.ActiveArea(1)+1;
height = meta_info.SubIFDs{1}.DefaultCropSize(2);
raw = double(raw(y_origin:y_origin+height-1,x_origin:x_origin+width-1));

%LINEARISING, BLACK/WHITE CORRECTION AND FIXING BAD PIXELS (Sumner, 2014)
if isfield(meta_info.SubIFDs{1},'LinearizationTable')
   ltab=meta_info.SubIFDs{1}.LinearizationTable;
   raw = ltab(raw+1);
end
black = meta_info.SubIFDs{1}.BlackLevel(1);
saturation = meta_info.SubIFDs{1}.WhiteLevel;
lin_bayer = (raw-black)/(saturation-black);
lin_bayer = max(0,min(lin_bayer,1));

%WHITE BALANCING (Sumner, 2014)
```

```
wb_multipliers = (meta_info.AsShotNeutral).^-1;
wb_multipliers = wb_multipliers/wb_multipliers(2);
mask = wbmask(size(lin_bayer,1),size(lin_bayer,2),wb_multipliers,'rggb');
balanced_bayer = lin_bayer .* mask;
temp=uint16(balanced_bayer/max(balanced_bayer(:))*2^16);
lin_rgb=double(demosaic(temp,'rggb'))/2^16;

[X,Y,Z]=size(lin_rgb);
poll=zeros(X,Y);
for i=1:X
   for j=1:Y
      pix=lin_rgb(i,j,:);
      poll(i,j)=(pix(1)+pix(2)+pix(3))/Z;
   end
end
pollV2=uint16(poll*(2^16-1));

%% Figure(4) - Original Pollution Image
figure(4)
surf(flux2V2,'FaceColor','interp','Edgecolor','interp')
axis equal
colormap jet(1000)
title('Original Pollution Image')
view(0,90)

%% Calculate Pollution Image Angle of Rotation
%CALCULATE ANGLE OF ROTATION
%coordinates for corners of top edge
x1=1542;
y1=366;
x2=4003;
y2=266;
width=x2-x1;
height=y1-y2;
theta=atand(height/width);
pollV3=imrotate(pollV2,-theta);

%% Figure(5) - Rotated Pollution Image
figure(5)
surf(flux2V3,'FaceColor','interp','Edgecolor','interp')
axis equal
colormap jet(1000)
title('Rotated Pollution Image')
view(0,90)

%% Crop Pollution Image to Target Size
```

```
%CROP IMAGE TO FULL TARGET SIZE
%bottom left corner
xbl=1667;
ybl=428;
%top right corner
xtr=4114;
ytr=2890;
xdif=xtr-xbl;
ydif=ytr-ybl;
pollV4=pollV3(ybl:ybl+ydif-1,xbl:xbl+xdif-1);

%% Figure(6) - Cropped Pollution Image
figure(6)
surf(flux2V4,'FaceColor','interp','Edgecolor','interp')
axis equal
colormap jet(1000)
title('Cropped Pollution Image')
view(0,90)

%%
% ###### ------Images are corrected and ready for processing------#######

%% Removing Pollution using Pollution Image and Average Flux Border Values
[fI,fJ]=size(fluxV4);
fluxV5=zeros(fI,fJ);
%average pollution value
av_poll=mean(mean(pollV4));%using pollution image
for i=1:fI
   for j=1:fJ
      new=fluxV4(i,j)-av_poll;
      if new>=0
         fluxV5(i,j)=new;
      else
         fluxV5(i,j)=0;
      end
   end
end
minV5=min(min(fluxV5))
maxV5=max(max(fluxV5))

figure(7)
surf(fluxV5,'FaceColor','interp','Edgecolor','interp')
axis equal
colormap jet(1000)
title('Flux With Average Light Pollution From Pollution Image Removed')
view(0,90)
```

```
%Assuming target edges are darkness
av_bound=mean([mean(fluxV4(1,:)),mean(fluxV4(end,:)),mean(fluxV4(:,1)),mean(fluxV4(:,end))]);
fluxV6=zeros(fI,fJ);
for i=1:fI
   for j=1:fJ
      new=fluxV4(i,j)-av_bound;
      if new>=0
         fluxV6(i,j)=new;
      else
         fluxV6(i,j)=0;
      end
   end
end
minV6=min(min(fluxV6))
maxV6=max(max(fluxV6))
centroid=regionprops(true(size(fluxV4)),fluxV6,'WeightedCentroid');%centre of mass

figure(8)
hold on
surf(fluxV6,'FaceColor','interp','Edgecolor','interp')
xloc=round(centroid.WeightedCentroid(1));
yloc=round(centroid.WeightedCentroid(2));
plot3(xloc,yloc,maxV6+10,'kx')
axis equal
colormap jet(1000)
title('Flux With Average Light Pollution From Flux Image Boundaries Removed')
view(0,90)

%% Normalize Flux Maps
%NORMALIZE FLUX MATRICES
temp1=im2double(fluxV4);
temp2=im2double(fluxV5);
temp3=im2double(fluxV6);
maxV4=max(max(temp1));
maxV5=max(max(temp2));
maxV6=max(max(temp3));
fluxV4norm=temp1./maxV4;
fluxV5norm=temp2./maxV5;
fluxV6norm=temp3./maxV6;

%%
%#### ---------GENERATE INTERCEPT FACTOR DATA---------- ####

%% ADD flux Matrix to dark matrix.
board_area=0.54^2;%m^2
pixelarea4=board_area/(numel(fluxV4norm));
```

```
pixelarea5=board_area/(numel(fluxV5norm));
pixelarea6=board_area/(numel(fluxV6norm));

fluxV4norm=padarray(fluxV4norm,[1000,1000],0,'both');
fluxV5norm=padarray(fluxV5norm,[1000,1000],0,'both');
fluxV6norm=padarray(fluxV6norm,[1000,1000],0,'both');

%% Intercept Data for No Pollution correction
%centroids of all three images
centroid=regionprops(true(size(fluxV4norm)),fluxV4norm,'WeightedCentroid');
cent=centroid.WeightedCentroid;
centreV4raw=[round(cent(1)),round(cent(2))];

centroid=regionprops(true(size(fluxV5norm)),fluxV5norm,'WeightedCentroid');
cent=centroid.WeightedCentroid;
centreV5raw=[round(cent(1)),round(cent(2))];

centroid=regionprops(true(size(fluxV6norm)),fluxV6norm,'WeightedCentroid');
cent=centroid.WeightedCentroid;
centreV6raw=[round(cent(1)),round(cent(2))];

%properties
disharea=15.57028631;
target_area=(250/1000)^2;%m^2
CR_target=disharea/target_area;%target concentration ratio

%processing V4
AreaPerPixV4raw=pixelarea4;
fluxV4norm_sum=sum(sum(fluxV4norm));
interceptV4raw=[];
CRV4raw=[];
for i=1:2000
   shift1=i-1;
   zone4=fluxV4norm(centreV4raw(1)-shift1:centreV4raw(1)+shift1,centreV4raw(2)-shift1:centreV4raw(2)+shift1);
   zone4_suma=sum(sum(zone4));
   interceptV4raw=[interceptV4raw (zone4_suma/fluxV4norm_sum)];
   CRV4raw=[CRV4raw disharea/((AreaPerPixV4raw*numel(zone4)))];
end

%processing V5
AreaPerPixV5raw=pixelarea5;
fluxV5norm_sum=sum(sum(fluxV5norm));
interceptV5raw=[];
CRV5raw=[];
for i=1:2000
   shift1=i-1;
```

```
    zone5=fluxV5norm(centreV5raw(1)-shift1:centreV5raw(1)+shift1,centreV5raw(2)-shift1:centreV5raw(2)+shift1);
    zone5_suma=sum(sum(zone5));
    interceptV5raw=[interceptV5raw (zone5_suma/fluxV5norm_sum)];
    CRV5raw=[CRV5raw disharea/((AreaPerPixV5raw*numel(zone5)))];
end

%processing V6
AreaPerPixV6raw=pixelarea6;
fluxV6norm_sum=sum(sum(fluxV6norm));

interceptV6raw=[];
CRV6raw=[];
for i=1:2000
    shift1=i-1;
    zone6=fluxV6norm(centreV6raw(1)-shift1:centreV6raw(1)+shift1,centreV6raw(2)-shift1:centreV6raw(2)+shift1);
    zone6_suma=sum(sum(zone6));
    interceptV6raw=[interceptV6raw (zone6_suma/fluxV6norm_sum)];
    CRV6raw=[CRV6raw disharea/((AreaPerPixV6raw*numel(zone6)))];
end

%%
figure(9)
hold on
plot([CR_target,CR_target],[0,1],'--r')
plot(CRV4raw,interceptV4raw,'-r',CRV5raw,interceptV5raw,'-g',CRV6raw,interceptV6raw,'-b')
set(gca,'XScale','log')
legend('Target Area','No Light Pollution Correction','Light Pollution Correction Using Pollution Image','Light Pollution Correction Assuming
Target Edge is Darkness','Location','southeast')
title('Intercept Factor Using Raw Images')
xlabel('Concentration Ratio')
ylabel('Flux Intercept factor [%]')
grid on

figure(11)
hold on
surf(zone6,'FaceColor','interp','Edgecolor','interp')
axis equal
colormap hot(100)
colorbar
title('Flux With Average Light Pollution From Pollution Image Removed')
view(0,90)

figure(12)
surf(fluxV6norm,'Facecolor','interp','EdgeColor','interp')
colormap hsv(100)
colorbar
```

```
axis equal
view(0,90)

centroid=regionprops(true(size(zone4)),zone4,'WeightedCentroid');
cent=centroid.WeightedCentroid;
centrezone4=[round(cent(1)),round(cent(2))];

centroid=regionprops(true(size(zone5)),zone5,'WeightedCentroid');
cent=centroid.WeightedCentroid;
centrezone5=[round(cent(1)),round(cent(2))];

centroid=regionprops(true(size(zone6)),zone6,'WeightedCentroid');
cent=centroid.WeightedCentroid;
centrezone6=[round(cent(1)),round(cent(2))];

 x1= 0:1:4466;
x1=(x1-2292)*(AreaPerPixV6raw^0.5);

y1=0:1:4451;
y1=(y1-2225)*(AreaPerPixV6raw^0.5);

[X_MATRIX,Y_MATRIX]=meshgrid(y1,x1);
Z_MATRIX=fluxV6norm;

figure(13)
hold on
surf(X_MATRIX,Y_MATRIX,Z_MATRIX,'FaceColor','interp','Edgecolor','interp')
axis equal
colormap hot(500)
colorbar
title('Normalised Flux Surface Map')
view(0,90)

%Reference: Sumner, R., 2014. Processing RAW images in MATLAB. Santa Cruz, CA: Department of Electrical Engineering, UC Santa Cruz.
```

Appendix C.2 RAW graphics and intercept factor post-processor – Python

C.2.1 Introduction

The code presented below takes the .mat file results from the code in Appendix C.1 and generates the necessary flux maps using the Viridis colour map in Python. This was necessary as the default colour maps provided in the Matplotlib library in MATLAB for contour plots can produce images with falsely represented areas of intensity. Viridis is from a class of colour maps called "perceptually uniform sequential colormaps" and allows flux maps to be representative of the true flux intensities on the target surface. The code also exported the intercept factor versus geometry data to an Excel file for plotting, as well as the transect data cutting through the weighted centroid of the flux image and coordinate matrices on the *x*- and the *y*-plane.

C.2.2 Python code

```
import scipy.io
import numpy as np
from matplotlib import pyplot as plt
import pandas as pd
from pandas import ExcelWriter
# from pandas import ExcelFile
from mpl_toolkits.axes_grid1 import make_axes_locatable
# from mpl_toolkits.mplot3d import axes3d

rawarray=scipy.io.loadmat(r'E:\Honours\MSS732 Research Study\Deathray 2\MATLAB Code\RAWarraycorrect3.mat')


#  1--> No pollution correction
#  2--> Pollution image correction
#  3--> Edge darkness correction

#area per pixel
Aperpix1=rawarray['AreaPerPixV4raw'][0,0]
Aperpix2=rawarray['AreaPerPixV5raw'][0,0]
Aperpix3=rawarray['AreaPerPixV6raw'][0,0]

#length per pix
Lperpix1=np.sqrt(Aperpix1)
Lperpix2=np.sqrt(Aperpix2)
Lperpix3=np.sqrt(Aperpix3)

#Concentration Ratio
cr1=rawarray['CRV4raw'][0,:]
```

```
cr2=rawarray['CRV5raw'][0,:]
cr3=rawarray['CRV6raw'][0,:]

#Target concentration ratio
crtarget=rawarray['CR_target'][0,0]

#Weighted flux centre
cent1=rawarray['centrezone4'][0,:]
cent2=rawarray['centrezone5'][0,:]
cent3=rawarray['centrezone6'][0,:]

#Intercept factor
intercept1=rawarray['interceptV4raw'][0,:]
intercept2=rawarray['interceptV5raw'][0,:]
intercept3=rawarray['interceptV6raw'][0,:]

#Flux matrices
raw1=np.asarray(rawarray['zone4'])
raw2=rawarray['zone5']
raw3=rawarray['zone6']

cutx1=raw1[:,cent1[0]]
cuty1=raw1[cent1[1],:]
cutx2=raw2[:,cent2[0]]
cuty2=raw2[cent2[1],:]
cutx3=raw3[:,cent3[0]]
cuty3=raw3[cent3[1],:]

writer=ExcelWriter('Corrected RAW data3.xlsx', engine='xlsxwriter')
df1=pd.DataFrame({'Xplane Cut1':cutx1,
                  'Xplane Cut2':cutx2,
                  'Xplane Cut3':cutx3})
df2=pd.DataFrame({'Yplane Cut1':cuty1,
                  'Yplane Cut2':cuty2,
                  'Yplane Cut3':cuty3})
DF=pd.DataFrame({'CR1':cr1,
                 'CR2':cr2,
                 'CR3':cr3,
                 'Intercept1':intercept1,
                 'Intercept2':intercept2,
                 'Intercept3':intercept3})
DF.to_excel(writer,'Raw Image Data')
df1.to_excel(writer,'Xplane Cuts')
df2.to_excel(writer,'Yplane Cuts')
writer.save()
```

```
#Xcoords lists
x,y=np.shape(raw1)
xl=np.arange(0,x,1)
yl=np.arange(0,y,1)

xl1=(xl-cent1[0])*Lperpix1
yl1=(yl-cent1[1])*Lperpix1
X1,Y1=np.meshgrid(xl1,yl1)

xl2=(xl-cent2[0])*Lperpix2
yl2=(yl-cent2[1])*Lperpix2
X2,Y2=np.meshgrid(xl2,yl2)

xl3=(xl-cent3[0])*Lperpix3*1000
yl3=(yl-cent3[1])*Lperpix3*1000
X3,Y3=np.meshgrid(xl3,yl3)

#plt.figure(10)
#plt.plot(np.arange(0,3999,1),cutx1,np.arange(0,3999,1),cuty1)

#PLOTTING

plt.figure(1)
figure1,ax1=plt.subplots()
contour1=ax1.contourf(X1[cent1[1]-600:cent1[1]+600,cent1[0]-600:cent1[0]+600],
                      Y1[cent1[1]-600:cent1[1]+600,cent1[0]-600:cent1[0]+600],
                      raw1[cent1[1]-600:cent1[1]+600,cent1[0]-600:cent1[0]+600]
                      ,500)
contour1.set_cmap('viridis')
plt.gca().set_aspect('equal')
plt.grid()
cbar=figure1.colorbar(contour1,ticks=np.arange(0,1.1,0.1))
cbar.ax.set_ylabel('Flux Intensity Ratio',fontsize=14)
plt.title('Flux Ratio Map - No Pollution Correction',fontsize=14)
plt.xlabel('X [m]',fontsize=12)
plt.ylabel('Y [m]',fontsize=12)

plt.figure(2)
figure2,ax2=plt.subplots()
contour2=ax2.contourf(X2[cent2[1]-600:cent2[1]+600,cent2[0]-600:cent2[0]+600],
                      Y2[cent2[1]-600:cent2[1]+600,cent2[0]-600:cent2[0]+600],
                      raw2[cent2[1]-600:cent2[1]+600,cent2[0]-600:cent2[0]+600],
                      500)
contour2.set_cmap('viridis')
plt.gca().set_aspect('equal')
plt.grid()
```

```
cbar=figure2.colorbar(contour2,ticks=np.arange(0,1.1,0.1))
cbar.ax.set_ylabel('Flux Intensity Ratio',fontsize=14)
plt.title('Flux Ratio Map - Pollution Correction Using Image of Pollution',fontsize=14)
plt.xlabel('X [m]',fontsize=12)
plt.ylabel('Y [m]',fontsize=12)


plt.figure(3)
figure2,ax2=plt.subplots()
contour3=ax2.contourf(X3[cent3[1]-1367:cent3[1]+1367,cent3[0]-1367:cent3[0]+1367],
                      Y3[cent3[1]-1367:cent3[1]+1367,cent3[0]-1367:cent3[0]+1367],
                      raw3[cent3[1]-1367:cent3[1]+1367,cent3[0]-1367:cent3[0]+1367],
                      500)
contour3.set_cmap('viridis')
plt.gca().set_aspect('equal')
plt.grid()
cbar=figure2.colorbar(contour3,ticks=np.arange(0,1.1,0.1))
cbar.ax.set_ylabel('Flux Ratio',fontsize=14)
plt.xlabel('X [mm]',fontsize=12)
plt.ylabel('Y [mm]',fontsize=12)

fig=plt.figure(5)
ax1=fig.add_subplot(1,3,1,adjustable='box',aspect=1)
ax2=fig.add_subplot(1,3,2,adjustable='box',aspect=1,sharey=ax1)
ax3=fig.add_subplot(1,3,3,adjustable='box',aspect=1,sharey=ax1)

cont1=ax1.contourf(X1[cent1[1]-600:cent1[1]+600,cent1[0]-600:cent1[0]+600],
                   Y1[cent1[1]-600:cent1[1]+600,cent1[0]-600:cent1[0]+600],
                   raw1[cent1[1]-600:cent1[1]+600,cent1[0]-600:cent1[0]+600]
                   ,500)
divider1=make_axes_locatable(ax1)
cax1=divider1.append_axes('right',size='5%',pad=0.05)
fig.colorbar(cont1,cax=cax1,ticks=np.arange(0,1.1,0.1))
ax1.set_ylabel('Y [m]')
ax1.set_xlabel('X [m]')
ax1.title.set_text('No Pollution Correction')

cont2=ax2.contourf(X2[cent2[1]-600:cent2[1]+600,cent2[0]-600:cent2[0]+600],
                   Y2[cent2[1]-600:cent2[1]+600,cent2[0]-600:cent2[0]+600],
                   raw2[cent2[1]-600:cent2[1]+600,cent2[0]-600:cent2[0]+600],
                   500)
divider2=make_axes_locatable(ax2)
cax2=divider2.append_axes('right',size='5%',pad=0.05)
fig.colorbar(cont2,cax=cax2,ticks=np.arange(0,1.1,0.1))
#ax2.set_ylabel('Y [m]')
ax2.set_xlabel('X [m]')
```

```
ax2.title.set_text('Pollution Correction Using Pollution Image')

cont3=ax3.contourf(X3[cent3[1]-600:cent3[1]+600,cent3[0]-600:cent3[0]+600],
                   Y3[cent3[1]-600:cent3[1]+600,cent3[0]-600:cent3[0]+600],
                   raw3[cent3[1]-600:cent3[1]+600,cent3[0]-600:cent3[0]+600],
                   500)
divider3=make_axes_locatable(ax3)
cax3=divider3.append_axes('right',size='5%',pad=0.05)
cbar=fig.colorbar(cont3,cax=cax3,ticks=np.arange(0,1.1,0.1))
cbar.ax.set_ylabel('Flux Intensity Ratio',fontsize=14)
#ax3.set_ylabel('Y [m]')
ax3.set_xlabel('X [m]')
ax3.title.set_text('Pollution Correction Using Dark Edges')

fig.suptitle('Flux Ratio Maps for Raw Images', fontsize=18)

fig1 = plt.figure(6)
ax6 = fig1.gca(projection='3d')
surf=ax6.plot_surface(X1, Y1, raw1,cmap='viridis',rstride=10,cstride=10)
cbar=fig1.colorbar(surf,ticks=np.arange(0,1.1,0.1))
ax6.set_xlabel('X [m]')
ax6.set_ylabel('Y [m]')
ax6.set_zlabel('Flux Ratio')
ax6.view_init(elev=30,azim=45)
plt.title('No Pollution Correction')
cbar.ax.set_ylabel('Flux Ratio',fontsize=14)

fig2 = plt.figure(7)
ax7 = fig2.gca(projection='3d')
surf=ax7.plot_surface(X2, Y2, raw2,cmap='viridis',rstride=10,cstride=10)
cbar=fig2.colorbar(surf,ticks=np.arange(0,1.1,0.1))
ax7.set_xlabel('X [m]')
ax7.set_ylabel('Y [m]')
ax7.set_zlabel('Flux Ratio')
ax7.view_init(elev=30,azim=45)
plt.title('Pollution Correction Using Pollution Image')
cbar.ax.set_ylabel('Flux Ratio',fontsize=14)

#dark edge treatment
fig3 = plt.figure(8)
ax8 = fig3.add_subplot(111,projection='3d')
surf=ax8.plot_surface(X3[cent3[1]-1367:cent3[1]+1367,cent3[0]-1367:cent3[0]+1367],
                      Y3[cent3[1]-1367:cent3[1]+1367,cent3[0]-1367:cent3[0]+1367],
                      raw3[cent3[1]-1367:cent3[1]+1367,cent3[0]-1367:cent3[0]+1367],cmap='viridis',rstride=3,cstride=3)
cbar=fig3.colorbar(surf,ticks=np.arange(0,1.0,0.1))
ax8.set_xlabel('X [mm]')
```

```
ax8.set_ylabel('Y [mm]')
ax8.set_zlabel('Flux Ratio')
ax8.view_init(elev=30,azim=45)
cbar.ax.set_ylabel('Flux Ratio',fontsize=14)
```

Appendix C.3 SolTrace CSV post-processor – Python

C.3.1 Introduction

The numerical model produced ray hit data that contained a ray number and the coordinates on the virtual stage target that it hit, which was exported as a CSV file. To transform this into a flux map and calculate the intercept factors, the following code was used:

Running the script will prompt the user to select a CSV file for processing and then return the maximum and minimum x and y coordinates where a ray hit the virtual target surface. This allows for user input to define the boundaries of what will become the image size in terms of the x and y coordinates. The user is then prompted to specify the pixel density of the image. This defines the density of a grid that is overlayed on the image setup. A loop then checks the coordinates of each ray in the CSV file to see if it falls within the spatial boundaries for a specific pixel element. If a ray falls in the element region, it is counted. This is repeated for every element. When the loop has counted all the valid rays, the x and y centroid of the element is written to its respective x and y coordinate matrices and the sum of the rays that fall within the element is written to the user-defined image matrix. The CSV data is then converted into an image and the weighted centroid is calculated. The same intercept factor and geometric concentration ratio calculation process is followed as described in Appendix C.1.6. The flux maps are then generated using the same colour map, and the intercept factor and geometric concentration ratio data is written to an Excel file for plotting.

C.3.2 Python code

```
"""Notes
-- Install easygui using anaconda prompt with 'conda install -c conda-forge easygui'
-- Download photutils using anaconda prompt with 'conda install -c conda-forge photutils'
"""

import easygui
import numpy as np
import os
from photutils import centroid_com
from matplotlib import pyplot as plt
import pandas as pd
from pandas import ExcelWriter

def clear():
    os.system('cls' if os.name == 'nt' else 'echo -e \\\\033c')
clear()
```

```
17.
18. print("#############################################################################################################",'\n')
19.
20. print("#############################################################################################################")
21. print('Please select the output .csv file from SolTrace to be processed. Note -
    > alt + Tab to get to selection window if hidden')
22. print("#############################################################################################################",'\n')
23.
24. print("#############################################################################################################",'\n')
25.
26. path = easygui.fileopenbox('Please select a file')
27. data=np.genfromtxt(path,delimiter=",",skip_header=1)
28.
29. print('\n')
30. print('File imported successfully','\n')
31.
32. """
33. Data format by column: PosX, PosY, PosZ, CosX, CosY, CosZ, Element, Stage, RayNumber
34. -reduce matrix size by deleting columns 3,4,5,6,7 and 8. Yields 2D data and raynumber
35. """
36.
37. globalf=data[0,2]
38.
39. """
40. For geometry where Z-axis is vertical
41. """
42. data=np.delete(data,2,1)
43. data=np.delete(data,2,1)
44. data=np.delete(data,2,1)
45. data=np.delete(data,2,1)
46. data=np.delete(data,2,1)
47. data=np.delete(data,2,1)
48.
49. """
50. For geometry where Y-axis is vertical
51. """
52. # data=np.delete(data,1,1)
53. # data=np.delete(data,2,1)
54. # data=np.delete(data,2,1)
55. # data=np.delete(data,2,1)
56. # data=np.delete(data,2,1)
57. # data=np.delete(data,2,1)
```

```
58.
59.  #convert to mm
60.  data[:,0]=data[:,0]*1000
61.  data[:,1]=data[:,1]*1000
62.
63.  raycount,datatypes=np.shape(data)
64.
65.  #get image boundaries
66.  xmax=np.max(data[:,0])
67.  xmin=np.min(data[:,0])
68.
69.  ymax=np.max(data[:,1])
70.  ymin=np.min(data[:,1])
71.  dely=ymax-ymin
72.
73.  raymax=np.max(data[:,2])
74.  raymin=np.min(data[:,2])
75.  delx=xmax-xmin
76.
77.  maxdia=max([delx,dely])
78.  imarea=np.pi*(maxdia)**2*0.25
79.
80.  print('Image range is ',xmin,' to ',xmax,' in X and ',ymin,' to ',ymax,' in Y. Yielding an image size of X: ',delx,'mm by Y: ',d
     ely, 'mm with an area of ',imarea,' mm^2','\n')
81.
82.  #define raw matrix size based on image size
83.  print('\n')
84.  val=str(xmax)
85.  prompt="Please choose a valaue for the MAXIMUM X-
     value?. Note MAX X magnitude from centre of the current flux is {}mm. ===>".format(val)
86.  xval=input(prompt)
87.  # xval=80
88.  Xmax=int(xval)
89.
90.  print('\n')
91.  val=str(xmin)
92.  prompt="please choose a value for the  MINIMUM X-
     value?. Note MIN X magnitude from centre of the current flux is {}mm. ===>".format(val)
93.  xval=input(prompt)
94.  # xval=-80
95.  Xmin=int(xval)
96.  del(xval)
97.
98.  print('\n')
99.  val=str(xmax)
```

```
prompt="Please choose a valaue for the MAXIMUM Y-
value?. Note MAX Y magnitude from centre of the current flux is {}mm. ===>".format(val)
yval=input(prompt)
# yval=80
Ymax=int(yval)

print('\n')
val=str(xmin)
prompt="please choose a value for the  MINIMUM Y-
value?. Note MIN Y magnitude from centre of the current flux is {}mm. ===>".format(val)
yval=input(prompt)
# yval=-80
Ymin=int(yval)
del(yval)
del(prompt)
del(val)

print('\n')
print('Next step is to define the image resolution which will be square (N x N pixels)','\n')

xydiv=input('How many divisions in x and y? ===>')
# xydiv=100
xydiv=int(xydiv)

#define dish area
# disharea=800**2*0.25*np.pi# [mm^2]single facet directly aimed at sun
disharea=15.57*1000**2# large array [mm^2}]

#define discretised node values for x and y
xlist=np.linspace(Xmin,Xmax,xydiv)
ylist=np.linspace(Ymin,Ymax,xydiv)

#Loop through csv data using xlist and ylist to generate X,Y and pixel matrices

pixelx=len(xlist)-1
pixely=len(ylist)-1

xgrid=np.zeros((pixelx,pixely))
ygrid=np.zeros((pixelx,pixely))
pix=np.zeros((pixelx,pixely))#hit matrix tha will represent the flux distribution

for i in range(pixelx):
    lx=xlist[i]
    hx=xlist[i+1]
    xcoord=(lx+hx)/2

```

```
    for j in range(pixely):
        hits=0
        ly=ylist[j]
        hy=ylist[j+1]
        ycoord=(ly+hy)/2

        hits= (lx <= data[:,0]) & (data[:,0] <= hx) & (ly <= data[:,1]) & (data[:,1] <= hy)
        hits=np.count_nonzero(hits)

        xgrid[i,j]=xcoord
        ygrid[i,j]=ycoord
        pix[i,j]=hits
print('Flux camptured','\n')

#Normalise flux matrix
maxpix = np.max(pix)
Z=pix/maxpix
del(pix)

# image centroids
xcent,ycent=centroid_com(Z)
xcent=int(round(xcent))
ycent=int(round(ycent))

txt="Image X and Y index values for Centroid are {} and {}".format(xcent,ycent)
print(txt,'\n')

#generate geometric concentration ratio and intercept factor lists
dx=np.abs(xlist[1]-xlist[0])
dy=np.abs(ylist[0]-ylist[1])
pixelarea=dx*dy
imagetot=np.sum(Z)
lenx, leny =np.shape(Z)
itr=np.max([round(lenx/2),round(leny/2)])+10
padwidth=(np.abs(lenx-leny))+100
Z1=np.pad(Z,padwidth,'constant',constant_values=0)

# image centroids
xcent,ycent=centroid_com(Z1)
xcent=int(round(xcent))
ycent=int(round(ycent))

intercept=[]
geoCR=[]
for i in range(itr):
    shift = i-1
```

```
    subarray = Z1[(xcent -shift):(xcent+shift),(ycent-shift):(ycent+shift)]
    subarray_sum = np.sum(subarray)
    intercept.append((subarray_sum/imagetot))
    xx,yy=np.shape(subarray)
    geoCR.append((disharea/(pixelarea*xx*yy)))

#plotting results
plt.figure(1)
plt.semilogx(geoCR,intercept)
plt.title('Intercept Factor vs Geometric Concentration Ratio')
plt.ylabel('Intercept Factor [%]')
plt.xlabel('Geometric Concetration Ratio')
plt.grid(True)

figure2,ax2=plt.subplots()
contour2=ax2.contour(xgrid,ygrid,Z,600)
contour2.set_cmap('viridis')
plt.gca().set_aspect('equal')
plt.grid(True)
cbar=figure2.colorbar(contour2,ticks=np.arange(0,1,0.1))
cbar.ax.set_ylabel('Normalised Flux Intensity',fontsize=14)
plt.title('Normalised FLux Ratio Map',fontsize=12)
plt.xlabel('X [mm]',fontsize=12)
plt.ylabel('Y [mm]',fontsize=12)

writer=ExcelWriter('Intercept vs CRg.xlsx', engine='xlsxwriter')
df1=pd.DataFrame({'Intercept factor':intercept,
                  'GeoConcRatio':geoCR})
df1.to_excel(writer,'Xplane Cut')
writer.save()
```

Appendix D Additional numerical results

The tilt angle versus translation distance was investigated for an elliptical facet in order to validate the SolidWorks optical model that was used to calculate the required membrane depth for a facet based on its location in the array relative to the target centroid. It was also performed to understand the unknown behaviour of elliptically supported membranes due to the dual focal length nature. An assumption that the total angle between the incoming and reflected ray (image angle) is equal to twice the tilt angle of the facet that was used during the design of the experimental setup is also validated. The results from the validated SolidWorks optical model developed by Swanepoel et al. (2020) were then used to generate the full-array CAD model with the correct membrane depths, locations and tilt angles to produce the smallest possible focal image that the experimental setup could achieve given its facet layout. Figure D.1 illustrates the analysis setup used to investigate tilt angle and translation distance for a facet orientated so that it tilts about its minor axis. The resulting data is also used to calculate image angles and focal lengths.

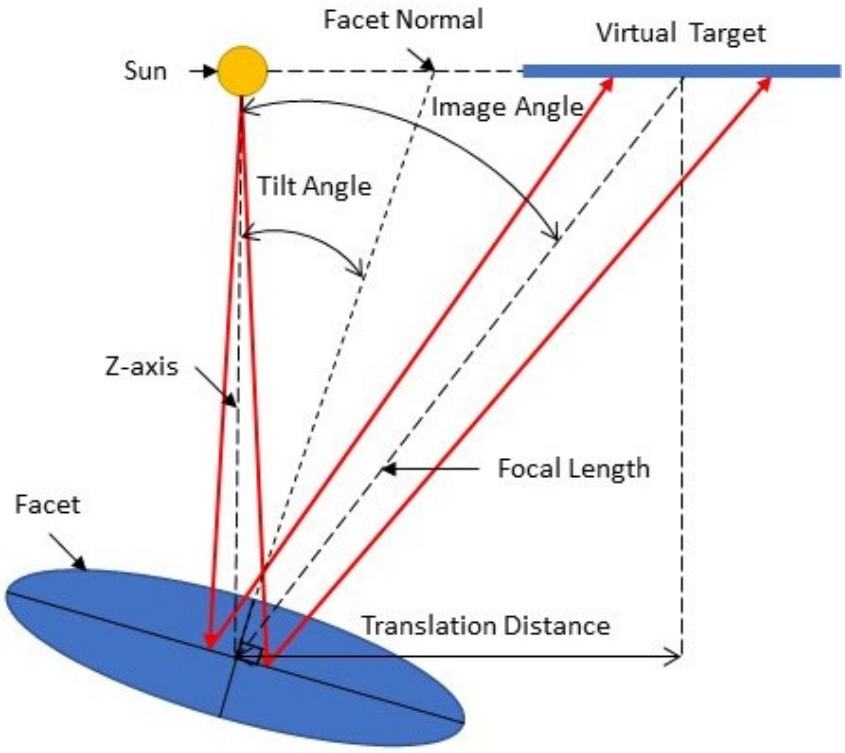

Figure D.1: Tilt angle and translational distance analysis setup

Figure D.2 shows the relationship between the tilt angle and the translation distance. Equation (D.1) represents the curve in Figure D.2 where T is the translational distance of the image as described in Figure D.1. The focal length was also checked to see if it remained consistent at different facet tilt angles. Figure D.3 shows that the numerically determined image angles are very similar to the expected image angle of twice the facet tilt angle and is therefore validated. A small decrease in focal length was also noticed in the results, but is based on a single facet aspect ratio and membrane depth of 15 mm as shown in Figure D.4 and described by Equation (D.2). Further investigation needs to be performed to determine the optical behaviour over a range of facet aspect ratios using various membrane depths and tilt angles in future work.

Additional images of the numerical model solution are presented in figures D.5 and D.6. Figure D.5 is a flux map result from a full-array analysis using 1 000 000 ray intersections in SolTrace with a 0 mrad total optical error. It clearly shows the negative impact, shown as a flower petal-like region on the boundary of the hot spot, with respect to the image size due to the facets being orientated to rotate about their major axis even when no optical error is present. Figure D.6 shows a side view of the same simulation with the ray paths added to visualise the concentrating behaviour of the array and give a sense of scale. Figure D.7 illustrates the image inversion for a single facet with the results from an analytical simulation in SolTrace as described in section 3.4.1.

$$\theta_{tilt} = 3.5903T^3 - 9.0288T^2 + 18.224T - 2.1326 \qquad (D.1)$$

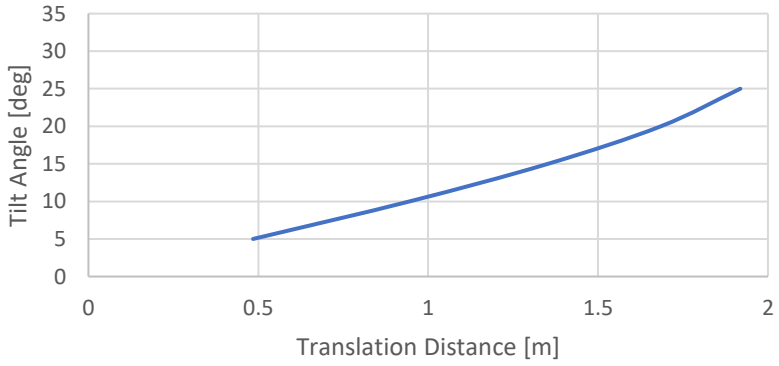

Figure D.2: Tilt angle versus image translation distance

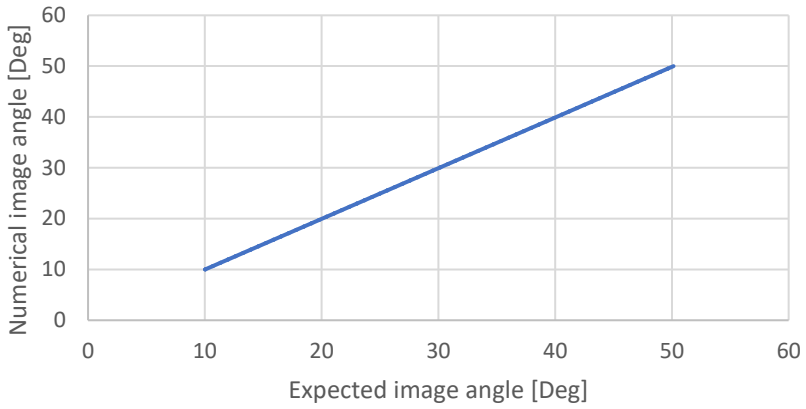

Figure D.3: Numerical image angle result versus the expected image angle

$$f = -0.0006\theta^2 + 0.003\theta + 2.783 \qquad (D.2)$$

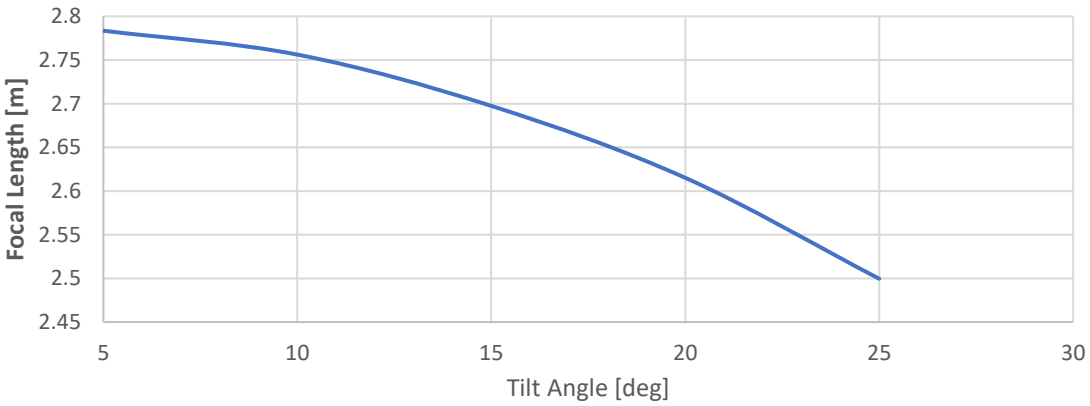

Figure D.4: Focal length versus facet tilt angle

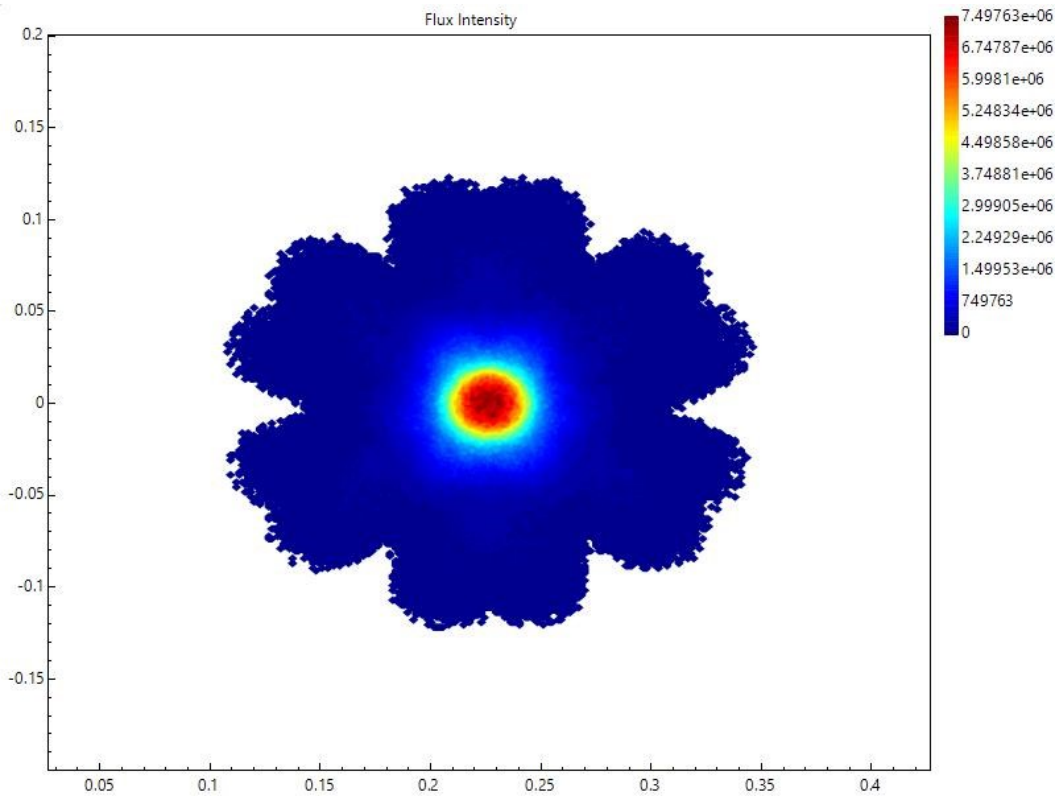

Figure D.5: A 0 mrad numerical solution with a flux map from SolTrace with the vertical *y*-axis and horizontal *x*-axis in metres. Intensity values are based on 1 000 W/m^2 and are reported in W/m^2.

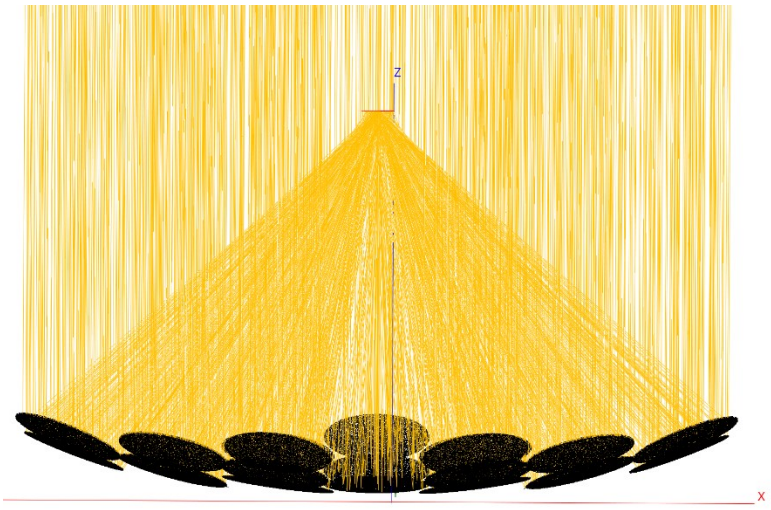

Figure D.6: Traced rays shown in the final numerical solution for the 0 mrad case

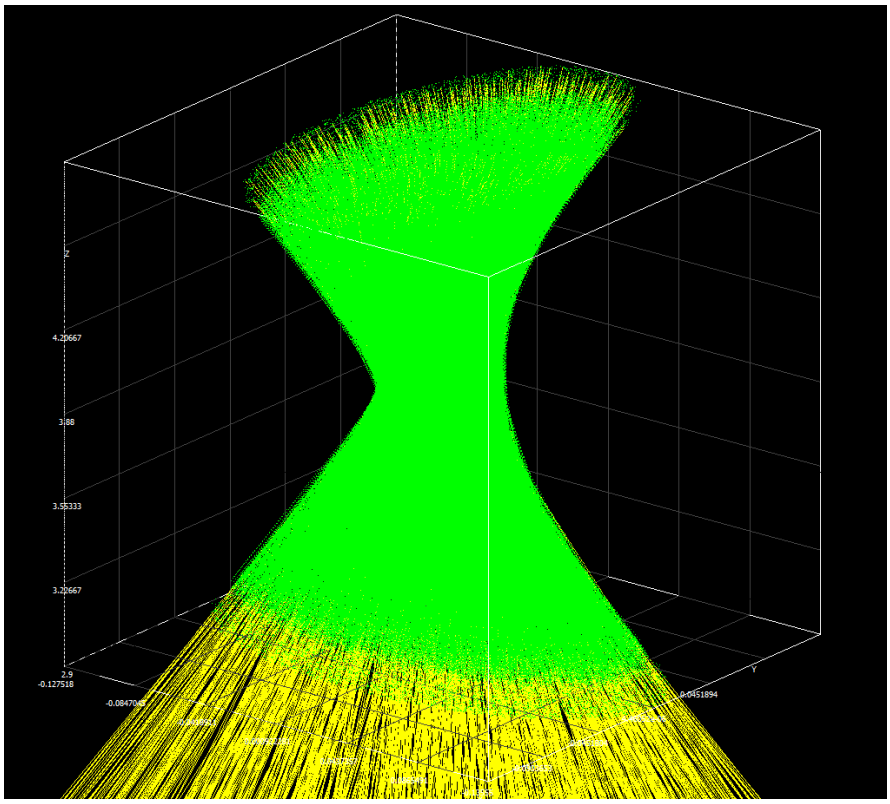

Figure D.7: Ray paths showing image inversion for single elliptical facet in SolTrace